Fermionic singlet and two-component dark matter

Master thesis submitted by
Sonja Esch

Münster, 30. September 2014

Peer Reviewer: Prof. Dr. Michael Klasen
Peer Reviewer: Prof. Dr. Christian Weinheimer

Abstract

In this thesis two minimal models in the framework of Higgs portal dark matter are presented. The fermionic dark matter model adds two new fields to the Standard Model. One Majorana fermion, which is the stable dark matter, thanks to a new $\mathbb{Z}_2$ symmetry, and a real scalar. The allowed parameter space is identified and characterized by imposing the relic density constraint on the entire parameter range, the impact of current and future direct detection experiments are incorporated as well as indirect detection feasibility.

The two-component dark matter model can be seen as an extension of the singlet fermionic dark matter model with a singlet scalar. As before an additional symmetry stabilizes the lighter particle, while the heavier is stable by an accidental symmetry. So within this model two dark matter species arise, one fermion and one scalar, enabling one of the most important new features: dark matter conversion. The conversion from one dark matter species to the other can have a large impact on the relic density. As a last point the direct detection prospects in the two-component model are studied.

Contents

Acknowledgements

I would like to offer my special thanks to all people who helped me on completing this thesis. All advice and help offered is greatly appreciated.

First I would like to express my very great appreciation to Prof. Dr. Michael Klasen, who offered me this particular interesting topic and enabled me to take part in many insightful conferences and workshops. I am grateful for this generous support. Without, this thesis would not have been possible.

Next, I would like to sincerely thank my supervisor Dr. Carlos E. Yaguna for all his advice and support and all the time he spent on helping me. The guidance and support I received is greatly appreciated.

I would also like to offer my special thanks to Prof. Dr. Christian Weinheimer for providing me with the opportunity to have a deep insight in experimental physicists work, the opportunity to learn a lot in different places and for the support on my further way which led to this thesis.

Furthermore, I would like to thank my office colleagues and the members of the particle physics groups in Münster for the friendly atmosphere, the nice coffee and occasionally also cake breaks and the encouraging conversations.

I also would like to thank my family, Beatrix, Thomas and Christian Esch for their love and support over the whole time. I appreciate all their help along my way.

Last, but not least, I offer my deepest thanks to Manuel Wiese, for his endless backing and cheering up. You carried me a long way and never ceased to encourage me. I am very grateful for this.

1. Introduction

Curiosity accompanies every step of mankind from the beginning on, we never cease to wonder and question the world around us. The desire to understand, the wish to gain more information is crucial to our lives. Ever since, the puzzle, how to describe the world attracted a lot of people. In a particle physics context, the Standard Model is a rather good description up to some energy scale, even though it has shortcomings. Cosmological and astrophysical observations convey the fact, that most of the Universe is not made of ordinary visible matter, but of some new kind of matter, which is not described in the Standard Model. As this new matter, which is only perceivable by its gravitational effects, does not emit any light, it is called dark matter. If dark matter is assumed to be a particle, it has to be neutral, colorless and stable compared to the lifetime of the Universe in oder to be consistent with all current observations.
The Standard Model describes all known particles, the quarks, leptons and the Higgs boson as well as the gauge bosons which are associated with the weak, strong and electromagnetic force, but there is no suitable dark matter particle among them. A well motivated class of models for dark matter focuses on weakly interacting particles (WIMPs), which are then the dark matter. WIMPs are produced as a thermal relic in the early Universe and with their weak scale interaction cross section they are very likely to match the currently observed relic density of dark matter. The evolution of the WIMP number density is described by the Boltzmann equation and enables a broad numerical investigation of WIMP models. As there is no suitable WIMP in the Standard Model, new theories are needed to explain dark matter. Some, like Supersymmetry, are complex and contain a somewhat natural dark matter candidate, while they aim at alleviating a shortcoming of the Standard Model other than dark matter. In other theories, the Standard Model is only extended by few fields in order to provide dark matter. Two such minimal extensions are presented and analyzed in this work, the fermionic singlet model, in which dark matter is an additional fermion, and the two-component dark matter model, in which a new scalar and a fermion act as dark matter, so somehow it can be seen as the extension of the singlet fermionic model with singlet scalar dark matter. To test these models there are in general three complementary types of dark matter searches, direct detection, indirect detection and collider searches, which can put constraints on the viable dark matter models. Hence the singlet fermionic model and the two-component model are analyzed regarding relic density, direct detection cross section and probable indirect detection bounds.

The rest of this work organizes as follows, first dark matter is introduced in section 2, evidence for dark matter and several WIMP models are described, as well as the WIMP relic density and the different techniques for dark matter detection as direct detection, indirect detection and collider searches. Then the main part of this work starts in section 3. The fermionic singlet model is described in detail and important aspects of its phenomenology are pointed out. Afterwards a numerical study is presented in which the viable regions in the parameter space consistent with current bounds are determined, followed by detection prospects regarding both direct and indirect detection. After that, in section 4 the two-component dark matter model is presented and analyzed in detail. Its phenomenology is investigated in numerical studies and conclusively a set of five parameter space points is chosen to illustrate future detection prospects.

In collaboration with Carlos Yaguna and Michael Klasen the course of this work led to the publication of two papers [1, 2], each paper is directed at the analysis of one of the two dark matter models which are presented here.

2. Dark Matter

Surprisingly, little is known about the different components of the Universe, yet its composition is determined with high precision. Cosmological discoveries have revealed approximately 5 % of the Universe's energy content consists of visible matter, the rest remains undetected yet. Precision measurements of the PLANCK [23] space-telescope point to the fact that the remaining 95 % consist of basically two-components. One of these two is matter, raising the matter content of the Universe to nearly 25%, the other is dark energy.

This – since not observed – dark matter is supposed to be non-relativistic and to interact only gravitationally or very weakly with ordinary matter. As dark matters nature is not revealed yet, it has been the focus of many scientific works over the past few years.

2.1. Evidence for Dark Matter

Evidence for dark matter is found on all scales by astrophysical and cosmological observations. One of the earliest observations was made by Fritz Zwicky in 1933 [17]. Zwicky measured the velocity dispersion of galaxies in the Coma cluster. A comparison between the velocities and the amount of luminous matter in the cluster gives a first clue that there is more mass than visible. If the galaxies in the cluster are gravitationally bound, the viral theorem should apply, which links the velocity of the bound galaxies to the gravitational potential of the cluster. But the measured velocities were too high for the galaxies to be bound by the potential. In order to fix that, the amount of mass in the cluster has to be approximately 400 times higher than contained luminous mass [17].

Since there are plenty of indications for dark matter, only a short outline will be given here. This comprises the observations that reveal most about this new type of matter and its properties, as the observation of galactic rotation curves, gravitational lensing, measurements of the Cosmic Microwave Background and the process of structure formation.

Galactic Rotation Curves

An impressive evidence for the presence of dark matter in our Universe comes from the analysis of galactic rotation curves. In a galaxy most of the luminous mass is gathered in the galactic center. According to Newtonian mechanics, for a star orbiting the center, the centrifugal force equals gravitational force. Thus to keep the star in its orbit

$$v = \sqrt{\frac{GM(r)}{r}} \tag{2.1}$$

is required, where v is the star's velocity, which could be measured by the redshift of star spectra, G is the gravitational constant, r is the distance to the center and $M(r)$ is the mass enclosed from the center up to r. By assuming a spherical mass density distribution $\rho(r)$ for matter - as supposed for the distribution of luminous matter – the enclosed mass is

$$M(r) = 4\pi \int_0^r r'^2 \rho(r') \mathrm{d}r' \ . \tag{2.2}$$

In regions far from the center most of the mass is already contained within the radius r. This results in $M(r)$ being nearly independent of r. Accordingly (2.1) simplifies to

$$v \propto \frac{1}{\sqrt{r}} \ . \tag{2.3}$$

One would expect that the rotation velocity drops in the far out regions, instead it is found to be constant.

In the 1960's and 1970's Vera Rubin and Kent Ford Jr. measured the rotation velocities of the Andromeda galaxy [15] by examining HII regions, consisting of ionized hydrogen gas, which emit light. A lot of other works on galactic rotation curves followed [16, 93, 94]. In 1985 the spiral galaxy NGC 3198 in the constellation Ursa Major was observed by van Albada et al. [16]. As pointed out before, the circular velocities should decrease when going to larger distances r, similar to the movement of planets in our solar system. Instead there is a strong discrepancy between the expected $\frac{1}{\sqrt{r}}$ behavior and the actual measured rotation curve which is shown in figure (2.1).

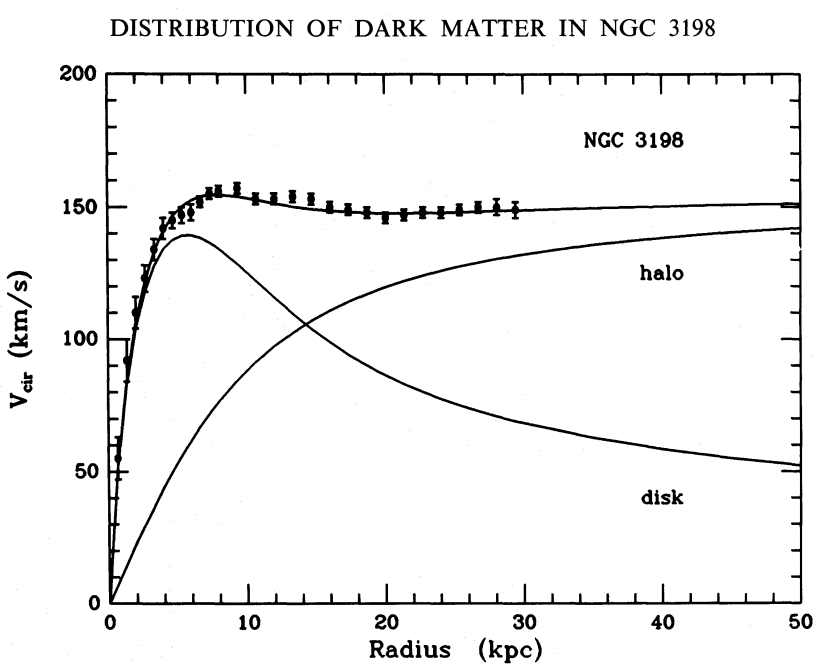

Figure 2.1.: Rotation curve of NGC 3198 indicating the presence of additional dark matter. Taken from [16].

The observed curve remains flat, even far outside the galactic center. This behavior can be modeled by adding a spherical halo of non-visible matter to the luminous mass distribution. The halo is supposed to have a mass density scaling like r^{-2} to match the experimental results. Another possible explanation for the deviation is an alteration of Newton's gravity laws at small accelerations, but other observations do not support this theory.

Gravitational Lensing

Light from distant luminous objects can be deflected by strong gravitational fields of matter distributions, for example galaxies or galaxy clusters. This deflection will cause an observer to see multiple or distorted images of the source as shown in figure 2.2, where the Abell cluster distorts the image of objects behind. Based on the observed alteration of the images, the gravitational mass along the line of sight can be deduced.

The amount of visible matter in a given cluster can be determined by X-ray spectroscopy. Comparing the results from lensing and X-ray signals reveals that in most cases the amount of gravitational mass is much larger than the visible mass. This discrepancy is a strong hint to dark matter.

Figure 2.2.: Distorted images due to gravitational lensing caused by the Abell galaxy cluster [11].

Using both techniques for mass measurements can give even more insight to the nature of dark matter. One famous example is the so called Bullet cluster [5]. The Bullet cluster or technically 1E 0657-558 is an ongoing cluster merger consisting of two smaller galaxy clusters which collided recently, which means on cosmological scales approximately 100 million years ago. A galaxy cluster consists of stars and galaxies, which are accumulated mainly at the cluster center. Intergalactic gas clouds fill up the space in between. If a cluster contained visible matter only, most of its mass would be comprised in interstellar gas. When two clusters collide, stars and galaxies are assumed to behave like collisionless objects and cross one another unaffected. Whereas the hot diffuse gas clouds interact electromagnetically. The clouds experience ram pressure and are ripped away from the galactic center. In fact, this can be observed in the Bullet cluster which is shown in figure 2.3. It incorporates a bigger main cluster, seen on the left, which was recently crossed by a smaller subcluster, seen more to the right. The image is overlaid with pink and blue colored regions, the pink regions are determined by X-ray spectroscopy to hold most of the intergalactic gas, whereas the blue regions contain the dominant matter contributions as determined by gravitational lensing. The pink regions with the intergalactic gas do not longer coincide with the visible centers of the clusters at which most stars and galaxies are gathered. The diffuse intergalactic clouds interacting with each other are now in between the two former centers. The smaller cluster to the left shows a bullet shaped region of gas, which is a shock front due to the recent collision and gave the cluster its name. Contrary to the expectation, the blue regions with the largest matter fraction still overlap strongly with the main amount of galaxies and stars at the former cluster centers. Other than expected without dark matter, most of the mass is not gathered in the gas clouds. The discrepancy points to

Figure 2.3.: Picture of X-ray emission, gravitational lensing and visible spectrum for the Bullet cluster [13].

dark matter being collisionless and mostly gravitationally interacting and also it makes up for most of the mass in such a system.

Cosmic Microwave Background Measurements

The cosmic microwave background (CMB) is a relic from the early Universe ,when photons and decoupled from baryons. Today it is a nearly uniform background of photons with a black body spectrum at a temperature of 2.7 K (see figure 2.4).

At the time where the Universe is approximately 380 000 years old, its high temperature around $\approx$ 3000 K causes all matter to be ionized. Therefore photons are not free streaming, but interacting electromagnetically with the charged ions. As the Universe expands and cools down, recombination starts, neutral elements form and the equilibrium interactions between photons and matter stop. After the photons experience the freeze out from former equilibrium, the ongoing expansion of the Universe effectively causes a red shift, thus the photon wavelength is nowadays on the microwave scale.
Measurements of the CMB with very high precision were done by the satellites Wilkinson Microwave Anisotropy Probe (WMAP)[8] and PLANCK [30]. The surveys revealed a highly uniform distribution of photons, yet there are small fluctuations on a scale of 60μK as shown in figure 2.5.

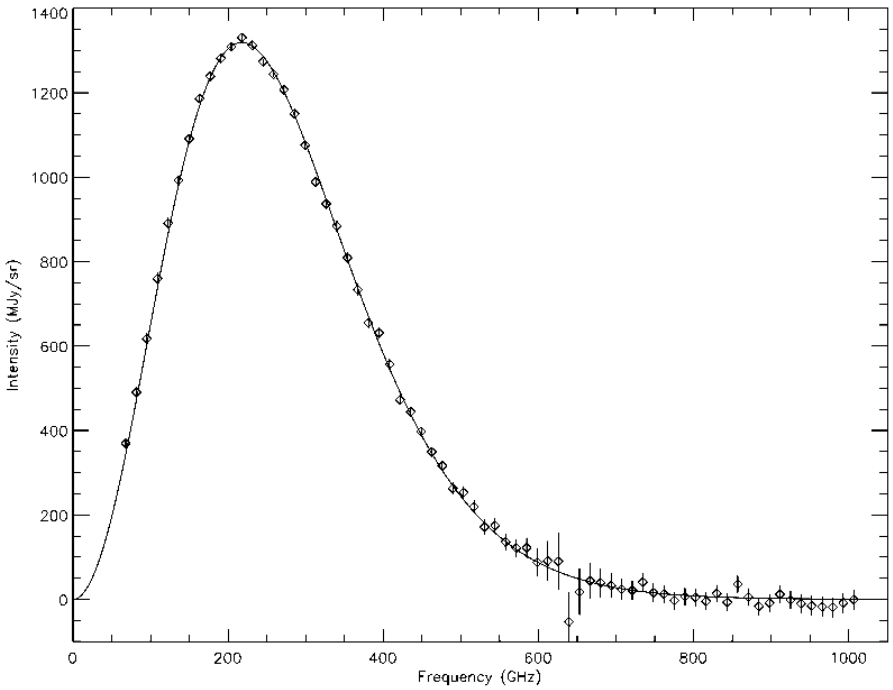

Figure 2.4.: Spectrum of the CMB showing behavior like a black body radiator at 2.7 K. The image is taken from [7].

In the early Universe over and under dense regions were present, which are caused by variations in energy density distribution. Photons leaving over dense regions get red shifted due to the gravitational potential they have to overcome, whereas photons in under dense regions undergo blue shifting. This effect of wavelength alterations by the gravitational potentials is called Sachs-Wolfe effect [31]. So, the anisotropies in the CMB directly link to density fluctuations in the early Universe [32].

The angular power spectrum of the temperature fluctuations in the PLANCK data shown in figure 2.5 reveals more about the processes at the time of recombination. The power spectrum shows a big peak around a multipole moment l of approximately 200 which is followed by two considerably smaller peaks. These peaks correspond to the effects of baryon acoustic oscillations. In the time before freeze out the baryon-photon plasma is in equilibrium. Over dense regions in the matter distribution start to attract more mass due to the higher gravitational potential. Counteracting to this attractive gravitational force is the radiation pressure of the photons which couple to the baryons in the hot plasma. The two opposing forces result in density oscillating baryon clouds. The first peak in the power spectrum corresponds to the largest matter cloud that

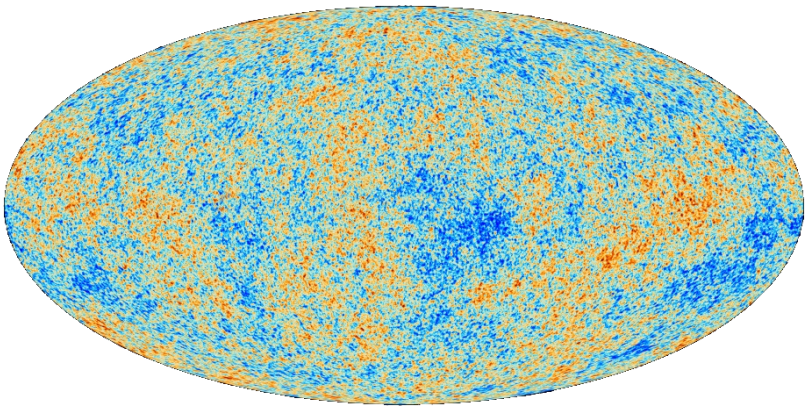

Figure 2.5.: Anisotropies of the CMB measured by PLANCK taken from [30].

could oscillate once before the photons freeze out. The position of this first peak reveals that the the Universe is flat. The smallness of the following peaks emanates from Silk damping [76], as smaller objects have too little gravitational mass, so radiation pressure drives these structures away. The fraction of peak heights with respect to the first acoustic peak, especially for the third peak, contains information about the ratio of baryons to the total amount of matter, as only baryons couple to photons. The discrepancy between the two matter contributions constitutes of non-baryonic dark matter. A fit containing all important cosmological parameters is applied to the power spectrum in order to determine the quantities, see figure 2.6, while assuming a ΛCDM model, a cosmological model with non-relativistic dark matter and dark energy[33].

The entire density Ω_{tot} consists of the baryon density Ω_{B}, the dark matter density Ω_{DM} and the amount of dark energy Ω_{DE},

$$\Omega_{\text{tot}} = \Omega_{\text{B}} + \Omega_{\text{DM}} + \Omega_{\text{DE}}. \tag{2.4}$$

The results of the PLANCK measurements within a 1σ error are

$$\Omega_{\text{B}}h^2 = 0.02264 \ \pm \ 0.00050 \qquad \text{as well as} \qquad \Omega_{\text{DM}}h^2 = 0.1138 \ \pm \ 0.0045, \tag{2.5}$$

which are given in units of the critical density

$$\rho_c = \frac{3H^2}{8\pi G} \tag{2.6}$$

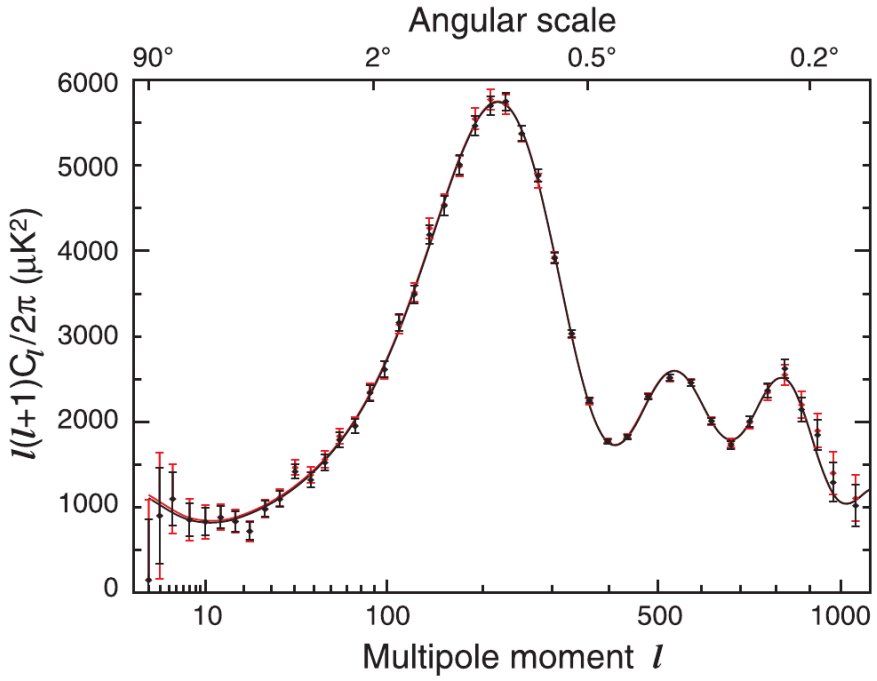

Figure 2.6.: Angular power spectrum of the CMB with best fit from ΛCDM model [33].

with the Hubble constant H. The relic density Ω in general is linked to the critical density ρ_c by

$$\Omega = \frac{\rho}{\rho_c}. \tag{2.7}$$

The Hubble constant H is typically given by

$$H = h \cdot 100 \frac{\text{km}}{\text{s Mpc}} \ . \tag{2.8}$$

The dependence of the PLANCK results on H is indicated by the h^2 terms in (2.5). This outcome emphasizes the presence of a non-baryonic dark matter component, which mostly interacts gravitationally.

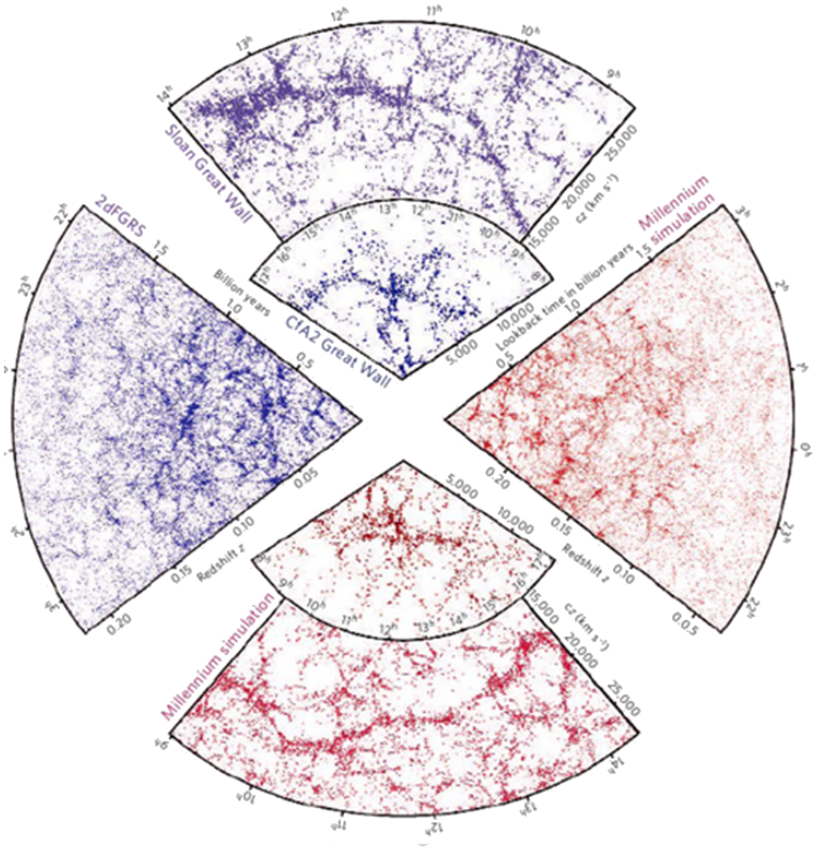

Figure 2.7.: Large scale structures in the Universe measured by the Galaxy Redshift Survey (blue) and simulated by the Millennium Simulation (red). Image taken from [36]

Structure Formation

As explained in the previous paragraph, density fluctuations in the early Universe could grow by attracting more and more mass due to gravitational effects. It is believed that dark matter clumps first and then baryonic matter could accumulate in the dark matter gravitational wells, small structures would grow ever larger over time attracting more and more matter as their gravitational potential grows. Today's large scale structures formed from such small deviations and are observed by satellites as in the Galactic Redshift Survey [34]. N-body simulations such as the Millennium simulation [35] emulate structure formation and compare the outcome to the survey observations with the amount of dark matter, which has to be non-relativistic (cold) at the time before recombination, as an important input parameter to match both results. Figure 2.7 shows

the structures measured by the Galaxy Redshift Survey (blue) and the outcome of the Millennium simulation (red). Both show similar large structure filaments with a lot of voids in between, the model of cold dark matter reproduces the observations rather well.

2.2. Dark Matter Candidates

The evidence reveals some properties of dark matter. It must be a non-baryonic particle with a specific relic density, as seen from PLANCK and the baryon acoustic oscillation. In order to be non-visible, it should be electrically neutral, colorless and collisionless. And as it is still present today, dark matter is stable or has at least a lifetime larger than the age of the Universe. Unfortunately it is not discovered yet, its nature is not revealed.

In the following, first different dark matter candidates are presented, then in the next section the production of WIMPs in the early Universe is described. The first part of this section deals with theories which are motivated by offsetting the Standard Model shortcomings. The second part presents models which extend the Standard Model in a minimal way.

There is a successful model describing the fundamental particles and their interactions in a quantum field theory approach, the Standard Model. It includes three of the four fundamental forces, the electromagnetic, the weak and the strong force, which are mediated by the associated gauge bosons. As the Standard Model is a gauge theory, its Lagrangian is invariant under the local gauge transformations. In this gauge invariant Lagrangian the particle content is described, the gauge bosons, the three families of quarks and leptons. In particular it contains a particle that is electrically neutral, colorless and interacts weakly: the neutrino ν. It would make the perfect dark matter candidate, but neutrinos were relativistic in the early Universe due to their small mass. Structure formation however needs some cold, non-relativistic dark matter. Also the neutrino abundance is way to little to account for the observed dark matter.

The Standard Model has more shortcomings than the explanation of dark matter[4]. There is a large variety of scales, as there is no explanation why the electroweak force is so much stronger than gravity. This so called hierarchy problem results in having a Higgs mass ($\approx$ 126 GeV) much smaller than the Planck scale ($\approx 10^{19}$ GeV). As the bare Higgs mass receives large radiative corrections, quadratic divergences occur. In principle it is possible to remove the divergences by renormalizing the masses, but this would require an unnatural amount of fine tuning. Also the Standard Model does neither contain gravity, nor does it give mass to neutrinos. There is no explanation in the Standard Model for the matter-antimatter asymmetry in the Universe. In addition to this, there is the strong CP problem: In principle the Standard Model Lagrangian should contain terms which break CP symmetry in strong interactions, but no CP

violation is experimentally observed. This non-observation would need a huge amount of fine tuning which appears unnatural. The Standard Model probably can be seen as an effective theory, which is a low energy approximation of a larger symmetry. In general the Standard Model agrees well with most electroweak precision test. If new particles are introduced, they should not interfere with these tests. Therefore new symmetries are needed or the new particle is so heavy that tree level contributions are suppressed and most contributions do not appear below loop level. New theories are built to handle the shortcomings, some of them, like Supersymmetry, address problems of the Standard Model and automatically contain a somewhat natural dark matter candidates. Others are solely designed to solve the dark matter issue and extend the Standard Model by a few particles only and eventually add new symmetries.

A lot of models feature a well motivated class of dark matter candidates, which are weakly interacting massive particles (WIMPs). They have weak scale annihilation cross sections around $3\times10^{-26}\mathrm{cm}^3\mathrm{s}^{-1}$ and masses of order hundreds of GeV in order to lead to the correct relic density, if thermally produced. This coincidence is often referred to as the 'WIMP miracle'.

2.2.1. Dark Matter in Larger Theories

Supersymmetric Dark Matter

Supersymmetry [4, 37, 38, 39] is a widely favored theory not only for its explanation of dark matter but also for its intrinsic elegance and the disposal of some Standard Model problems. Supersymmetry (SUSY) extends the Standard Model by adding a new symmetry between bosons and fermions in order to alleviate the hierarchy problem, as boson and fermion contributions enter the Higgs mass calculation with different signs. SUSY leaves internal gauge symmetries unchanged, therefore no additional forces appear. Additionally gauge coupling unification at high energies can be achieved with SUSY. If SUSY were an exact symmetry, each particle and its superpartner would share the same quantum numbers, except spin, and they would have the same mass. Since there is no observation of light SUSY particles in collider experiments [77], [78], SUSY itself cannot be exact, it is a broken symmetry.

In the MSSM [37, 4], the simples supersymmetric extension of the Standard Model, every Standard Model fermion obtains one bosonic superpartner, every boson is entangled with a SUSY fermion, at the minimum doubling the particle content of the Standard Model. Additionally in SUSY at least one extra Higgs doublet is needed to generate top and down quark masses and to avoid gauge anomalies [79].

As the same mechanism as in the Standard Model [80] accounts for spontaneous electroweak symmetry breaking, both SUSY Higgs doublets acquire vacuum expectation

values v_1 and v_2. Their initial eight degrees of freedom are reduced to five by unitary gauge transformation. The three missing degrees of freedom are transformed to give mass to the W and Z bosons. Each of the remaining degrees of freedom is manifest as a physical particle: two charged Higgs bosons $H^{\pm}$, one heavy and one light neutral scalar h^0, H^0 and a neutral pseudoscalar A^0.

To render the proton stable, a new discrete symmetry, R-parity, is needed. The R quantum number is

$$R = (-1)^{3B+L+2S} \tag{2.9}$$

with the baryon and lepton numbers B and L and spin S. Thus Standard Model particles, including all of the new Higgs sector, have R-parity 1 whereas SUSY partners have R-parity -1. Since B and L are additively conserved, R parity is multiplicatively conserved. This implies R-odd particles can only enter as pairs in production and annihilation processes. Hence the lightest R-odd, supersymmetric particle (LSP) is stable. The LSP then is a natural dark matter candidate and it is most common the lightest neutralino χ. It is a linear combination of the wino $\tilde{W}^3$ (the partner of the third component of the $\mathrm{SU}(2)_L$ triplet of weak gauge bosons), the U(1) bino $\tilde{B}$ and the two Higgsinos $\tilde{H}_1$, $\tilde{H}_2$ (the SUSY partners of the neutral Higgs components). So

$$\chi = \alpha\tilde{B} + \beta\tilde{W}^3 + \gamma\tilde{H}_1 + \delta\tilde{H}_2. \tag{2.10}$$

Neutralino LSPs as dark matter has been investigated in a lot of different works [37, 38, 39, 4]. The LSP as dark matter has strong model dependent features regarding its composition and therefore its interaction with other particles. This reflects in the corresponding values of relic density and cross sections for direct and indirect detection. The rich phenomenology of supersymmetric models is due to the large amount of free parameters and the wide range of parameter space.

The LSP can also be the superpartner of a neutrino, a sneutrino, which is excluded by direct detection experiments to be the dark matter candidate. The LSP could also be a gravitino, the SUSY partner of a graviton, the hypothetical gauge bosons of gravity, which is not a WIMP. Also electrically charged LSPs are experimentally excluded.

Kaluza-Klein Dark Matter

An attempt to unify electromagnetism, gravity and eventually strong and weak force is done in Kaluza-Klein (KK) theories [4, 43, 44, 45]. In these theories the Standard Model is related to a 3+1 dimensional surface embedded in a higher dimensional space. This space can have either flat or warped geometry, which influences particle properties.

The n extra dimensions of the higher space are compactified into a volume R^n.

The original theory by Kaluza and Klein [41, 42] proposes one extra spatial dimension. This fifth dimension is curled up in a small circle. It can be seen similar to a straw. From a distance it looks like a one dimensional line, but coming close, the circular dimension becomes visible, revealing a cylindrical surface. Particles moving in the direction of the curled up dimension will end after a short length at their starting point. This length is classified as the size R of the extra dimension. At low energies no extra dimension is visible. It will show up at an energy scale inversely related to its size R. Also a new scalar degree of freedom along the new dimension shows up, the radion. It is as well related to the size of the extra dimension. In principle it is possible to replace the circular U(1) symmetry by any Lie group. The underlying space is not necessarily the four dimensional space time but can be any Riemannian manifold or even a non-commutative space.

Naturally one expects standing waves along the extra dimensions with quantized invariant masses. The set of all possible excitations of one multidimensional field, which can propagate through extra dimensions, is called a Kaluza-Klein tower. The KK towers are manifest as four dimensional particles with increasing masses. The mass spectrum however is model dependent. At low energies only the corresponding massless, on the scale $1/R$, states are produced. The lightest Kaluza-Klein particle (LKP) corresponds to the smallest excitation. The non-observation of KK excitations in collider experiments sets upper limits on the scale R.

In order to provide a dark matter candidate among the KK excitations, a stabilizing symmetry is needed. There is indeed a discrete symmetry, Kaluza-Klein parity. It originates from conserved momenta along extra dimensions and is a remnant of a larger symmetry coming from the geometry of the higher dimensional space. KK parity remains unbroken in the case of universal extra dimensions, rendering the LKP stable. If l is the quantum number of the extra dimension corresponding to the excitations, $l = 0$ is for Standard Model particles and $l = 1$ characterizes the LKP. KK parity is given by $(-1)^l$, hence the LKP only enters in pairs to interactions with the Standard Model particles. The nature of the LKP itself is model dependent. For example it can be the lightest KK excitation of the hypercharge boson B^1 or the excitation of Z or Higgs bosons. If R is of order TeV^{-1} and the LKP is neutral with weak scale interactions, it can be a WIMP.

2.2.2. Minimal Dark Matter

Minimal dark matter models extend the Standard Model by few additional fields and probably a stabilizing symmetry. In the simplest model, dark matter is a real scalar [6], but one can also add a fermion, as well as extending the Standard Model not only

by one but by more new fields [2, 49, 50]. One example is the singlet fermionic model analyzed in this thesis. Also, minimal models can contain symmetries like $\mathbb{Z}_2$ symmetries or for example a $\mathbb{Z}_3$ symmetry or in general $\mathbb{Z}_n$ symmetries [51] which leads to more complicated models. As the singlet fermionic model and the two-component dark matter model are analyzed in this thesis, detailed information on the specific models can be found in the corresponding sections 3 and 4, so the following paragraphs only present a short overview.

Singlet Scalar Dark Matter

A new scalar field S is introduced in the Standard Model in order to account for the dark matter in the Universe. In the simplest of these models the scalar field is real and a singlet under the gauge transformation, thus neutral. To make it stable dark matter, a $\mathbb{Z}_2$ symmetry ($\phi \to \pm\phi$) is imposed, under which all Standard Model particles are even while S is odd. The only renormalizable interaction between S and the Standard Model particles is mediated by the Higgs and due to the $\mathbb{Z}_2$ symmetry S does not mix with the Higgs. As the hidden sector is only accessible by this Higgs portal, dark matter interacts weakly as long as the Higgs-scalar couplings are small enough.

Adding only one scalar field and a new symmetry to the Standard Model already creates a stable dark matter candidate within a framework which allows for easy analysis. The phenomenology of singlet scalar dark matter with respect to relic density, detection prospects and other aspects has been covered in great detail in some works [6, 47, 48, 66, 67, 68, 69, 70].

Fermionic Singlet Dark Matter

In the fermionic singlet model two fields are added to the Standard Model particle content, a Majorana fermion χ and a real scalar ϕ, which are both singlets under the SM gauge group. χ is odd under a new $\mathbb{Z}_2$ symmetry, while ϕ as well as all Standard Model particles are even, hence χ is stable dark matter

The introduction of two new fields makes it possible to formulate renormalizable interactions of the form $\bar{\chi}\chi\phi$ and $\bar{\chi}\gamma_5\bar{\chi}\phi$. Therefore this model can be see as a UV completion of the so called fermionic Higgs portal model, an effective field theory in which the mediator ϕ is heavy and thus integrated out [10]. Since ϕ and the Standard Model Higgs boson h are both even under the $\mathbb{Z}_2$ symmetry, mixing between the two occurs after electroweak symmetry breaking. The extended Higgs sector opens a window from the dark sector to the visible one.

Similarly to the singlet scalar model, this minimal extension of the Standard Model is easy to handle, so it offers a rich phenomenology, which can be easily confronted with

theoretical and experimental constraints, testing its feasibility. The model is investigated in some previous works [10, 18, 19, 21, 22, 1].

2.3. The Dark Matter Relic Density

The Boltzmann equation – see [40] – describes the evolution of WIMP number density with temperature in the early Universe.

For WIMPs with number density n_χ the Boltzmann equation is

$$\frac{\mathrm{d}n_\chi}{\mathrm{d}t} = -3Hn_\chi - \langle\sigma_{\mathrm{ann}}v\rangle\left(n_\chi^2 - n_{\chi,\mathrm{eq}}^2\right) \tag{2.11}$$

where t is time and H is the Hubble parameter, angle brackets denote a thermal average, which is explained in the appendix D. Normally one would expect statistical mechanical factors, which differentiate between fermions and bosons, but for massive particles, which decouple in the early Universe, these can be neglected – see [40]. The first term in (2.11) accounts for the expansion of the Universe, the second expression describes creation and annihilation of WIMP pairs in particle collisions. The next lines outline how to derive an expression for the Boltzmann equation (2.11), which can be treated numerically. As entropy is conserved,

$$\frac{\mathrm{d}s}{\mathrm{d}t} = -3Hs \tag{2.12}$$

is true for the entropy density s. Furthermore it is useful to introduce the abundance

$$Y := \frac{n_\chi}{s} \qquad \text{and a new variable} \qquad x := \frac{M_\chi}{T}.$$

Here T is the photon temperature which can be used equally to t as a time measure in the Universe. The Boltzmann equation (2.11) then is

$$\frac{\mathrm{d}Y}{\mathrm{d}x} = -\langle\sigma_{\mathrm{ann}}v\rangle\left(Y^2 - Y_{\mathrm{eq}}^2\right) + \frac{1}{3H}\frac{\mathrm{d}s}{\mathrm{d}x}. \tag{2.13}$$

To simplify further, the Friedmann equation

$$H^2 = \frac{8\pi}{3M_{\mathrm{Pl}}^2}\rho \tag{2.14}$$

is used where $M_{\mathrm{Pl}} = 1.22{\times}10^{19}$ GeV is the Planck mass and ρ is the mass energy density of the Universe. The relation of energy and entropy density to temperature is

$$\rho = \tfrac{\pi^2}{30} g_{\mathrm{eff}}(T) T^4, \tag{2.15}$$
$$s = \tfrac{2\pi^2}{45} h_{\mathrm{eff}}(T) T^3 \tag{2.16}$$

with the effective degrees of freedom $\mathrm{h_{eff}}$, $\mathrm{g_{eff}}$ of energy and entropy density. So $\frac{\mathrm{d}s}{\mathrm{d}x}$ can be calculated and the Boltzmann equation (2.13) leads to

$$\frac{\mathrm{d}Y}{\mathrm{d}x} = -\frac{45}{\pi M_{\mathrm{Pl}}}^{-1/2} \frac{g_*^{1/2} M_\chi}{x^2} \langle \sigma_{\mathrm{ann}} v \rangle \left(Y^2 - Y_{\mathrm{eq}}^2 \right) \tag{2.17}$$

where

$$g_*^{1/2} := \frac{h_{\mathrm{eff}}}{g_{\mathrm{eff}}^{1/2}} \left(1 + \frac{1}{3} \frac{T}{h_{\mathrm{eff}}} \frac{\mathrm{d}h_{\mathrm{eff}}}{\mathrm{d}T} \right). \tag{2.18}$$

as in [40].

Typically the Boltzmann equation (2.13) is treated numerically, since there is no analytical solution.

micrOMEGAs[72] is a tool, which is well suited to compute relic densities. The code utilizes a Runge-Kutta method to solve the Boltzmann equation (2.17), and provides a high precision, even in the presence of thresholds and resonances, which are rather important in some models. micrOMEGAs can also be used to calculate direct detection and annihilation cross sections as well as the neutrino flux from dark matter annihilation in the Sun.

For the numerical solution, one can chose the initial condition $Y = Y_{\mathrm{eq}}$ at $x \approx 2$ to obtain the WIMP abundance today Y_0. The relic density then is

$$\Omega_\chi h^2 = \frac{M_\chi \rho_0 Y_0 h^2}{\rho_C} = 2.742 \times 10^8 \frac{Y_0 M_\chi}{\mathrm{GeV}} \tag{2.19}$$

with the dark matter mass M_χ, the present entropy density ρ_0 and the critical density ρ_C.

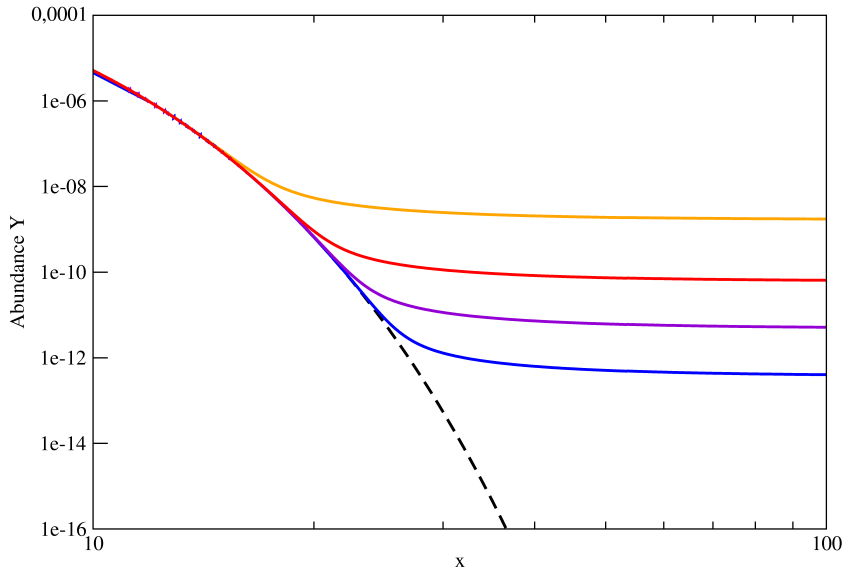

Figure 2.8.: Evolution of abundances Y and equilibrium abundance Y_{eq} with respect to x for increasing values of $\langle \sigma_{\mathrm{ann}} v \rangle$ from top to bottom.

Figure 2.8 shows the evolution of the WIMP abundance Y (colored solid lines) as a function of x for different values of $\langle \sigma_{\mathrm{ann}} v \rangle$, which increases from top to bottom. The equilibrium value Y_{eq} is shown as a solid line .

In the early Universe, the WIMPs are in equilibrium with the hot plasma, thus annihilation and creation processes equally take place in particle collisions. As a result the WIMP abundance follows the equilibrium distribution. The Universe cools down and the temperature decreases, so WIMP creation becomes suppressed by the Boltzmann factor $e^{-M_\chi/T}$, hence the WIMP density is decreased as annihilation processes are more abundant than WIMP creation. As the Universe not only cools but also expands, the expansion rate $3H$ becomes larger than the common annihilation rate, thus the mean free path of the WIMPs becomes larger than the size of the Universe. After this freeze-out the WIMP number density per comoving volume element stays constant. The exact freeze-out temperature depends on the WIMP annihilation cross section. The higher the cross section is, the longer the particles annihilate and the smaller the relic density $\Omega_\chi h^2$. If the WIMP relic density is smaller than the value measured by PLANCK [30], the WIMP is not particularly excluded as dark matter, but however, it cannot account for the entire dark matter, there has to be another contribution

2.4. Dark Matter Searches

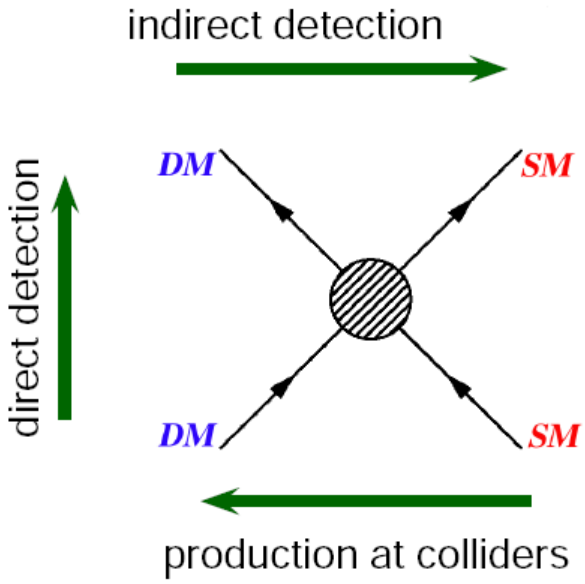

Figure 2.9.: Dark matter (DM) interaction with Standard Model (SM) particles providing different channels for searches, taken from [81].

Despite the huge variety of evidence and models for dark matter, it is not clear how it is realized in nature, hence many experiments are set up to look for this new kind of matter. Basically there are three kinds of experiments searching for dark matter at the moment: direct, indirect and collider experiments. All focus on the small non-gravitational interaction of dark matter with ordinary matter, as shown in figure 2.9. Direct detection aims at the interaction between dark matter and a given detector material. This field contains a huge variety of experimental techniques, setting strongest limits on dark matter parameters. Indirect detection aims at observing signals from dark matter annihilation. There are several annihilation products which might be more or less suited to give rise to a noticeable signal. In particle colliders one can search for the signature of pair production of dark matter when colliding two particles at high energies. It is unlikely that collider experiments will claim a discovery of dark matter, but they can put limits on the parameter space. All three kinds of experiments are complementary, so a signal in one type can be confirmed or falsified by the others. The different detection approaches are described in more detail in the following paragraphs.

2.4.1. Direct Detection

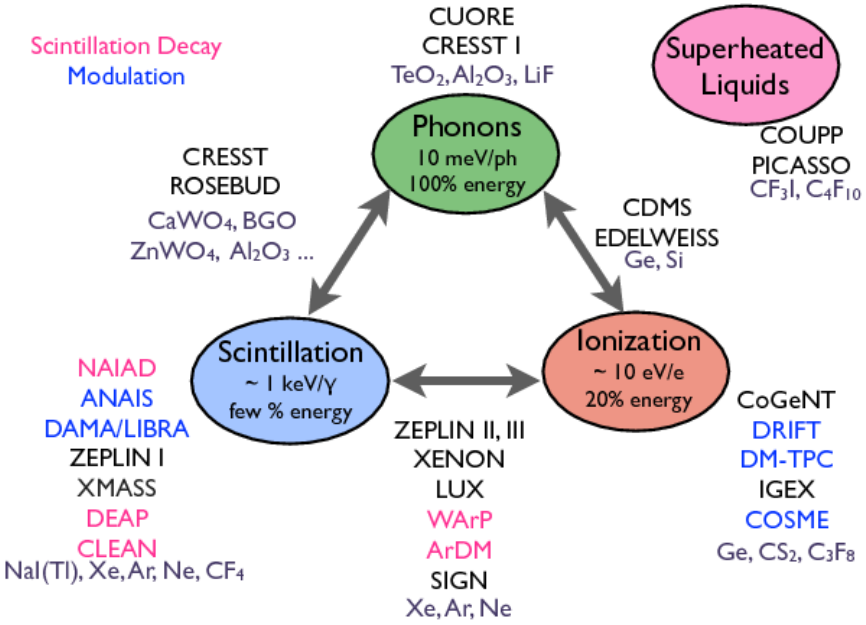

Figure 2.10.: The three channels for dark matter nucleus interactions including specific experiments which use the specific channels, taken from [82].

When the Sun orbits around the galactic center, it passes through the dark matter distribution with a given velocity, hence there is always a dark matter flux through the Earth. Direct detection experiments aim at this flux. When WIMPs hit the target material, they can interact with its nuclei and produce a nuclear recoil. There are two possible ways of WIMP-nucleon coupling, a spin-independent interaction, as WIMPs couple to mass, and probably a spin-dependent interaction, as WIMPs could also couple to spins. In a spin-independent collision, the WIMP couples coherently to the nucleus, the A nucleons in the nucleus all contribute to the scattering process, thus the total cross section is proportional to A^2. In a spin-dependent event, paired nucleons do not contribute to the scattering, only the spins of free unpaired nucleons add up. In order to probe this, the target material has to contain odd isotopes.
There are three basic signals, as shown in figure 2.10, that can be induced by WIMP nucleon scattering: charge, light and heat. The interaction can ionize the material and therefore produce charges, light can be emitted in scintillation processes and heat can

originate from the deposited energy. If the material is a suitable solid state, this can give rise to phonons. If an experiment uses two of the signatures, it is easier to differentiate whether an event is a dark matter induced nuclear recoil or an electron recoil caused by another interaction. Currently there are three main types of detectors: cryogenic detectors, noble liquid detectors, and super heated bubble chambers.

Cryogenic Detectors

Experiments like CRESST [54] or CDMS [55] use ultra-cool germanium or silicon crystals in the milli-Kelvin temperature range. When a WIMP hits these crystals, the temperature change creates phonons, which propagate in the crystal. The rise time of the phonons and the pulse shape allow to reconstruct the original event position within the detector. This is a nice feature for background suppression, as it is possible that nuclear recoils occur due to neutrons. These events are most likely to happen close to the detector surface, since neutrons cannot penetrate deep before being stopped. Another accessible channel is ionization from the nuclear recoil, allowing a good discrimination between nuclear and electronic recoils.

Noble Liquid Detectors

XENON [24], LUX[26] and other noble liquid detectors use a large volume of cooled noble liquid or a dual phase approach with noble gas. A WIMP interacting with the cooled liquid can lead to ionization and scintillation. This dual channel read out allows for good event discrimination by the charge to light ratio, as the energy deposited per photon differs for electronic and nuclear recoils. These kinds of detectors also allow for good position reconstruction, thus the background can be reduced by looking at the inner volume only, for the same reason as for cryogenic detectors.

Superheated Gas Detectors

Detectors like PICASSO[56] work in a similar way to bubble chambers. They are filled with superheated gas, which undergoes a phase transition when a recoil deposits energy. The temperature and pressure variations give rise to bubbles and allow for event discrimination.

All direct detection experiments have to deal with a large background which needs to be reduced as much as possible, thus the detector material has to be non-radio active. Also most detectors are surrounded by heavy shielding and located underground to eradicate cosmic rays. Fiducializing the volume, as explained before, lowers the background further. It is possible to avail an active veto to reject multiple scattering events, which are most likely not caused by dark matter. If the sensitivity of future experiments continues to increase, at some point the background neutrinos will be visible in the detectors. This is a background which cannot be alleviated.

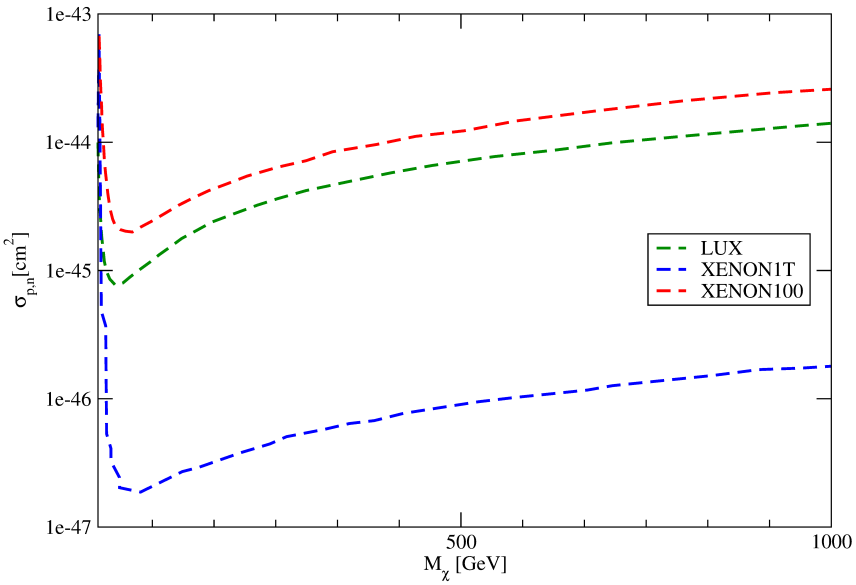

Figure 2.11.: Exclusion curves from direct detection experiments, data taken from [90, 26].

Figure 2.11 shows the current bounds and the expected sensitivities on the spin-independent cross section as a function of dark matter mass. The lines mark the sensitivity of the labeled experiments. Currently leading on the field is LUX (green line). XENON100 (red line) has the second best sensitivity. Since there has been no discovery yet, all parameters above the curves are excluded. Future experiments are under construction, as XENON1T[25] and LZ [91], which work with the same principle as XENON100 but are scaled up to contain about 1 ton of Xenon ore more in an active volume. The goal is to increase sensitivity in order to probe more and more of the parameter space. The expected reach of XENON1T (blue line) is also shown in figure 2.11.

2.4.2. Indirect Detection

Indirect detection experiments like FERMI-Lat[57], PAMELA[58] or IceCube[27] search for the signature of dark matter annihilating in the Universe. In order to produce a feasible signal, the annihilation products need to be detectable and stable enough to reach the detector, such as photons, neutrinos and antimatter. Unstable particles as

the W and Z bosons can produce stable detectable particles in subsequent decays. In order to have an observable signature from dark matter annihilation, it is favored to focus on regions with an enhanced dark matter density such as the Galactic center or the Sun. In the following the main messengers for indirect detection are described.

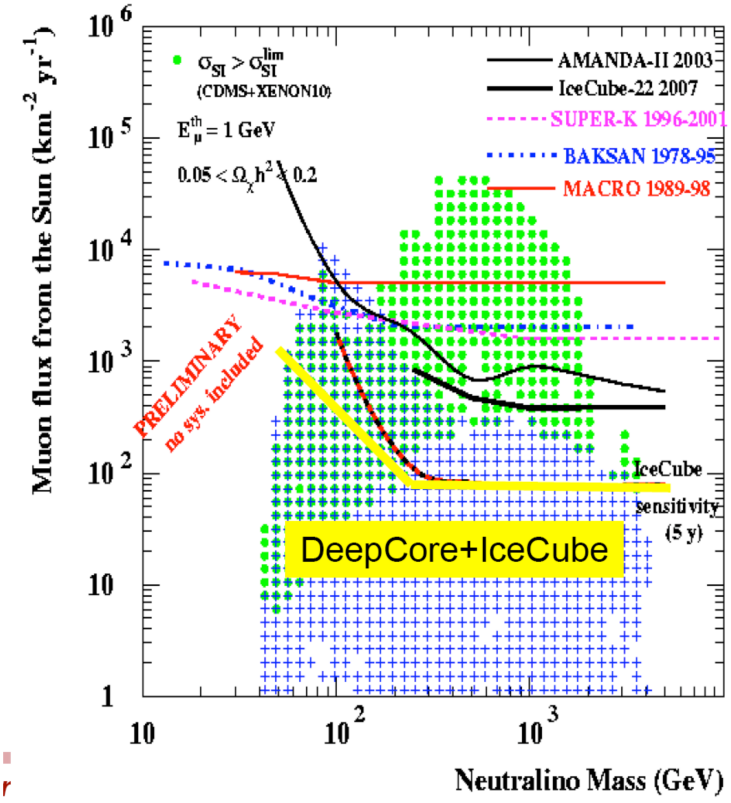

Figure 2.12.: The plot shows the sensitivity of different experiments for the muon flux from solar neutrinos [27].

Photons

For photons at such high energies, as expected for WIMP annihilation, there is only little deflection by charged particles and scattering off of background photons. So they propagate nearly free in the Universe. Unfortunately the coupling of dark matter to

photons is highly suppressed, thus the expected signal is small. The methods for γ-ray detection are well engineered, but there is a rich background for photons in the Universe, which makes signal identification rather complicated. Even if a signal looks like dark matter, the gamma-rays could come from a not yet understood astrophysical source. Present experiments like Fermi-LAT [57] have made significant progress in this field and have started to probe the parameter space consistent with WIMP dark matter.

Antimatter

Space based detectors are used to look for antimatter signals. WIMP annihilation often favors the production of positrons and anti-protons. Since antiparticles are charged, they undergo diffusion and scatter multiply while traveling through the intergalactic medium. There is no back-tracing to a specific source, still it is possible to extract antimatter signals from cosmic rays with spaceborn experiments such as PAMELA [58] and AMS-02 [92].

Neutrinos

It is more difficult to detect neutrinos, but they travel straight from their origin nearly unaffected by the medium in between, only the neutrino flavor can be affected by neutrino oscillation. Fortunately, most of the background neutrinos have energies way below the expected signal from WIMP annihilation. This makes the searches with neutrino telescopes as IceCube [27] promising, as well as the fact that a lot of Standard Model particle decays feature neutrinos and subsequent decays are likely to produce a neutrino signal. Figure 2.12 combines the current sensitivity with respect to muon flux, which comes from neutrinos from the Sun interacting with the target material, of the IceCube[27, 29] neutrino telescope with the reach of other experiments.

2.4.3. Collider Searches

Particle colliders such as the LHC at CERN [4, 84, 85] may offer insight into the dark matter nature. By not observing for example the Higgs decaying to dark matter as favored in the Higgs portal dark matter models, bounds on the couplings and mass of dark matter are obtained [59]. In addition one can also search for the direct production of dark matter particles. Once produced in collision the dark matter particles simply travel through the detector without interacting. Thus the typical signature accompanying dark matter production is missing energy. To trigger the detector, however, another visible particle must be present. Monojet searches, for example, analyze the pair production of dark matter particles accompanied by a gluon, giving rise to a single jet. The limits from monojet studies are included in figure 2.13.

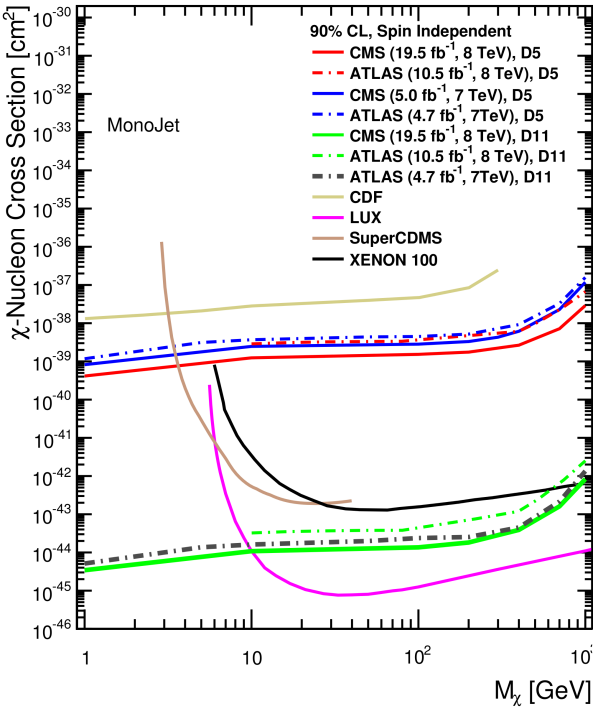

Figure 2.13.: Recent bounds on dark matter nucleon cross sections including collider searches. Image taken from [60]

3. Fermionic Singlet Dark Matter

The fermionic singlet model adds two new fields to the Standard Model particle content. One Majorana fermion χ, which is the dark matter, and one real scalar ϕ. The Lagrangian for χ includes all renormalizable interactions between χ and ϕ. It is

$$L = -\frac{1}{2}\left(M_\chi \overline{\chi}\chi + g_s \phi \overline{\chi}\chi + g_p \phi \overline{\chi}\gamma_5 \chi\right) \tag{3.1}$$

where M_χ is the mass of the fermion, g_s is the scalar coupling, providing parity conserving interactions, and g_p is the pseudo-scalar coupling, giving rise to parity violation.

A new $\mathbb{Z}_2$ symmetry is introduced, which is similar to R-parity in SUSY, to render χ stable, as it is odd under the $\mathbb{Z}_2$, whereas ϕ and all other Standard Model particles are even. The scalar potential in this framework is

$$\begin{aligned} -V(\phi, H) =& \mu_H^2 \left(H^\dagger H\right) + \lambda_H \left(H^\dagger H\right)^2 - \frac{\mu_\varphi^2}{2}\phi^2 + \frac{\lambda_\varphi}{4}\phi^4 + \\ & \frac{\lambda_4}{2}\phi^2 \left(H^\dagger H\right) + \mu_1^3 \phi + \frac{\mu_3}{3}\phi^3 + \mu\phi \left(H^\dagger H\right). \end{aligned} \tag{3.2}$$

and in the process of electroweak symmetry breaking the Higgs boson acquires a vacuum expectation value v, analogous to the symmetry breaking mechanism in the Standard Model [80]. In principle ϕ could obtain a vacuum expectation value as well, but it is possible to shift the fields by an appropriate basis choice so that it vanishes [83]. All transformations and derivations regarding the potential (3.2) are shown in the appendix E. With the basis transformation only the μ term in the potential (3.2) contributes to the mixing of ϕ and h, offering a simplified description of the phenomenology. Furthermore the parameter μ_1 is no longer free, but equal to $\mu_1^3 \frac{\mu v^2}{2}$. In order to bound the potential from below, the conditions λ_H, $\lambda_\phi > 0$ and $\lambda_4 >$ -2 $\sqrt{\lambda_\phi \lambda_H}$ are imposed. h and ϕ mix with each other and give rise to the mass eigenstates H_1 and H_2 given by

$$\begin{aligned} H_1 &= h\ \cos\alpha + \phi\ \sin\alpha, \\ H_2 &= \phi\ \cos\alpha - h\ \sin\alpha \end{aligned} \tag{3.3}$$

where α is the mixing angle between h and ϕ, which is taken to be a free parameter of the model. At the LHC a Standard Model-like Higgs was observed [86, 87, 88, 89], so M_{H_1} is set to 125 GeV. In order to maintain one Standard Model-like Higgs, α has to

be small, then H_1 corresponds mainly to h whereas H_2 is mostly ϕ. To get a handle on how well H_1 fits the Standard Model expectation, the signal strength reduction factor r_1 is defined according to [10],

$$r_1 = \frac{\sigma_{H_1} Br_{H_1 \to X}}{\sigma_{H_1}^{SM} Br_{H_1 \to X}^{\mathrm{SM}}} \tag{3.4}$$

where σ_{H_1} is the H_1 production cross section, $Br_{H_1 \to X}$ is the branching ratio for H_1 to any final state X and Γ_{H_1} is the decay width of H_1, all for the extended model. A superscript SM denotes the same quantities for the Standard Model. r_1 measures the reduction in numbers of events for H_1 decaying to final states X with respect to the Standard Model. Throughout the whole analysis $r_1 > 0.9$ is imposed. Moreover, the focus is on the region of the parameter space where processes like $H_1 \to \chi\chi$ or $H_1 \to H_2 H_2$ are kinematically forbidden. In the framework of this model r_1 can be simplified to

$$r_1 = \cos^4 \alpha \frac{\Gamma_{H_1}^{\mathrm{SM}}}{\Gamma_{H_1}}, \tag{3.5}$$

in which Γ_{H_1} is the total decay width of H_1. So the constraints on r_1 result directly in constraints on α. Incorporating the non-observation of a second Higgs like H_2 at the LCH, the signal strength reduction factor r_2 for H_2, similarly defined, simplifies to

$$r_2 = \sin^4 \alpha \frac{\Gamma_{H_2}^{SM}}{\Gamma_{H_2}}. \tag{3.6}$$

It has to remain smaller than 0.1 to match the bounds. However, this constraint is weaker than that obtained for r_1.

One is left with eight free parameters in general:

$$M_\chi, M_{H_2}, g_s, g_p,\ \alpha,\ \lambda_4,\ \mu_3,\ \lambda_\phi.$$

In the parity conversing case the requirement $g_p = 0$ reduces the number to seven. The parameters, except M_χ, g_s and g_p, are linked to the parameters in the scalar potential as shown in the appendix E.

The fermionic singlet model was already investigated in some previous works [18, 19, 20, 21, 22]. Still this thesis features some new aspects of this model, while examining the viable parameter regions and investigating detection prospects both for direct and indirect detection.

As the fermion χ is thermally produced, it achieves its relic density by a freeze-out mechanism. In order to be a potential dark matter candidate, χ has not only have to have the correct relic density, but its direct detection cross section has to be below present bounds. To treat this properly, the Lagrangian is modeled in LanHep [71] and then implemented in micrOMEGAs [72], which takes into account all resonance and threshold effects and calculates relic density, direct detection cross sections and the neutrino flux from dark matter annihilation in the Sun.

Regarding direct detection, the scattering of dark matter particles off nuclei is spin-independent and takes place through the two t-channel diagrams in figure 3.1.

Figure 3.1.: Feynman diagrams providing spin-independent elastic scattering of dark matter particles off nuclei.

Thus it is mediated by the two scalars H_1 and H_2 and the elastic-scattering cross section σ_{SI} for χ on a proton is given by (cf. appendix F)

$$\sigma_{\mathrm{SI}} = \frac{g_s^2 \sin^2 2\alpha}{4\pi} M_r^2 \left(\frac{1}{M_{H_1}^2} - \frac{1}{M_{H_2}^2} \right)^2 g_{\mathrm{HP}}^2, \tag{3.7}$$

where M_r is the reduced mass of the dark matter proton system and

$$g_{\mathrm{HP}} = \frac{M_p}{v} \left[\sum_{q=u,d,s} f_q^p + \frac{2}{9} \left(1 - \sum_{q=u,d,s} f_q^p \right) \right] \approx 10^{-3}, \tag{3.8}$$

where the micrOMEGAs default values have been used for the form factors f_q^p. As the proton mass M_p is much larger than the dark matter mass M_χ,

$$M_r = \frac{M_\chi M_p}{M_\chi + M_p} \approx M_p. \tag{3.9}$$

is a valid approximation. Thus the cross section σ_{SI} is basically independent of M_χ and proportional to $g_s^2 \sin^2\alpha$ as $\sin^2 2\alpha \propto \sin^2\alpha$. Especially, the direct detection cross section independent of g_p. The annihilation rate, however, which is important for indirect detection and the relic density, includes a term proportional to the dark matter velocity and one term which is proportional to g_p.

In a previous work [10] three options to be consistent with the latest experimental limits for direct detection were identified. The *pseudo scalar Higgs portal* allows only parity violating interactions, mediated by the term $(\phi\bar{\chi}\gamma_5\chi)$ in the Lagrangian (3.1). Hence dark matter annihilation receives a contribution which is not velocity suppressed. So it is possible to evade direct detection, while still fulfilling the relic density constraint. Another way is the enhancement of the annihilation cross section close to the Higgs resonances, either for H_1 or H_2. This is called *resonant Higgs portal*. The last case is the *indirect Higgs portal*, where the process $\chi\chi \to H_2H_2$ is dominant. In this work a new *indirect Higgs portal* via H_1H_2 is found which allows to find viable models above the H_2 resonance but below $M_\chi = M_{H_2}$. In addition, a detailed analysis of the parameter space of the model and of the future prospects for detection is performed. Specifically, the parameter space which is already excluded by XENON100 data [24] and the one that will be probed by XENON1T [25] are identified. Finally the expected signal from dark matter annihilation in the Sun is calculated and compared against the sensitivity of IceCube [27]. It is found to be convenient to divide the analysis of this model into two parts. First it starts with the parity conserving one and then one comes to the most general case which allows for parity violation.

3.1. Parity Conserving Case $g_p = 0$

Throughout this section only parity conserving interactions are treated, so the pseudo scalar coupling g_p is set to zero. First regions consistent with the relic density constraint are identified, then direct detection bounds and prospects are analyzed, and finally, indirect detection is described.

In order to start with a short illustration, figure 3.2 shows the relic density Ωh^2 (red line) with respect to M_χ for a fixed set of parameters. The relic density constraint $\Omega h^2 \approx 0.11$ is shown as a black line. The relic density varies over a large spectrum from 10^{-3} up to 10^5 depending on M_χ, it is largest for small values of M_χ, at high values of M_χ the relic density increases with mass. Starting from low masses, the relic density decreases slightly until a large dip appears around 62.5 GeV. This corresponds to the H_1 resonance where $2M_\chi = M_{H_1}$ and thus the annihilation rate is enhance. Similarly the dip at 100 GeV, which equals $\frac{1}{2}M_{H_2}$, refers to the H_2 resonance. The smallest relic densities are obtained at this resonance due to a largely enhanced annihilation rate. After the H_2 resonance the relic density increases with M_χ until a steep drop

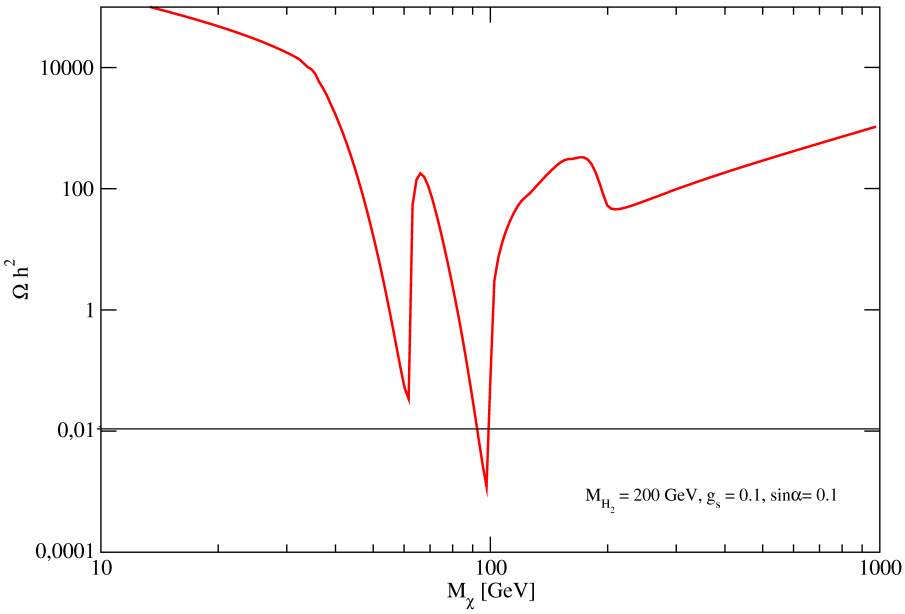

Figure 3.2.: The relic density of χ for varying mass M_χ, while the mass of H_2 is fixed at 200 GeV, g_s equals 0.1 and $\sin\alpha$ equals 0.1. The black line is the relic density constraint of $\Omega h^2 \approx 0.11$.

at $M_\chi = 200\text{GeV} = M_{H_2}$, when the channel $\chi\chi \to H_2H_2$ opens up. In principle the opening of the channel $\chi\chi \to H_1H_1$ could also be seen, but it is overlaid by the resonances. For this set of parameters it is only possible to achieve the right relic density at the resonances. This first example shows, that the relic density can vary over a large range strongly depending on model parameters.

To investigate the viable parameter space further, a random scan was done allowing the parameters of the model, except g_p $(= 0)$, to vary freely over the ranges given in table 3.1. 10^5 models fulfilling the relic density constraint are obtained. In the following this sample will be used to analyze in detail the phenomenology of this model.

Figure 3.3 shows all the viable models in the plane (M_χ, M_{H_2}). The figure also displays the four possible dominant annihilation final states, W^+W^- (blue squares), H_1H_1 (black stars), H_1H_2 (orange crosses) and H_2H_2 (green circles). The final states do not necessarily feature Standard Model particles. The entire plane is filled with parameter

Table 3.1.: Range of free parameter in the numerical investigation of the singlet fermionic model.

Parameter	Range	
M_χ	(50-1000)	GeV
M_{H_2}	(150-1000)	GeV
μ_3	$\pm(10^{-4}\text{-}10^{4})$	GeV
g_s	$\pm\pi(10^{-4}\text{-}1)$	
g_p	$\pm\pi(10^{-4}\text{-}1)$	
λ_4	$\pm\pi(10^{-4}\text{-}1)$	
α	$\pi(10^{-5}\text{-}1)$	

points, as the relic density constraint does not exclude any region of (M_χ, M_{H_2}). It is always possible to choose the other parameters accordingly.

The red dashed line marks the H_2 resonance around $2M_\chi = M_{H_2}$. Below the H_2 resonance, to the left of the dashed line, the annihilation channels featuring H_2 are closed and dark matter only annihilates to Standard Model particles, most common to W^+W^-, but few feature H_1H_1 as the dominant final state. Above the H_2 resonance final states with H_2 become accessible. Close to the resonance the final state H_1H_2 dominates, whereas for larger masses ($M_\chi > M_{H_2}$) the major contribution is from annihilation to H_2H_2. Final states featuring H_2 receive contributions independent of α, whereas all couplings of dark matter to the Standard Model particles depend on the mixing angle α, for comparison the Feynman rules are given in the appendix C.1.

Regarding the phenomenology of the singlet fermionic model, the H_2 resonance is crucial, therefore it is called *the resonance* in the following sections. It is useful to classify parameter points with respect to the resonance, models with $2M_\chi \leq 0.9M_{H_2}$ are labeled *below the resonance*, models *above the resonance* are models with $2M_\chi > 1.1M_{H_2}$ and models featuring $0.9M_{H_2} \leq 2M_\chi \leq 1.1M_{H_2}$ are considered *on the resonance*. Even though the classification is somewhat arbitrary, it will be seen that it helps in understanding the phenomenology.

Figure 3.4 shows all viable models projected onto the $(g_s, \sin\alpha)$ plane. The models are divided into three classes. Models below the resonance are displayed as blue squares, models above the resonance as orange circles and models on the resonance are shown as red crosses. Most models on the resonance feature $\sin\alpha$ larger than 10^4 and can take nearly any value of g_s in the shown range. Notice that g_s is never smaller than about 0.01. Non-resonant models mostly take values of g_s smaller than 0.1, as the annihilation cross section is proportional to g_s^2, which should be around 3×10^{-6} cm^3/s to produce the right relic density. Most models above the resonance attribute g_s larger than 0.1 and

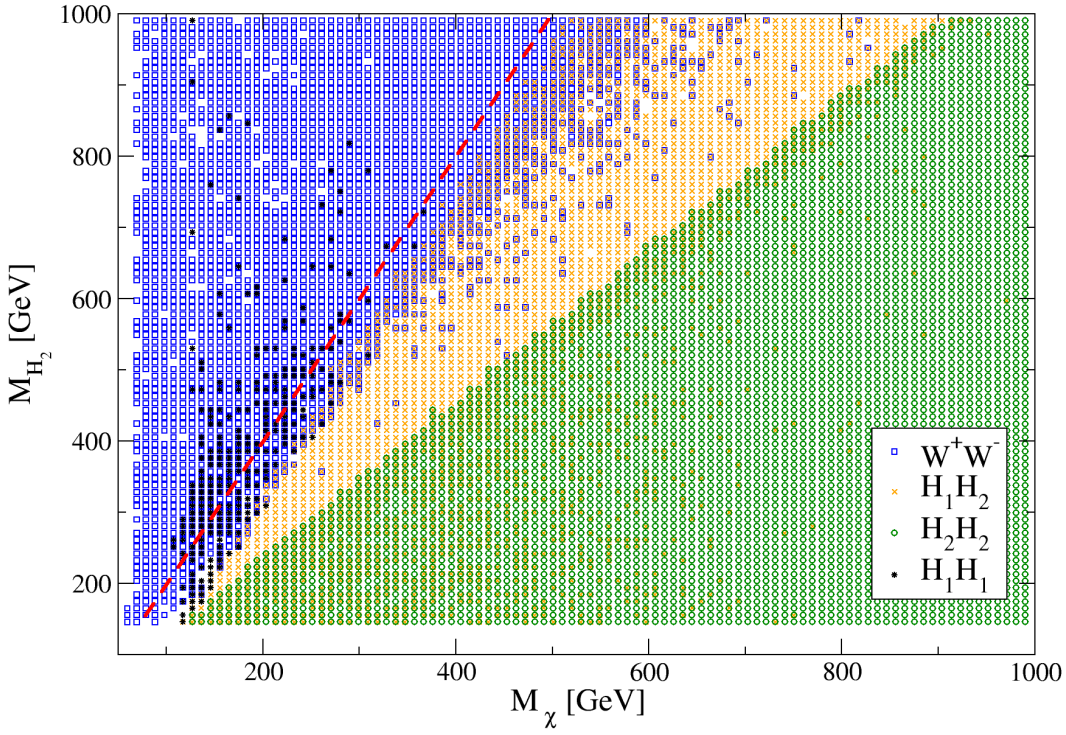

Figure 3.3.: Models which are conform with the relic density constraint projected on the (M_χ, M_{H_2}) plane. The red dashed line shows the resonance condition $2M_\chi = M_{H_2}$. Different symbols are used to indicate dominant annihilation channels.

have no limit on $\sin\alpha$. Models below the resonance are concentrated in the upper right corner of the plane and $\sin\alpha$ is always larger than about 0.002. The triangular shape of the distribution stems from the fact that the product of $\sin\alpha$ and g_s can not be very small since the annihilation cross section into Standard Model particles is proportional to $g_s^2 \sin^2\alpha$.
The link between the product $|g_s|\sin\alpha$ and dark matter mass is illustrated further in figure 3.5, projecting all models onto the plane $(M_\chi, g_s \sin\alpha)$ with different symbols to mark the position of the models with respect to the resonance. The choice of symbols is the same as in figure 3.4. Due to the chosen parameter range, models below and on the resonance are restricted to the low mass area, M_χ cannot go above 450 GeV respectively about 550 GeV. For models below the resonance the cross section is proportional to the product of g_s and $\sin\alpha$, so it cannot be smaller than about 0.001 and is largest for small masses. For resonant models, unlike models below the resonance, the product $g_s \sin\alpha$ can never be very large, having an upper limit of about 0.1. Otherwise, the relic

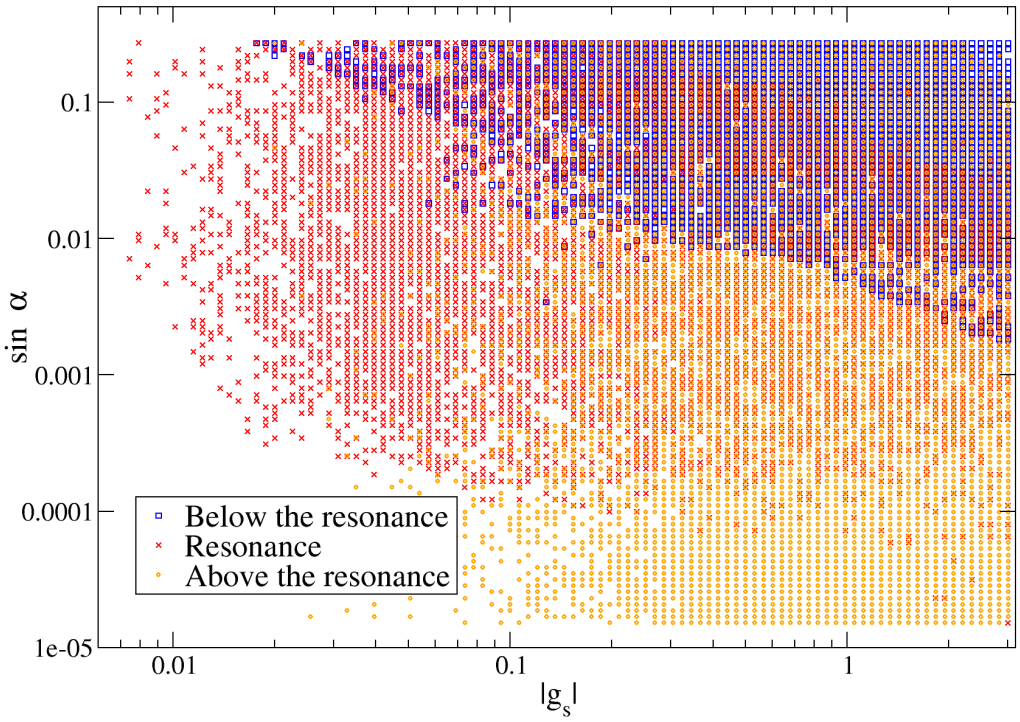

Figure 3.4.: Models which are conform with the relic density constraint projected on the $(g_s, \sin\alpha)$ plane. Different symbols are used to distinguish the models on, below and above the resonance.

density would be too large because of the enhanced annihilation around the resonance (cf. figure 3.2). Models above the resonance fill nearly the entire parameter space and can take any value of $|g_s| \sin\alpha$, since once the resonance is crossed, the annihilation channels $\chi\chi \to H_1 H_2$ and $\chi\chi \to H_2 H_2$ become accessible.

The process $\chi\chi \to H_1 H_2$ is particularly relevant, because it was not considered in previous works. Three diagrams contribute to this process – see figure 3.6. In agreement with the Feynman rules for this model (cf. appendix C.1) the first diagram (a) is proportional to $\sin\alpha$, the second one (b) is suppressed by $\sin^2\alpha$, but the third diagram (c) is independent of $\sin\alpha$ and only set by the product $g_s\lambda_4$. Hence the independence of α, the relic density constraint can be satisfied while still allowing small couplings.

This new kind of *indirect Higgs portal* with $\chi\chi \to H_1 H_2$ is presented in figure 3.7, as all models featuring $H_1 H_2$ as a dominant annihilation channel are projected onto the plane $(M_\chi, |g_s\lambda_4|)$.

Two regions of $\sin\alpha$ are chosen in order to highlight the dependence on the mixing angle α. Models with a value of $\sin\alpha$ smaller than 0.01 are marked with blue squares,

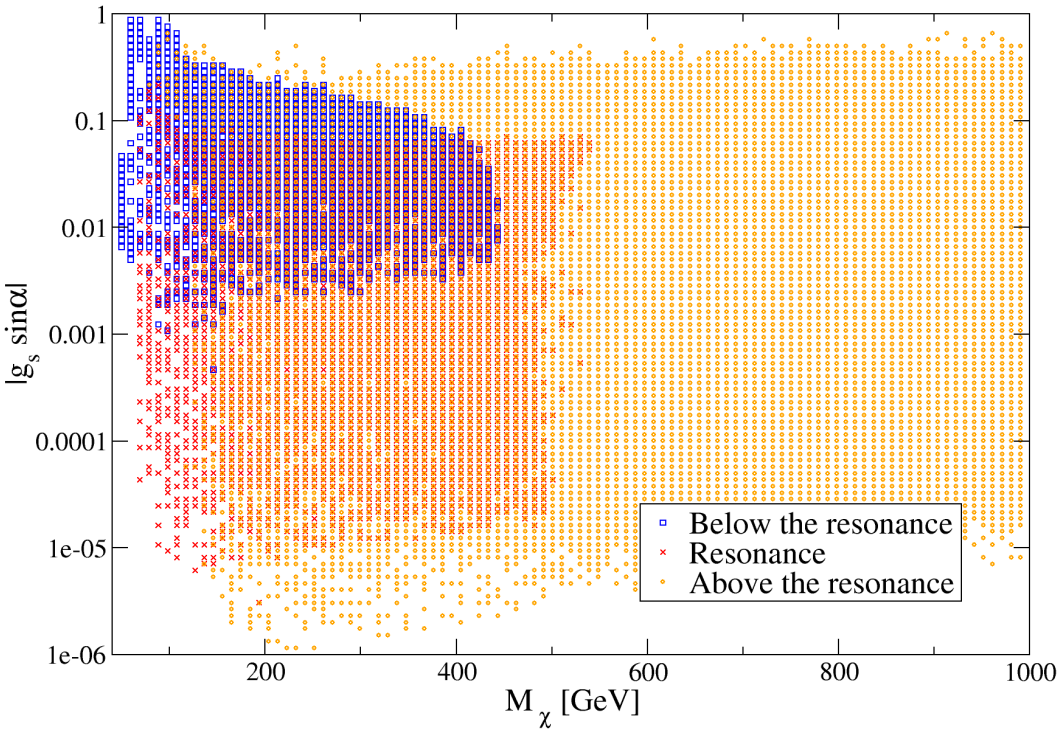

Figure 3.5.: The regions of the plane $(M_\chi, g_s \sin\alpha)$ which are conform with the relic density are shown, with different symbols to distinguish the models on, below and above the resonance.

models with larger values are displayed as orange crosses. For points with small values of $\sin\alpha$, the contributions of the diagrams (a) and (b) shown in figure 3.6 are largely suppressed. Hence the product of $|g_s\lambda_4|$ is never very small, all points are concentrated around a narrow band which covers the whole span of M_χ. As $\sin\alpha$ takes larger values, the suppression is relieved. The influence of the above diagrams becomes relevant, allowing $|g_s\lambda_4|$ to take much smaller values as indicated by the orange crosses filling the whole plane.

3.1.1. Direct Detection Bounds and Prospects

After examining the parameter space compatible with the relic density constraint, it is interesting to see how the viable regions are influenced by the current direct detection limits from XENON100 [24] and which parameter ranges will be probed by future experiments like XENON1T[25].

The spin-independent direct detection cross section σ_{SI} is nearly independent of M_χ

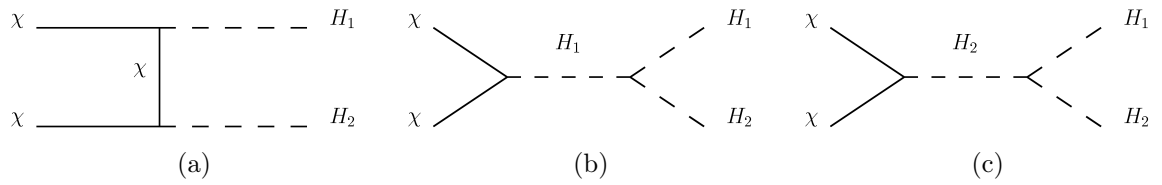

Figure 3.6.: Feynman diagrams contributing to $\chi\chi \to H_1 H_2$.

and proportional to $g_s^2 \sin^2\alpha$, see equation (3.7). Hence, direct detection constraints can exclude extensive areas of the parameter space for this model as shown in [10, 22]. Similarly to their studies, figure 3.8 illustrates the dependence of the spin-independent cross section σ_{SI} on the dark matter mass M_χ for two different fixed values of M_{H_2}.

The green solid line represents the current XENON100 limit and the dashed line shows the expected sensitivity of XENON1T. The current results from LUX would lie slightly below the XENON100 curve. Blue squares are points for $M_{H_2} = 500$ GeV whereas the red crosses display the distribution for $M_{H_2} = 900$ GeV. For both values of M_{H_2} the cross section clearly is suppressed at the resonance featuring a drop over six orders of magnitude around $2M_\chi = M_{H_2}$. Below the resonance all points are cumulated in a narrow band, since the cross section σ_S and the relic density both depend on $\sin\alpha$. Above the resonance, the relic density receives a contribution independent of $\sin\alpha$ originating from the newly opened channels $\chi\chi \to H_1 H_2$ and $\chi\chi \to H_2 H_2$. Hence σ_{SI} can vary over several orders of magnitude. Taking into account the bounds from the XENON100 experiment, viable models can be identified. Models above the XENON100 curve are within the reach of the detector and thus excluded. Interestingly, non-excluded models can even be found in regions below the resonance, for $M_{H_2} = 500$ GeV they start to occur at M_χ around 200 GeV, for $M_{H_2} = 900$ GeV the first viable models are found around 300 GeV.

A generalized version of figure 3.8 is shown in figure 3.9 where all of the 10^5 models are displayed in the plane $(M_\chi, \sigma_{\mathrm{SI}})$ and different symbols are used to mark the position of the models with respect to the resonance. Contrary to figure 3.8, M_{H_2} is no longer fixed but allowed to vary over the entire range given in table 3.1. The former stated connection between the cross section σ_{SI} and the position of the model according to the resonance made clear that there is no large suppression for models below the resonance (blue squares). Hence all of these models are concentrated in the upper left corner, the cross section hardly goes below 10^{-12} pb and the parameter range restricts M_χ to be smaller than or equal to 450 GeV. Still some models feature cross sections small enough to avoid the current bound (solid line), but a large part will be probed by the future experiment XENON1T (dashed line). For models on the resonance (red crosses), the cross section is rather suppressed as shown in the previous figures 3.8 and 3.2. Con-

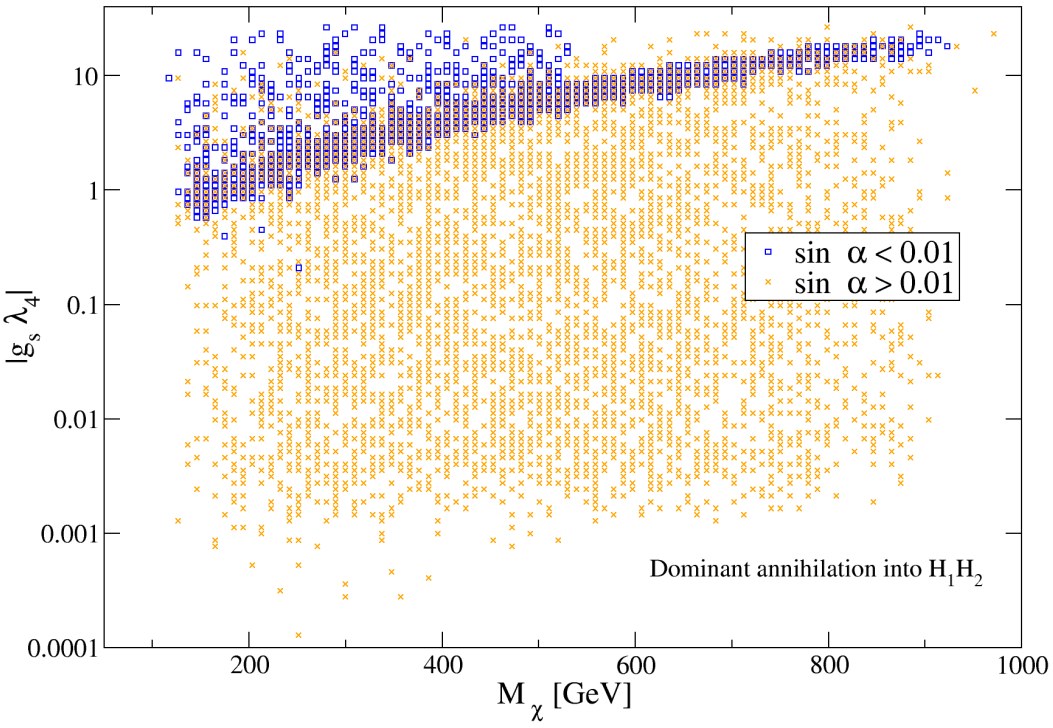

Figure 3.7.: Models featuring H_1H_2 as a dominant final state displayed in the plane $(M_\chi, g_s\lambda_4)$ with different symbols to distinguish between models with $\sin\alpha$ smaller or lager than 0.01.

sequently, most of them are not detectable yet, but future experiments will be able to exclude a huge portion of resonant models for the first time. Concerning models above the resonance (orange circles), the manifestation of two new final states featuring H_2 provides a contribution to the relic density which is independent of $\sin\alpha$. This weakens the direct detection bound and enables values of σ_{SI} all over the plane for any given mass M_χ. Despite this huge variety, lots of the models above the resonance will be probed in the future.

It is useful to investigate the regions below and above the resonance separately, as properties change drastically below or above the resonance. For example, the relic density receives a contribution independent of $\sin\alpha$ above the resonance, while the cross section is determined by $g_s \sin\alpha$ for all models. So, figures 3.10 and 3.11 display models either below or above the resonance projected onto the plane $(M_\chi, |g_s \sin\alpha|)$. In both figures blue squares mark all models currently excluded by XENON100, red crosses denote models not yet probed but within reach of XENON1T, whereas models depicted

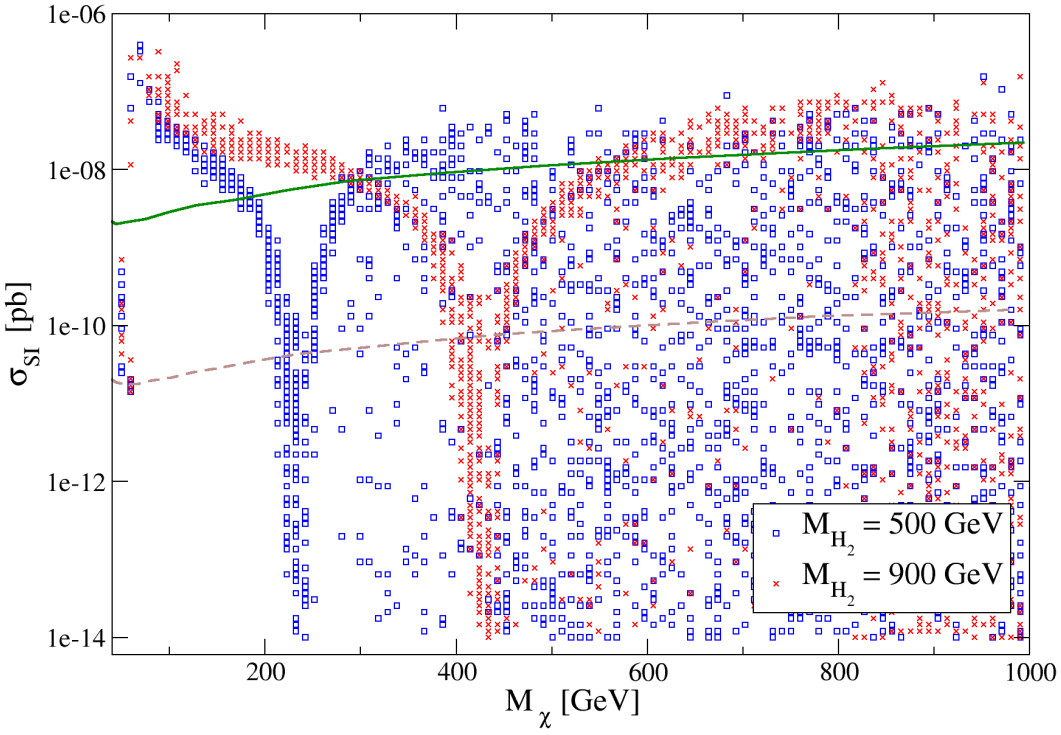

Figure 3.8.: The spin-independent direct detection cross section with respect to the dark matter mass is shown. Blue squares denote $M_{H_2} = 500$ GeV and red crosses stand for $M_{H_2} = 900$ GeV. The green solid line displays the current bound from the XENON100 experiment, whereas the dashed line shows the expected sensitivity of XENON1T.

by green circles are able to evade future detection. All models below the resonance are presented in figure 3.10. The three colored bands, indicating the direct detection status, are clearly separated, there is only little overlap, as both the direct detection cross section and the relic density are determined by g_s and $\sin\alpha$. Models which are already excluded by XENON100 feature the largest values of $|g_s \sin\alpha|$ down to about 0.1, while models within the reach of XENON1T have $|g_s \sin\alpha| \geq 0.01$. Only few models with smallest values of $|g_s \sin\alpha|$ will not be probed in the future.

Once the resonance is crossed, the correlation between relic density and direct detection is lost, new contributions independent of $\sin\alpha$ to the annihilation cross section appear. There is no longer a clear separation between the three detection status regions between all models above the resonance as displayed in figure 3.11. Instead there is a sizable overlap and a slight shift in $|g_s \sin\alpha|$ depending on the dark matter mass M_χ. Excluded models feature $|g_s \sin\alpha| \gtrsim 0.1$ for M_χ around 100 GeV and $|g_s \sin\alpha| \gtrsim 0.2$

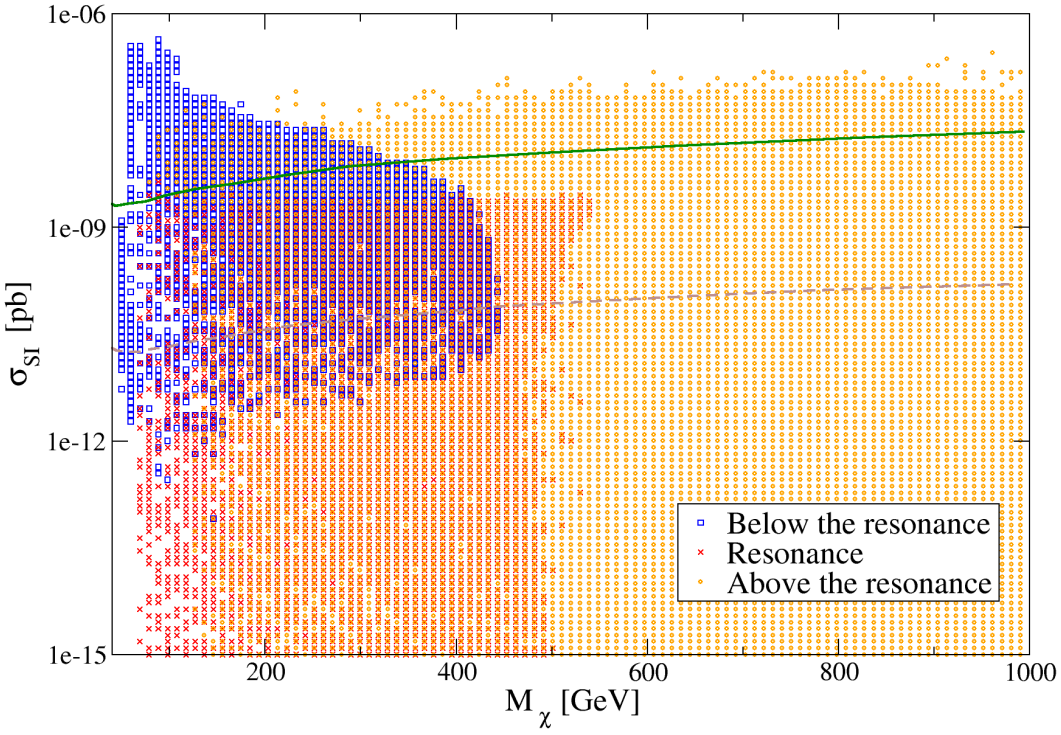

Figure 3.9.: All 10^5 models shown in the plane $(M_\chi, \sigma_{\mathrm{SI}})$. Different symbols mark the position with respect to the resonance, blue squares are models below the resonance, red crosses are models on the resonance and orange crosses are models above the resonance. The green solid line is the current bound from XENON100 and the dashed line indicates the expected sensitivity from XENON1T.

for M_χ at 1 TeV. XENON1T can probe models with $|g_s \sin\alpha|$ on order of magnitude below this. Yet, a large amount of models, featuring the smallest values of $|g_s \sin\alpha|$, has direct detection cross sections below the expected sensitivity.

To summarize all preceding outcomes for direct detection, figure 3.12 depicts the regions in the plane (M_χ, M_{H_2}) which are compatible with the relic density constraint, similar to figure 3.3, including direct detection limits from XENON100.

The red shaded area displays the resonance region, models to the left are below the resonance and models to the right are above the resonance. The different symbols are used to distinguish dominant annihilation final states. A triangular region in the upper left corner is completely excluded by the current limits, it features for instance $M_{H_2} \lesssim 500$ GeV for models with $M_\chi = 200$ GeV and $M_{H_2} \lesssim 900$ GeV for $M_\chi = 300$

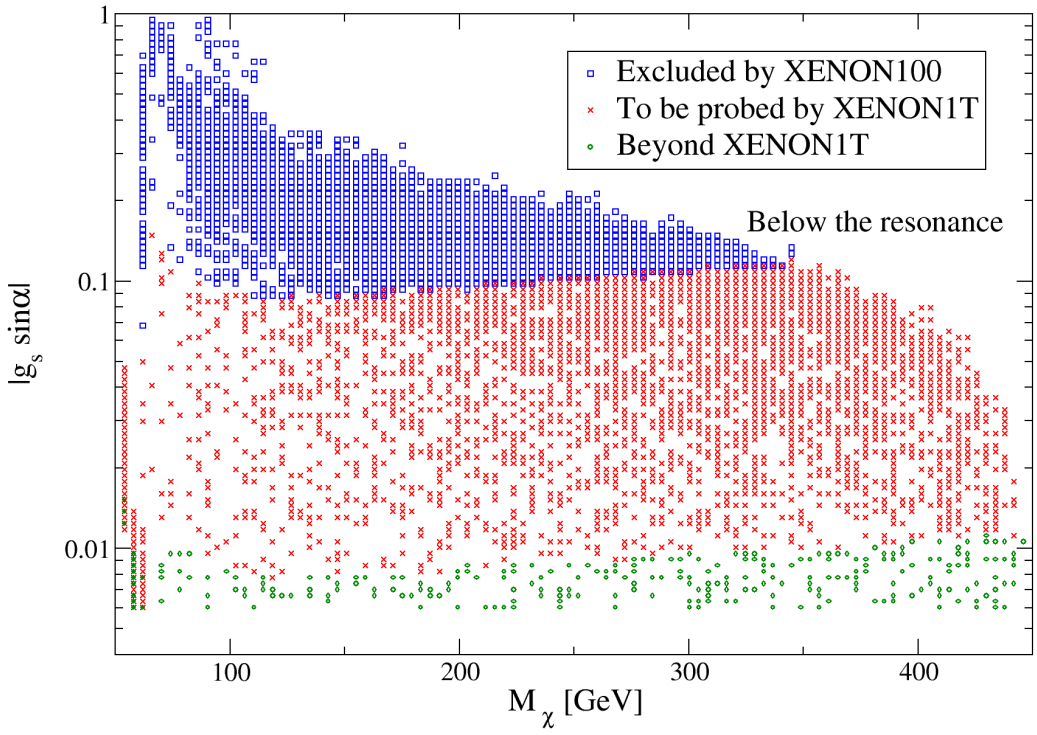

Figure 3.10.: The correlation between M_χ and $|g_s \sin\alpha|$ with respect to direct detection feasibility for models below the resonance is shown. Different symbols mark regions within or beyond recent and future sensitivities.

GeV. Interestingly, viable models can be found even below the resonance. Starting at M_χ about 350 GeV and higher, the non-excluded models can be found for any value of M_{H_2}. Still a lot of models with featuring W^+W^- (blue squares) as the dominant annihilation channel are ruled out for larger masses, while only few models with H_1H_2 (orange crosses) and H_2H_2 (green circles) in the final state are excluded. Most of them are unaffected, as processes featuring H_2 receive contributions which are not suppressed by the mixing angle α.

3.1.2. Indirect Detection

Since the parity conserving case ($g_p = 0$) was considered, the dark matter annihilation rate is proportional to the square of the dark matter velocity v. In the early Universe around the freeze out v^2 is approximately $1/20$, so the suppression is not that strong. Nowadays, in the galactic halo v^2 is nearly 10^{-6} leading to a large suppression of the annihilation cross section – see [4].

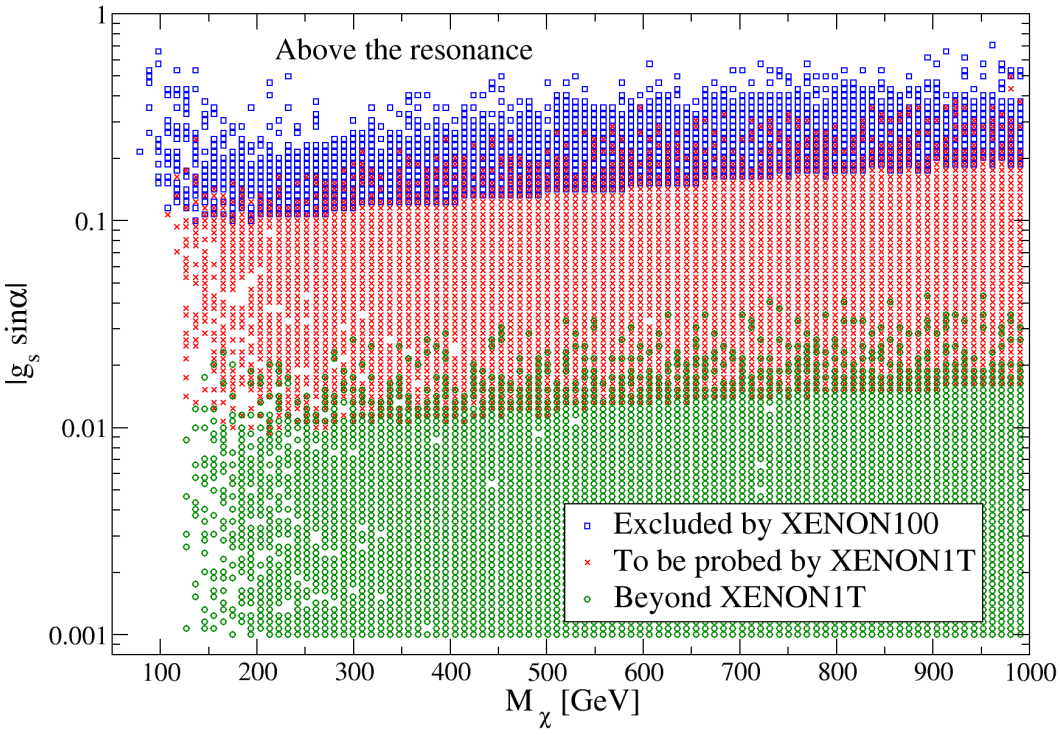

Figure 3.11.: Models above the resonance in the plane $(M_\chi, |g_s \sin\alpha|)$ classified by their direct detection likeliness.

Figure 3.13 shows the dark matter annihilation rate nowadays σv versus the dark matter mass M_χ while differentiating between the four main annihilation final states identified in the previous paragraph. Since $v \propto 10^{-6}$, for WIMPs σv is naively expected to be around 10^{-31} cm^{3}s^{-1}, which is only true for some models here, instead σv varies over a range of about 10 orders of magnitude. Values up to 10^{-28}cm^{3}s^{-1} are reached for models at lower masses, while much smaller values, down to 10^{-38}cm^{3}s^{-1}, can be found for arbitrary masses M_χ. In figure 3.14 all models with unexpected σv, either larger than 10^{-30} cm^{3}s^{-1} or smaller than 10^{-33} cm^{3}s^{-1}, are shown in order to explain these deviations.

The dashed lines are the resonance and the thresholds involving H_2: the red line is for $M_{H_2} = 2M_\chi$, the purple line features $M_{H_2} = 2M_\chi - M_{H_1}$ and the yellow line is $M_{H_2} = M_\chi$. All points on the right border of the figure are at the H_1 resonance where $M_{H_1} = 2M_\chi$. This includes a lot of the models with annihilation rates higher than 10^{-30} cm^{3}s^{-1} (black stars). All other models of this type lie at the H_2 resonance (red), where $M_{H_2} = 2M_\chi$. This is as expected, at both resonances the dark matter can annihilate very efficiently, enhancing the cross section. Models with σv smaller than 10^{-33} cm^{3}s^{-1}

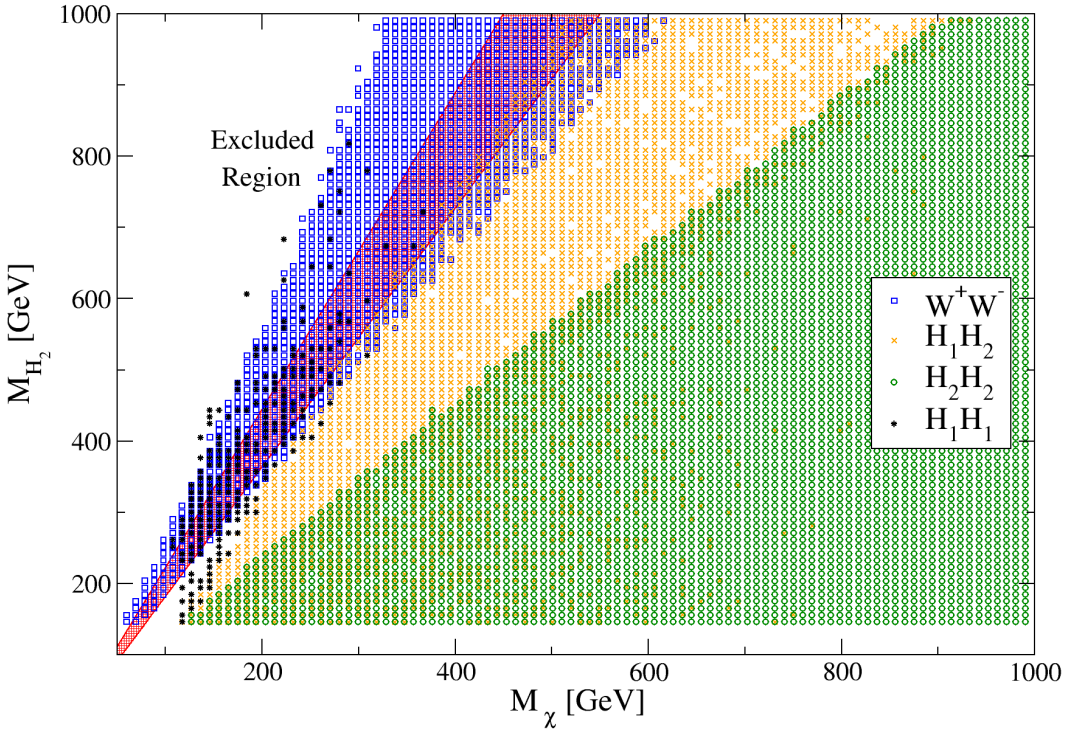

Figure 3.12.: The region of the plane (M_χ, M_{H_2}) which is compatible with the relic density constraint and direct detection bounds from XENON 100 is shown. The red shaded area displays the resonance and different symbols are used to distinguish between the dominant final states.

(blue squares) lie either close to the resonances or the thresholds for H_1H_2 (purple) and H_2H_2 (yellow) production. Their cross section is so suppressed, since in the early Universe dark matter particles were energetic enough to pass the thresholds and also hit the resonances, whereas nowadays these annihilation channels are kinematically closed.

This renders indirect detection rather unfeasible, as indirect detection with gamma rays has just started to probe values around $\sigma v \approx 3{\times}10^{-26}\mathrm{cm}^3/\mathrm{s}$ for very light dark matter [57],[61]. The expected gamma ray flux is proportional to σv, which can be largely suppressed in this model, the same is true for antimatter annihilation signals [62]. Thus the only chance for indirect detection in this framework is a high energetic neutrino signal from dark matter annihilation in the Sun [63].
As the Sun moves through the galactic halo, it accumulates dark matter particles. The

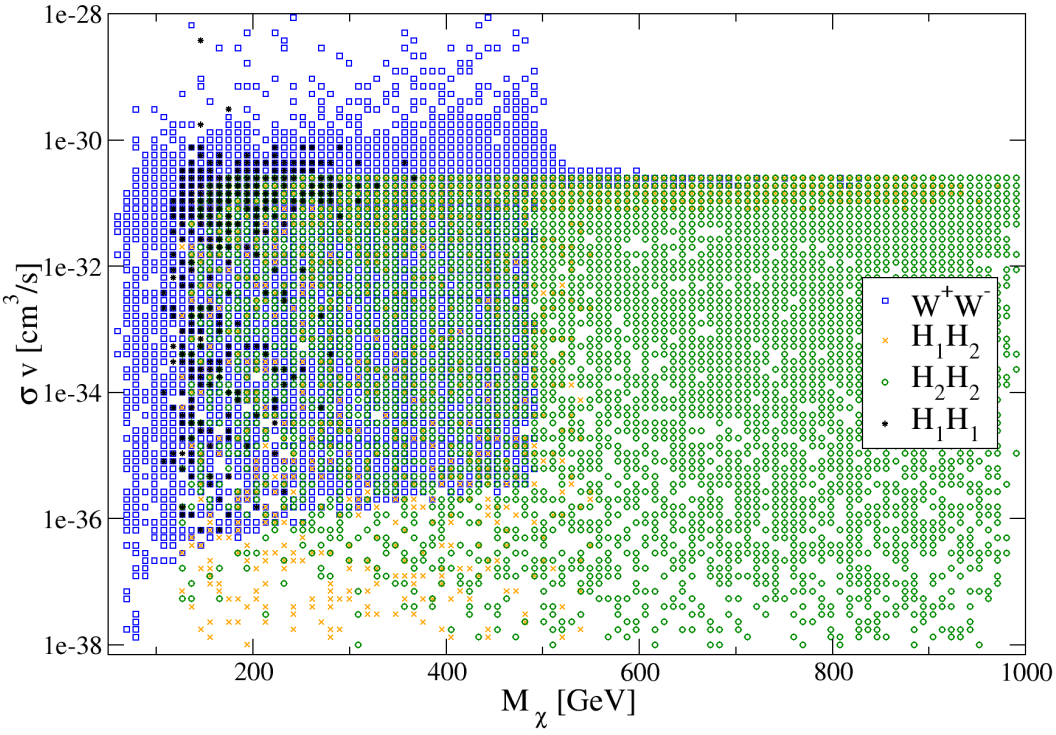

Figure 3.13.: The dark matter annihilation rate today σv is shown relative to the dark matter mass M_χ. Different symbols distinguish between dominant annihilation channels.

evolution of the number of captured particles N is described by

$$\frac{\mathrm{d}N}{\mathrm{d}t} = CN - AN^2 - EN \tag{3.10}$$

where C is the capture rate, A describes annihilation and E takes into account the evaporation. The capture rate C depends mostly on the nuclear recoil cross section, whereas the annihilation rate A is proportional to the annihilation cross section. Evaporation is the process of a particle acquiring enough kinetic energy in elastic recoils within the massive object to overcome the gravitational potential, but this effect is neglected since it requires rather large recoil cross sections. Thus the solution for the number of captured particles with negligible evaporation is

$$N(t) = \sqrt{\frac{C}{A}} \tanh \sqrt{CA}t. \tag{3.11}$$

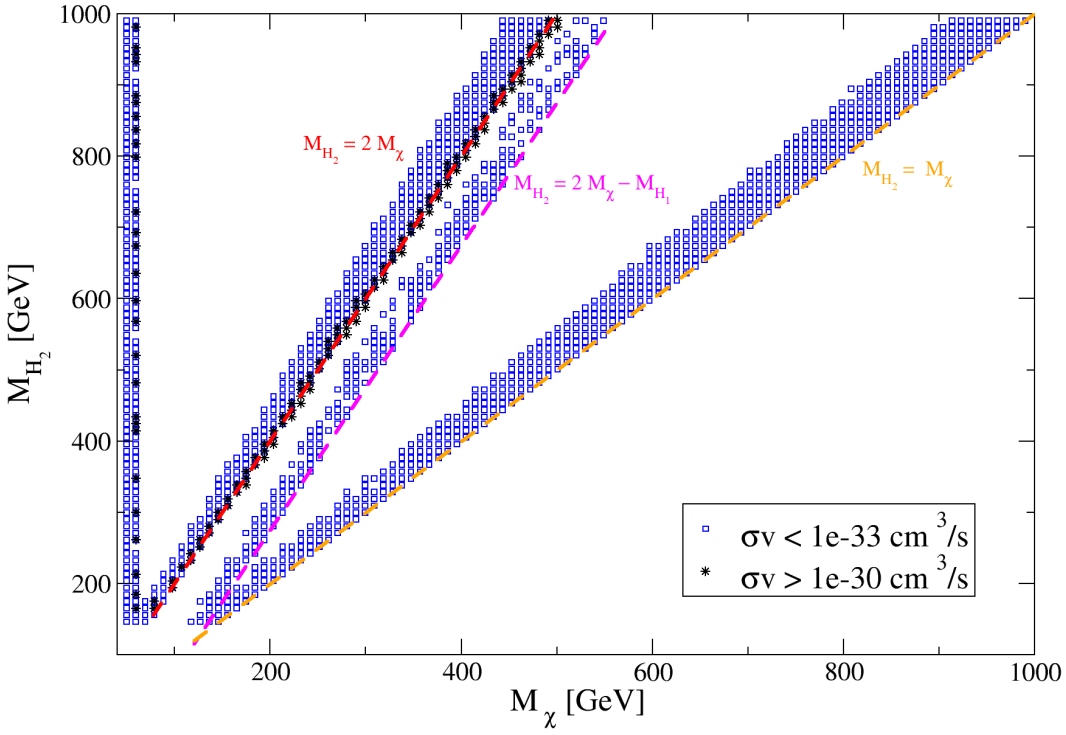

Figure 3.14.: Models with unusually large σv are depicted by black stars, models with rather small σv are shown by blue squares for M_χ versus M_{H_2}. The dashed lines are the resonance and the thresholds: red is $M_{H_2} = 2M_\chi$, purple equals $M_{H_2} = 2M_\chi - M_{H_1}$ and yellow is $M_{H_2} = M_\chi$.

If the lifetime of the Sun $t_\odot \approx 4.6{\times}10^9$ years is taken for t, equilibrium is reached for

$$\sqrt{CAt_\odot} \gg 1. \tag{3.12}$$

With this requirement N is constant and the current annihilation rate of dark matter in the Sun is

$$\Gamma_{\text{ann}} = \frac{1}{2}AN^2 = \frac{1}{2}C\tanh^2\sqrt{CAt} \approx \frac{1}{2}C. \tag{3.13}$$

For a feasible neutrino signal from dark matter annihilation in the Sun it is crucial to determine if equilibrium is reached. If that is the case, the suppression of σv becomes irrelevant, as the annihilation rate in the Sun then only depends on the capture rate and

thus on the direct detection cross section. Yet the accessibility of equilibrium depends on σv.

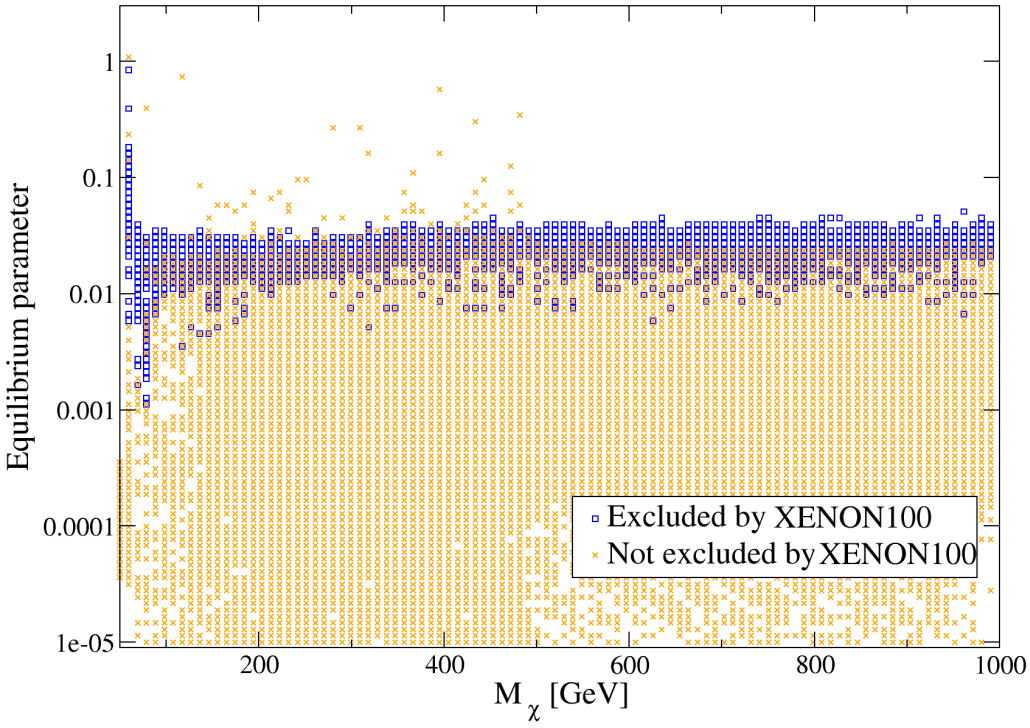

Figure 3.15.: The equilibrium parameter is plotted versus dark matter mass. Blue squares depict models excluded by XENON100, orange crosses are not yet excluded models.

Whether neutrinos are produced in dark matter annihilation or not, depends on the final states. If the main annihilation channel features H_1 or H_2, it is not very likely to yield a large amount of neutrinos. The W^+W^- final state in contrast, which is dominant mostly at lower dark matter masses, produces neutrinos in subsequent decays. For all models, which feature the W^+W^- final state, the equilibrium parameter as a function of M_χ is shown in figure 3.15. Models which are already excluded by XENON100 (blue squares) mostly have an equilibrium parameter larger than 0.01. Models which are beyond the reach of XENON100 (orange crosses) hardly have equilibrium parameters larger than 0.1. Neither for excluded nor for non-excluded models is the equilibrium parameter much larger than one. Hence equilibrium is never reached and the neutrino flux is small as shown in figure 3.16.

Models, which are excluded by XENON100 (blue squares), feature largest fluxes up

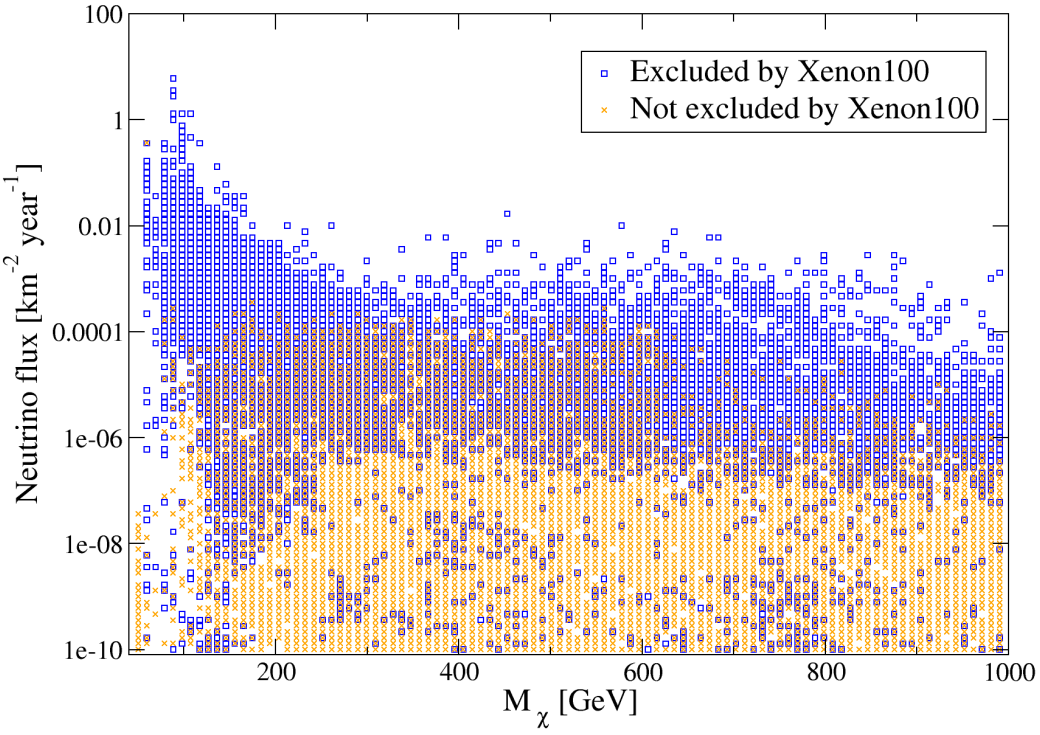

Figure 3.16.: The expected neutrino flux at the Earth versus dark matter mass is shown. Blue squares are models which are already excluded by XENON100, orange crosses are not yet probed.

to 10 neutrinos per km^2 and year for small masses. All non-excluded models (orange crosses) lie orders of magnitudes below this; at most at 10^{-4} neutrinos per km^2 and year. Overall the neutrino flux on Earth is small, since equilibrium is never reached in the Sun due to the σv suppression, especially at thresholds and resonances. Thus there is no enhanced neutrino signal from the Sun.
Regarding indirect detection in general, signals are way beyond detection feasibility. This renders indirect detection hopeless in the parity conserving case. In the more general case with $g_p \neq 0$ this result changes drastically.

3.2. General Case $g_p \neq 0$

The general case is achieved by allowing the parameter g_p to be non-zero to enable parity violating interactions as well. In this framework the dark matter annihilation rate in the early Universe receives a new contribution which proportional to g_p^2 and not velocity suppressed. In consequence indirect detection becomes more feasible. However,

the direct detection cross section is not altered, equation (3.7) is still valid, as all g_p contributions to it are suppressed by the square of the dark matter velocity. Thus it is easier to achieve the correct relic density while evading direct detection.
For the following analysis a new scan was made where in addition g_p was allowed to vary freely in the same range as g_s. All of the new 10^5 models fulfill the relic density constraint.

3.2.1. Viable Parameter Space and Direct Detection

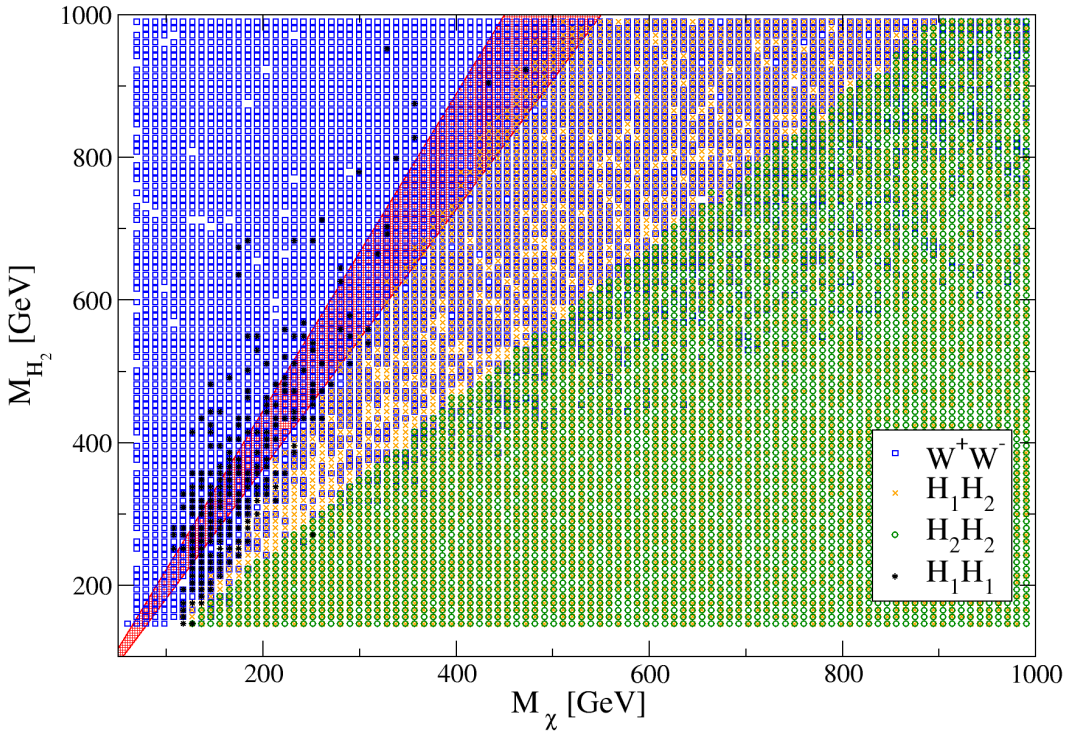

Figure 3.17.: The region of the parameter space (M_χ, M_{H_2}) which is compatible with both relic density and direct detection constraints is shown. Different symbols are used to distinguish between dominant annihilation channels and the red hatched area depicts the resonance.

In order to identify the viable parameter space, the models are confronted with the limits from XENON100. All consistent models are projected onto the plane (M_χ, M_{H_2}) in figure 3.17. The red shaded area is the resonance and the different symbols are used to distinguish between the dominant annihilation final states. Most of the models below the resonance feature W^+W^- (blue squares) as the dominant annihilation channel and

also on the resonance and above the resonance this final state is more common than in the parity conversing case. Models, where the dark matter mainly annihilates to H_1H_2 (orange crosses), now spread over the whole region above the resonance extending into the high mass region and hugely overlap with models with the final state H_2H_2 (green circles). The entire plane is filled with parameter points, in contrast to the parity conserving case, there is no region entirely excluded.

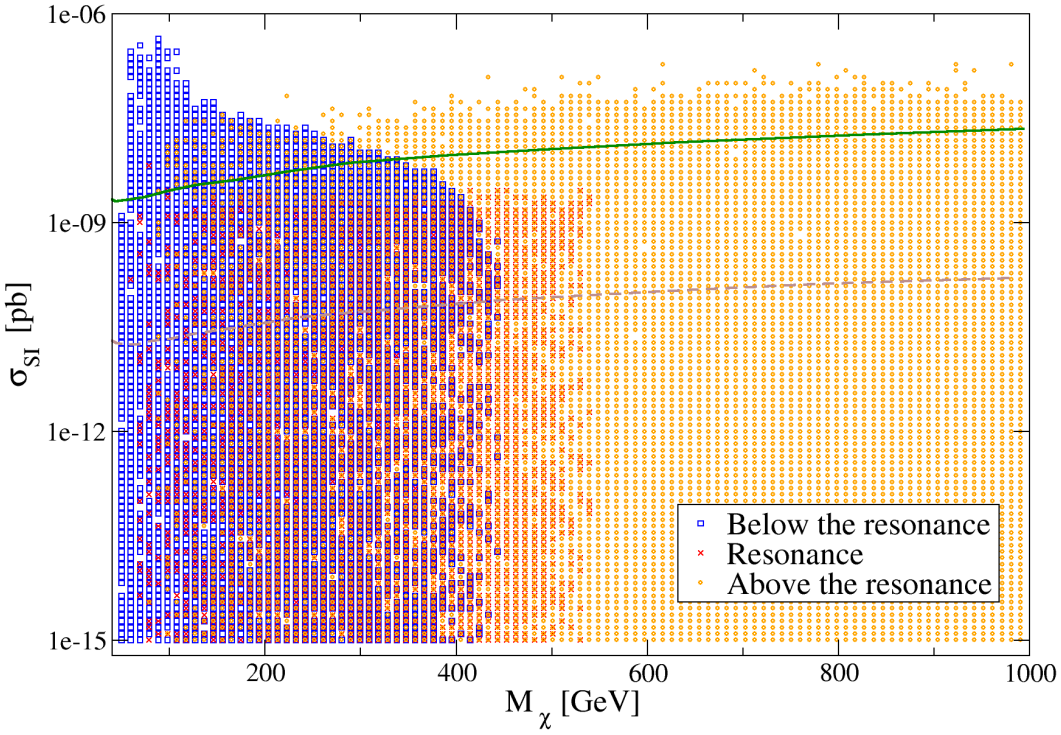

Figure 3.18.: The viable models are projected onto the plane $(M_\chi, \sigma_{\mathrm{SI}})$. Different symbols indicate whether a model is below (blue squares), above (orange circles) or on (red crosses) the resonance. The solid line displays the XENON100 limit and the dashed line is the expected sensitivity for XENON1T.

To illustrate this attenuation of direct detection limits further, figure 3.18 displays a scatter plot of the spin independent elastic scattering cross section σ_{SI} versus dark matter mass M_χ. The green solid line shows the current bound from XENON100 and the dashed line displays the expected cross section for XENON1T. Different symbols are used to indicate the position of the model with respect to the resonance, blue squares depict models lying below, orange circles models above and red crosses models on the

resonance. For all three types of models it is possible to obtain small values of σ_{SI} orders of magnitude below the reach of XENON1T. Especially models below the resonance are not concentrated in the upper left any more but extend down to $\sigma_{\mathrm{SI}} \approx 10^{-15}$ pb. Hence it is neither possible to rule out an entire region in the parameter space now nor in the future. Nevertheless future experiments such a XENON1T will be able to exclude a huge number of models, even though it cannot probe the entire range of models below the resonance.

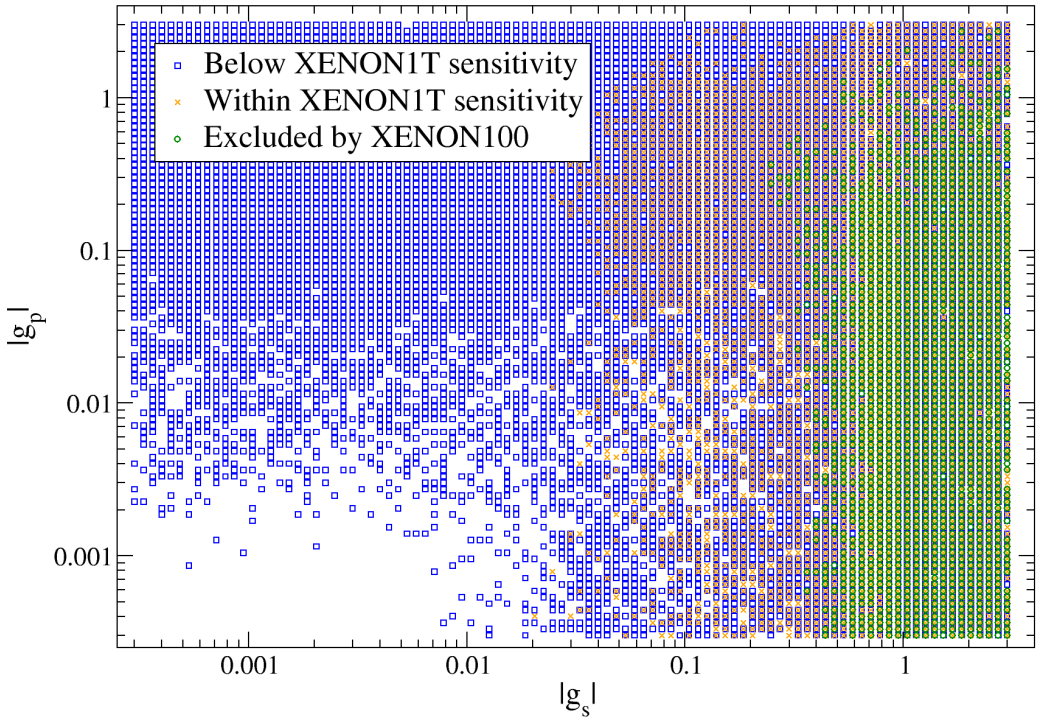

Figure 3.19.: The models consistent with the relic density constraint are presented in the plane $(|g_s|, |g_p|)$. Different symbols display the reach of XENON100 and XENON1T.

In order to characterize the new viable regions further, figure 3.19 shows a scatter plot of the parameter $|g_s|$ versus $|g_p|$. The symbols are used to mark the detection status regarding XENON100. If g_s and g_p are simultaneously small, it is not possible to satisfy the relic density constraint, therefore no points are found in this region. So, models with small values of g_s have $g_p \gtrsim 10^{-3}$ and models with small g_p feature $g_s \gtrsim 10^{-2}$. Regarding direct detection, g_s is the important parameter, as the direct detection cross section does not depend on g_p. Hence models which are already excluded by XENON100 (green

circles) can have nearly any value for g_p but g_s is larger than about 0.4. As the direct detection limits are softened in the presence of g_p, models which are beyond the sensitivity of 1ton-experiments (blue squares) can be found all over the plane. This implies, that it is possible to find models which evade future detection for all values of g_p and no region of g_p nor g_s will be completely ruled out by direct detection experiments. Still it is useful to analyze the models, which are consistent with the limits from XENON100.

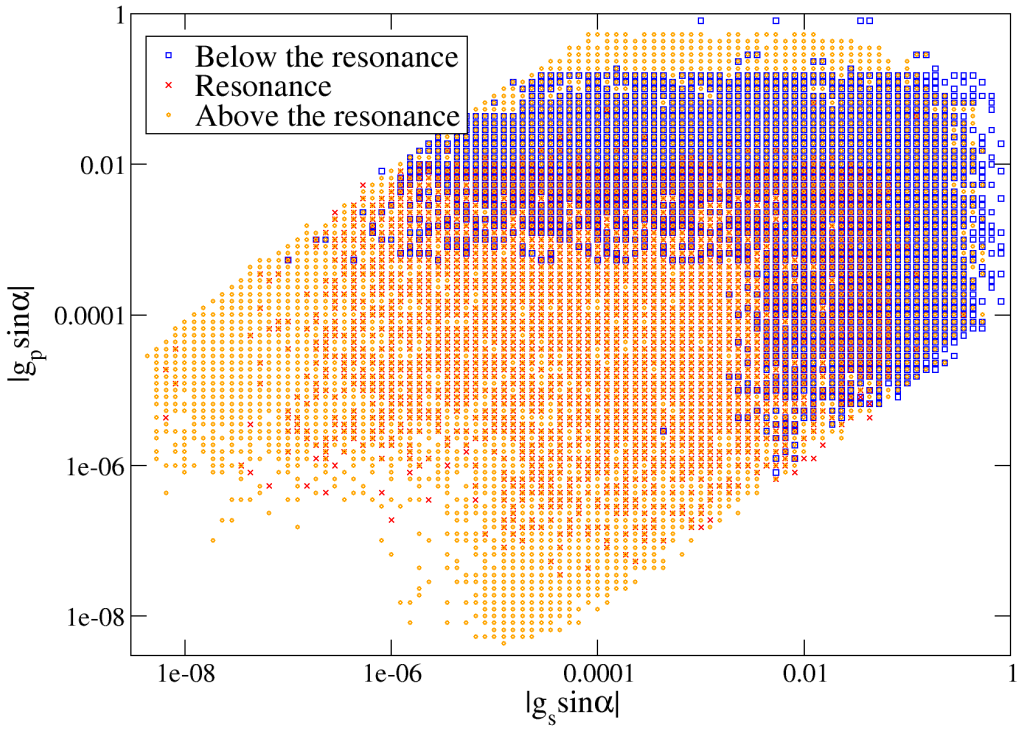

Figure 3.20.: A scatter plot of $|g_s \sin\alpha|$ versus $|g_p \sin\alpha|$ including the model's position with respect to the resonance. Blue squares are below, red crosses on and orange crosses above the resonance.

Figure 3.20 shows the distribution of $|g_s \sin\alpha|$ versus $|g_p \sin\alpha|$ for all these non-excluded models. In the parity conserving case the resonance plays a crucial role, the same is true in the general case as illustrated by figure 3.20. The symbols indicate the model's position with respect to the resonance. Models below the resonance (blue squares) are concentrated in the upper right corner along a narrow band, as $|g_s \sin\alpha|$ and $|g_p \sin\alpha|$ cannot be small for these at the same time due to the dark matter constraint. If $|g_s \sin\alpha|$ is small, $|g_p \sin\alpha|$ is larger than 0.001 and for small $|g_p \sin\alpha|$ the value of $|g_s \sin\alpha|$ is mostly above 0.01. Once the resonance is crossed (orange circles),

the relic density is no longer determined by $\sin\alpha$, therefore parameter points can be found in a broad region. For models on the resonance (red crosses) however, $|g_s \sin\alpha|$ and $|g_p \sin\alpha|$ cannot be very large, at most $|g_p \sin\alpha|$ is around 0.01 and $|g_s \sin\alpha|$ at approximately 0.04.

3.2.2. Indirect Detection

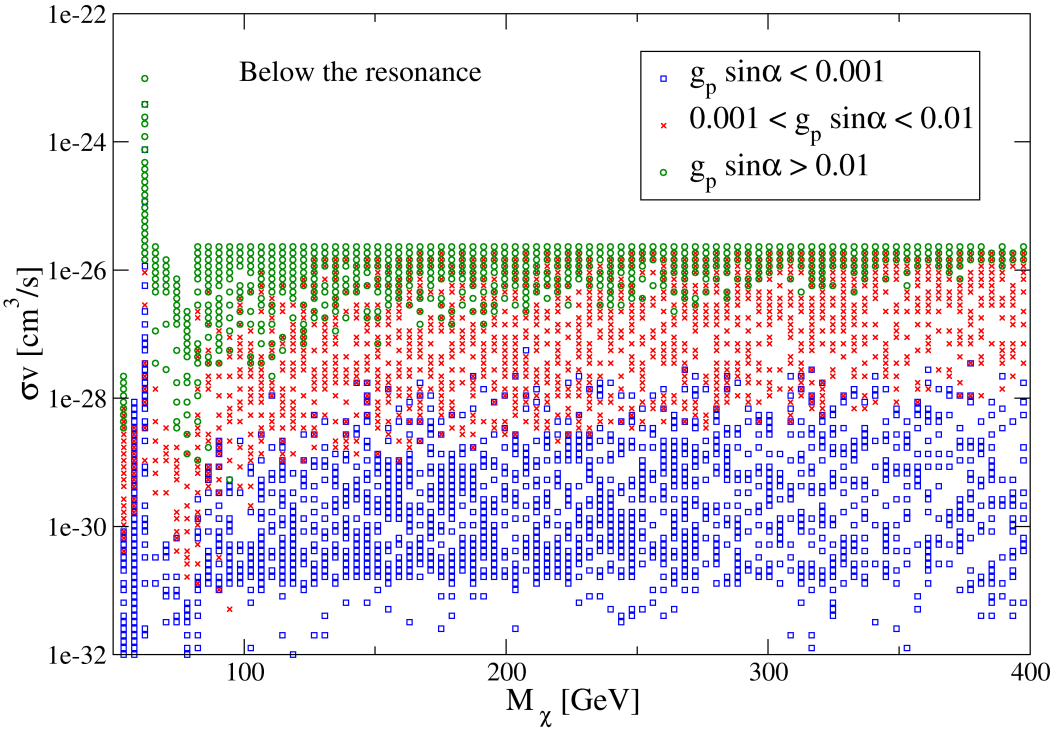

Figure 3.21.: The distribution of σv versus dark matter mass M_χ is presented for models below the resonance. The colors are used to separate three regions of $g_p \sin\alpha$: blue squares $g_p \sin\alpha \langle 0.001$, red crosses $0.001 \langle g_p \sin\alpha \langle 0.01$ and green circles $g_p \rangle 0.01$

In the general case ($g_p \neq 0$) indirect detection prospects look more promising, due to the new contribution to σv proportional to g_p^2 and independent of the dark matter velocity.
Figure 3.21 and figure 3.22 show scatter plots of the dark matter annihilation rate σv versus the dark matter mass M_χ for models below respectively above the resonance. Since $g_p \sin\alpha$ is an important parameter for σv below the resonance, symbols are used in figure 3.22 to differentiate between three ranges: blue squares for $g_p \sin\alpha$ smaller than

0.001, red crosses for $g_p \sin\alpha$ between 0.001 and 0.01 and green circles for $g_p \sin\alpha$ above 0.01. For these models below the resonance largest annihilation rates are obtained for smallest dark matter masses and the three regions of $g_p \sin\alpha$ overlap slightly. A strong correlation between $g_p \sin\alpha$ and σv is visible, the higher $g_p \sin\alpha$ the higher the annihilation rate σv and the thermal value of around 3×10^{-26} cm^3/s is reached for models with large $g_p \sin\alpha$.

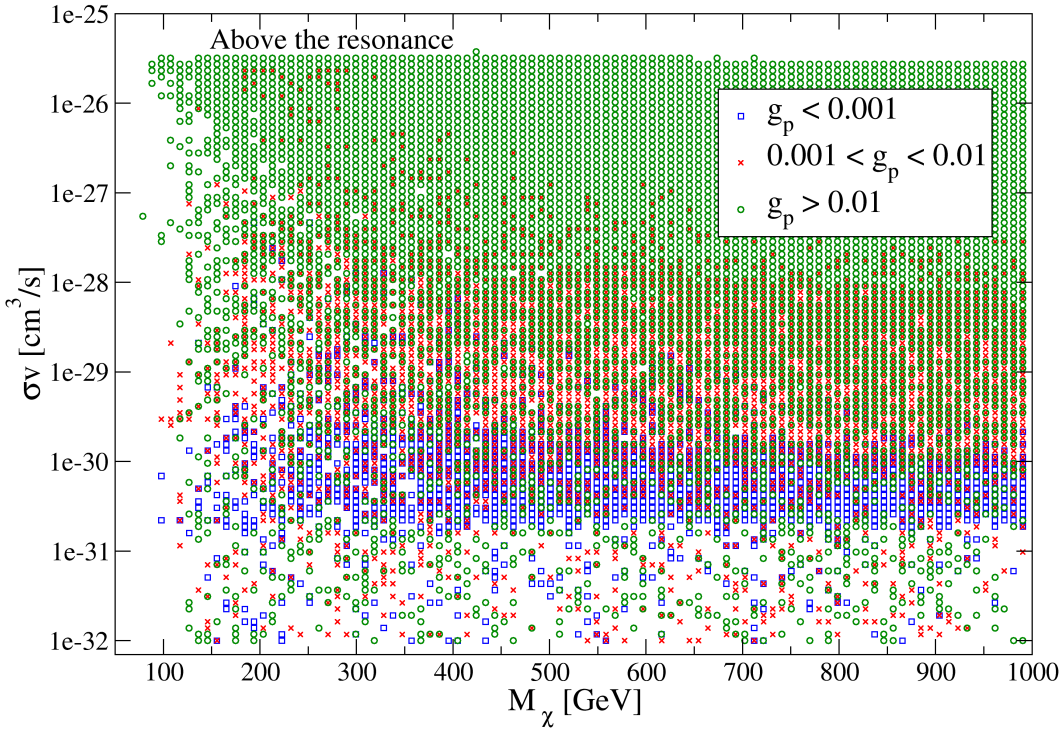

Figure 3.22.: Models above the resonance are displayed in the plane $(M_\chi, \sigma v)$. Different colors indicate the value of $g_p \sin\alpha$.

Above the resonance, see figure 3.22, g_p rather than $g_p \sin\alpha$ becomes the important parameter, as the dependence on $\sin\alpha$ is softened. Therefore three regions of g_p are distinguished by different symbols: blue squares feature g_p smaller than 0.001, red crosses have g_p between 0.001 and 0.01 and green circles have values larger than 0.01. In general the largest annihilation rates σv are obtained for models with largest values for g_p, but also models with small σv can feature g_p larger than 0.01. Still there is a visible separation between the three ranges for g_P as the upper limit of σv gets smaller with smaller g_P.

In the general case much larger values for σv are obtained compared to the parity conserving case with $g_p = 0$, both below and above the resonance. A lot of models fea-

ture σv close to the thermal value, therefore indirect detection becomes more promising. As FERMI-Lat [57, 61] has just started to probe thermal cross sections for very light dark matter particles, antimatter and gamma ray searches are not expected to give any substantial constraints. On account of this, only neutrino signals from dark matter annihilation in the Sun are considered. Fortunately, models featuring final states producing neutrinos are much more common in all mass ranges. And as σv is larger, it is easier to reach equilibrium between dark matter capture and annihilation. The equilibrium parameter as a function of dark matter mass M_χ is shown in figure 3.23, the colors indicate the models' detection status.

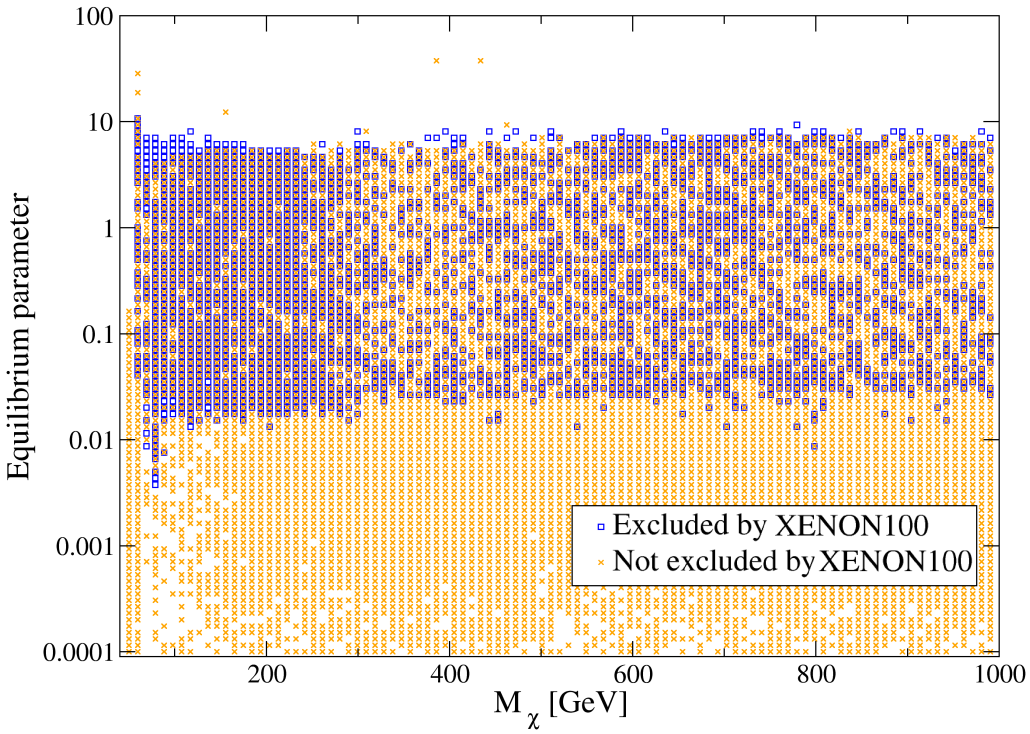

Figure 3.23.: A scatter plot of the equilibrium parameter versus the dark matter mass with different symbols to display the detection status of the models. Blue squares are models which are within the reach of XENON100 and orange crosses are not yet probable models.

Lots of models over the whole mass range feature equilibrium parameters larger than one, so equilibrium is reached and the annihilation process is solely determined by the capture rate.

Equilibrium is reached for models which are already excluded by XENON100 (blue squares) as well as for models which lie below the current sensitivity (orange crosses).

Most of the excluded models feature equilibrium parameters larger than 0.01. Non-excluded models can have large or small values but tend to reach at max slightly smaller equilibrium parameters than the excluded models.
In order to determine indirect detection capabilities, the expected neutrino flux on the Earth against the dark matter mass M_χ is shown in figure 3.24. Again, symbols indicate the direct detection feasibility.

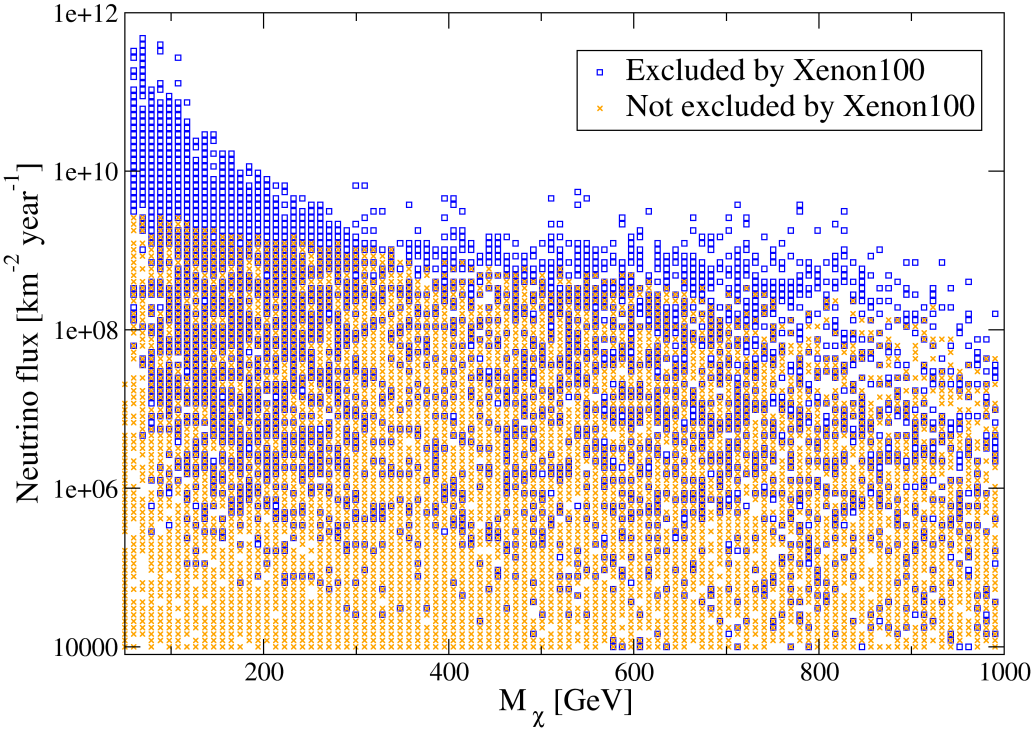

Figure 3.24.: The expected neutrino flux at the Earth versus dark matter mass is shown. Models are marked if they are already excluded by XENON100.

Since equilibrium is reached for a lot of models, high fluxes can be obtained, reaching up to 10^{12} neutrinos per km^2 and year for dark matter particles lighter than 300 GeV. Unfortunately all models with lager fluxes are already excluded by XENON100 (blue squares). Models which are not yet excluded (orange crosses) yield fluxes at least three orders of magnitude smaller.

Neutrino telescopes, like IceCube, do not detect the neutrinos directly but muons coming from interactions of neutrinos with the surrounding material. Hence, in order to contrast these findings with recent bounds, the expected muon flux with respect to the dark matter mass is shown in figure 3.25. The solid line is the current limit from

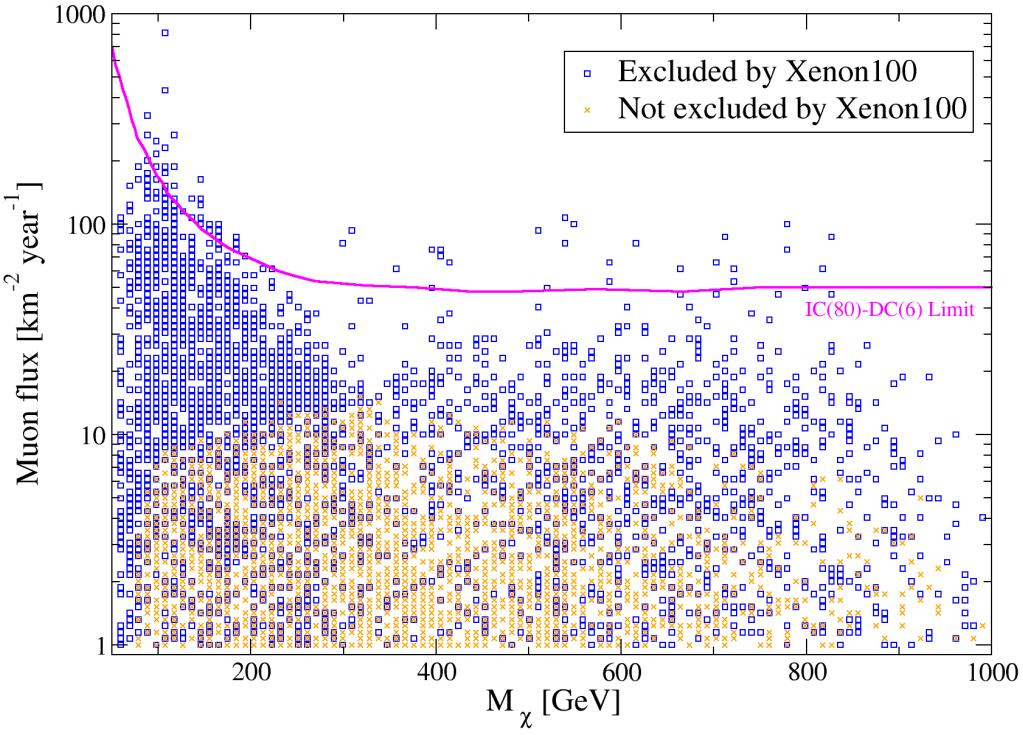

Figure 3.25.: The muon flux with respect to dark matter mass M_χ is shown. The solid line is the current IceCubeDeepCore detection limit.

IceCubeDeepCore [64, 65] and the same symbols as before are used regarding direct detection. The highest fluxes are found for smallest values of M_χ, they can reach up to nearly 1000 per km^2 and year, but similarly high fluxes can even be found for dark matter masses up to 800 GeV. There is no strict limitation to the low mass region. Yet, only few models are ruled out by the IceCube limits. Unfortunately, all of these are also excluded by XENON100 as indicated by the blue squares. Models which are not within the sensitivity of XENON100 (orange crosses) feature muon fluxes at least a factor of three below the current IceCubeDeepCore limit.

3.3. Summary

As it was shown, the singlet fermionic model provides a simple and interesting way of explaining the dark matter. In it the Standard Model is extended by two new particles, one Majorana fermion χ acting as dark matter and a real scalar ϕ, which mixes with the Higgs. Within this framework the dark matter particle can couple to the new scalar

via parity conserving and parity violating interactions.

To analyze this model, an extensive scan of the parameter space compatible with the dark matter constraint is used. By projecting these parameter points onto different planes the feasible parameter space is identified and characterized and then confronted with current and future direct detection limits. For the parity conserving case a new indirect Higgs portal is found to satisfy the dark matter constraint, it is shown that direct detection allows to exclude a large part of the parameter region and that indirect detection is always hopeless. In the general case the link between relic density and direct detection is weakened. Still, it is possible to probe a large amount of the parameter space with direct detection experiments. Indirect detection is more feasible for the general case, as the annihilation cross section is large enough to achieve equilibrium for dark matter annihilation in the Sun. Although this results in significantly larger neutrino fluxes on Earth, it is shown that all high flux models are already excluded by direct detection.

4. Two Component Dark Matter

The two-component dark matter model can be seen as a union of the singlet scalar dark matter [66, 67, 68, 69, 70, 6, 47, 48] and singlet fermionic dark matter[10, 18, 19, 21, 22, 1]. In addition to the Majorana fermion χ and the real scalar mediator ϕ another real scalar field S is introduced. All three new fields are singlets under the gauge group. Again the $\mathbb{Z}_2$ symmetry is imposed to render the lightest dark matter species stable, hence S and χ are odd whereas all Standard Model particles and ϕ are even. The heavier of the two dark matter species is stable due to an accidental symmetry, as it is not possible to write terms involving both S and χ that are still invariant under the gauge and $\mathbb{Z}_2$ symmetry. Thus there are two stable dark matte particles in this model.

In this extension the interactions between χ and the Standard Model are not altered, the Lagrangian for χ still is the same as in equation (3.1):

$$L = -\frac{1}{2}\left(M_\chi \overline{\chi}\chi + g_s \phi \overline{\chi}\chi + g_p \phi \overline{\chi}\gamma_5 \chi\right).$$

And as in the singlet fermionic model, the electroweak symmetry breaking gives rise to a mixing between H and ϕ with the mass eigenstates H_1 and H_2. S does not mix with H and ϕ due to the $\mathbb{Z}_2$ symmetry, and it does not acquire any vacuum expectation value, so the potential is

$$\begin{aligned} -V(\phi, H, S) = \; & \mu_h^2 \left(H^\dagger H\right) + \lambda_H \left(H^\dagger H\right)^2 - \frac{\mu_\phi^2}{2}\phi^2 + \frac{\lambda_\phi}{4}\phi^4 + \mu_1^3 \phi + \frac{\mu_3}{3}\phi^3 + \frac{\lambda_4}{2}\phi^2 \left(H^\dagger H\right) \\ & + \mu\phi \left(H^\dagger H\right) + \frac{\lambda_S}{4}S^4 + \frac{\lambda_{HSS}}{4}\left(H^\dagger H\right) S^2 + \frac{\lambda_{\phi SS}}{2}\phi S^2 + \frac{\lambda_{\phi\phi SS}}{2}\phi^2 S^2. \end{aligned} \tag{4.1}$$

The treatment to obtain masses and parameter relations stays the same as explained in the appendix E. Also the constraints on α, due to LHC data and the requirement $\mu_1^3 = \frac{-\mu v^2}{2}$, are the same as in the singlet model. From the interactions in the Lagrangian and the scalar potential new properties arise in this model. On the one hand the coupling of the scalar S to two Higgs bosons H_1 and H_2 instead of one, on the other hand dark matter conversion, $SS \leftrightarrow \chi\chi$, which can influence the relic density. The main focus of this work is on the new features within this framework.

In the two-component dark matter model thirteen parameters are free, but not all are important for dark matter relic density and direct detection. λ_ϕ and λ_S and the choices μ_3=0 and λ_4=0 do not have an impact on phenomenology. Hence, for further investigation nine parameters are taken to be free:

$$M_\chi,\ M_S,\ M_{H_2},\ g_s,\ g_p,\ \sin\alpha,\ \lambda_{\phi SS},\ \mu_{\phi SS},\ \lambda_{\phi\phi SS} \tag{4.2}$$

The quantities M_χ, g_s and g_p are linked to the fermionic component only. M_S, $\lambda_{\phi SS}$, which will be called λ in the following, and $\lambda_{\phi\phi SS}$ only determine properties of the scalar. Both species are related to M_{H_2}, $\sin\alpha$ and $\mu_{\phi SS}$.

4.1. Relic Density

The two dark matter species, the Majorana fermion χ and the real scalar S, require the treatment of two coupled Boltzmann equations. This is described here in general, borrowing from [51]. The Boltzmann equations for the two species with number densities n_1 and n_2 are

$$\frac{\mathrm{d}n_1}{\mathrm{d}t} = -\sigma_v^{11\to \mathrm{SM\ SM}}\left(n_1^2 - n_{1,\mathrm{eq}}^2\right) - \sigma_v^{11\to 22}\left(n_1^2 - n_{1,\mathrm{eq}}^2\frac{n_2^2}{n_{2,\mathrm{eq}}^2}\right) - 3Hn_1, \tag{4.3}$$

$$\frac{\mathrm{d}n_2}{\mathrm{d}t} = -\sigma_v^{22\to \mathrm{SM\ SM}}\left(n_2^2 - n_{2,\mathrm{eq}}^2\right) - \sigma_v^{22\to 11}\left(n_2^2 - n_{2,\mathrm{eq}}^2\frac{n_1^2}{n_{1,\mathrm{eq}}^2}\right) - 3Hn_1, \tag{4.4}$$

with σ_v denoting the thermally averaged cross section times velocity. The superscript specifies for which processes the cross section is taken, 1 and 2 stand for the two dark matter species and SM denotes any Standard Model or rather non-dark matter particle like H_2. The first term describes annihilation into Standard Model particles, the second term accounts for dark matter conversion. The process of conversion enables one dark matter species to annihilate, creating a pair of particles of the other species, hence the relic density of the annihilating species can be reduced while the relic density of the produced species can be enhanced. The third term in the Boltzmann equation models the expansion of the Universe, as in the one dimensional equation (2.17).

Analogous to the case with only one WIMP, the abundances of the WIMPs are $Y_i := \frac{n_i}{s}$ for $i = 1, 2$, while Standard Model particles are assumed to be in equilibrium. Similarly to before $x := \frac{m}{T}$ with $m = \frac{M_1+M_2}{2}$ is introduced. This leads to the evolution equations

$$\frac{\mathrm{d}Y_1}{\mathrm{d}x} = -\left(\frac{45}{\pi M_{\mathrm{Pl}}}\right)^{-1/2} \frac{g_*^{1/2} m}{x^2} \left(\sigma_v^{11\to \mathrm{SM\ SM}}(Y_1^2 - Y_{1,\mathrm{eq}}^2) + \sigma_v^{11\to 22}(Y_1^2 - Y_{1,\mathrm{eq}}^2 \frac{Y_2^2}{Y_{2,\mathrm{eq}}^2})\right), \tag{4.5}$$

$$\frac{\mathrm{d}Y_2}{\mathrm{d}x} = -\left(\frac{45}{\pi M_{\mathrm{Pl}}}\right)^{-1/2} \frac{g_*^{1/2} m}{x^2} \left(\sigma_v^{22\to \mathrm{SM\ SM}}(Y_2^2 - Y_{2,\mathrm{eq}}^2) + \sigma_v^{22\to 11}(Y_2^2 - Y_{2,\mathrm{eq}}^2 \frac{Y_1^2}{Y_{1,\mathrm{eq}}^2})\right). \tag{4.6}$$

The fact that processes like $11 \to 22$ are described by the same matrix element as $22 \to 11$ is used in both set of coupled Boltzmann equations, as it provides a relation between the annihilation cross sections

$$Y_{A,\mathrm{eq}} Y_{B,\mathrm{eq}} \sigma_v^{ABCD} = Y_{C,\mathrm{eq}} Y_{D,\mathrm{eq}} \sigma_v^{CDAB} \tag{4.7}$$

where A, B, C, D are from $\{1, 2, \mathrm{SM}\}$, as shown in the appendix D.

In order to treat the two coupled Boltzmann equations numerically, the Lagrangian is modeled in LanHep [71] and then implemented in micrOMEGAs [72]. For the relic density calculation two independent methods are applied to obtain reliable results. One methods makes use of the built in Runge-Kutta routine in a new micrOMEGAs distribution (not yet public) as described in [51]. The second method follows the implicit trapezoidal strategy explained in the DarkSUSY manual [74] which is used in the DarkSUSY code [73] in order to solve one Boltzmann equation. The adaption to two equations is shown in the appendix H. The values for $\langle \sigma v \rangle$ are computed by micrOMEGAs in both cases, for the scalar some annihilation cross sections have been calculated analytically –see section G.1 in the appendix.
The relic density constraint in this two-component model is

$$\Omega_{\mathrm{DM}} h^2 = \Omega_S h^2 + \Omega_\chi h^2 = 0.1199 \pm 0.0027 \tag{4.8}$$

where Ω_S and Ω_χ are the relic densities of the single components. The fractions for S and χ of the entire relic density are defined as

$$\zeta_\chi := \frac{\Omega_\chi}{\Omega_{DM}} \qquad \text{and} \qquad \zeta_S := \frac{\Omega_S}{\Omega_{DM}} \qquad \text{with} \qquad \zeta_\chi + \zeta_S = 1 \tag{4.9}$$

The influence of the model parameters on relic density and direct detection is first studied without this constraint. Later it is taken into account for detection prospects.

The Boltzmann equations (4.5) and (4.6) contain the annihilation of dark matter into Standard Model particles as well as the conversion of one dark matter species into the other. This process $SS \leftrightarrow \chi\chi$ is mediated by the scalars H_1 and H_2 as shown in figure 4.1.

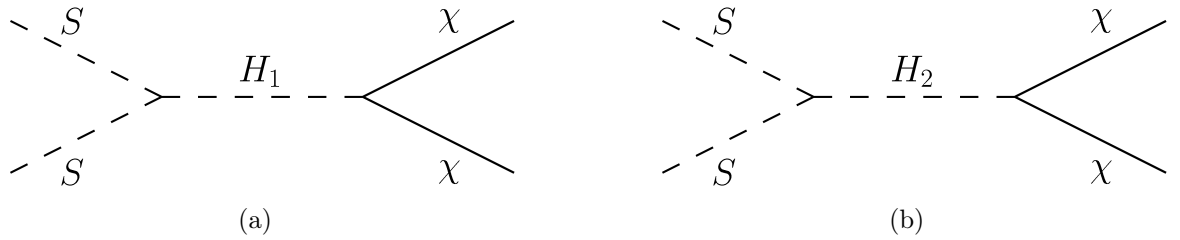

Figure 4.1.: Feynman diagrams for the conversion $\chi\chi \leftrightarrow SS$.

According to the Feynman rules in this model (cf. appendix C.2) the $H_1\chi\chi$ vertex is suppressed by $\sin\alpha$, whereas the $H_2\chi\chi$ vertex is not. Thus the second diagram is more important given that $\mu_{\phi SS}$, which sets the SSH_2 vertex, is large enough. If both dark matter species have similar mass, the conversion takes place in both ways, otherwise it only converts the heavier particle into the lighter one.

To begin with, lets illustrate the relic densities in the absence of conversion processes (they will be treated later).

Figure 4.2 shows the relic density $\Omega_\chi h^2$ of the fermion as function of the fermion mass M_χ for different values of M_{H_2}. By setting $\mu_{\phi SS}$ to zero, the process $SS \to \chi\chi$ is negligible since the H_2 mediated diagram in figure 4.1 is largely suppressed. For all four values of M_{H_2} the lines have the same overall behavior, similar to figure 3.2 in the singlet fermion model: The relic density varies over a large range, it can be as large as 10^3 for low M_χ or largely suppressed down to 10^{-4} at the H_2 resonance. Starting from low masses, the relic density decreases slightly until a large suppression occurs at $2M_\chi = M_{H_1}$ and at $2M_\chi = M_{H_2}$, which is shifted to the according value for each line. The dips correspond to regions with enhanced annihilation cross sections at the Higgs resonances. At $M_\chi = M_{H_2}$ a steep decreases in relic density is observed, corresponding to the process $\chi\chi \to H_2H_2$ becoming accessible. Afterwards all lines have an overall increase with M_χ for larger dark matter masses and feature a general value for the relic density independent of M_{H_2}. For masses below M_{H_2} the main annihilation channel are $\chi\chi \to W^+W-$ and $\chi\chi \to Z^0Z^0$. Above this threshold, H_2H_2 becomes the dominant final state, matching the results in the singlet fermion model.

Similarly, the scalar relic density $\Omega_S h^2$ is displayed in figure 4.3 featuring the same four values of M_{H_2}, while M_χ is equal to 800 GeV. Analogous to the fermion, the scalar relic density is largest for small masses, increases with M_S for large masses and can vary over a many orders of magnitude. Smallest values are obtained on the H_1 resonance for M_S around 62.5 GeV. All lines feature also a dip at the H_2 resonance but compared to H_1 resonance the decrease is small, as the SSH_2 vertex is suppressed by $\sin\alpha$ (cf. appendix section C.2). Common to all lines is also a decrease at $M_S = M_{H_2}$ due to the

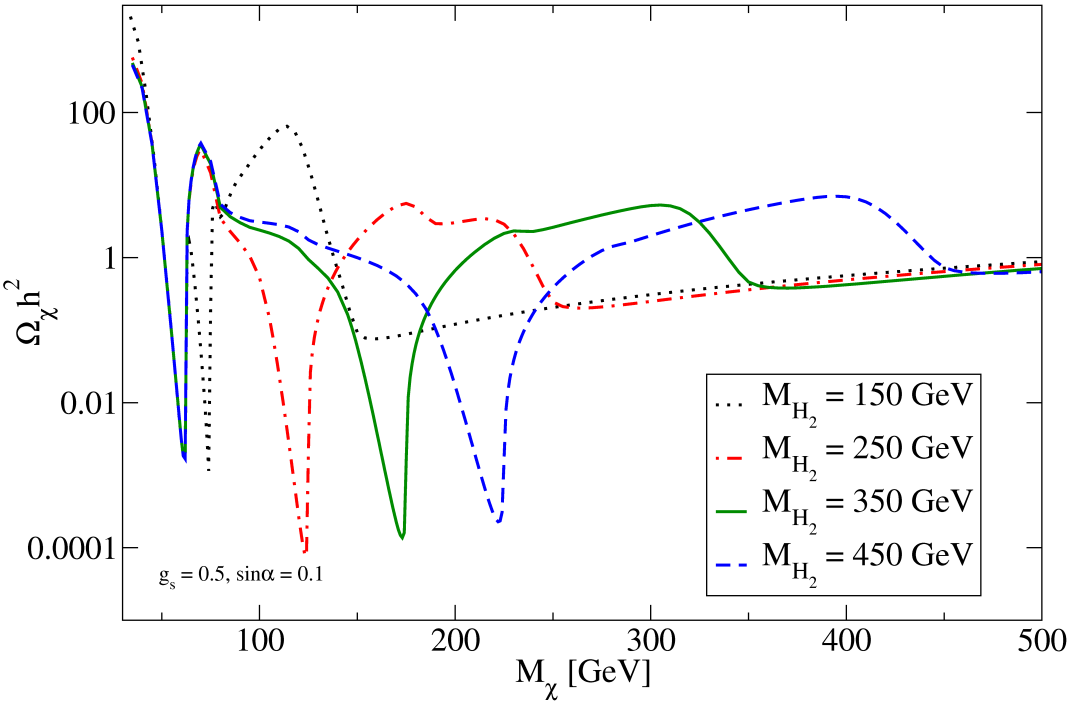

Figure 4.2.: The plot shows the relic density of χ with respect to its mass for negligible conversion and for different values of M_{H_2}: 150 GeV, 250 GeV, 350 GeV and 450 GeV. The other important parameters are set as $g_s = 0.5$, $\sin\alpha = 0.1$ and $M_S = 800$ GeV.

opening of the channel $SS \to H_2H_2$. These two features are new with respect to the singlet scalar model, where H_2 and therefore neither the H_2 resonance nor the opening of the H_2H_2 final state are present. To enhance the new aspects $\lambda_{\phi\phi SS}$ is set to 0.5, which also influences the dominant final annihilation states at larger masses. If $\lambda_{\phi\phi SS}$ is large enough, the most common final state for large M_S is H_2H_2, for low masses anyway, it is W^+W^-.

To illustrate the effect of conversion, $\mu_{\phi SS}$ is now allowed to be non-zero. For the relic density calculation of χ it is set to 100 GeV. The result as a function of M_χ for three different values of M_S is shown in figure 4.4. The other parameters are taken as $M_{H_2} = 700$ GeV, $\sin\alpha = 10^{-3}$ and $g_p = 0.5$, while the rest is set to zero.

The line for $M_S = 60$ GeV (green solid) features mostly relic densities smaller than or equal to to the other lines. The reason is that the channel $\chi\chi \to SS$ is open over the entire mass range. Compared to this, the relic density for $M_S = 400$ GeV (red dash-dotted line) is larger for fermion masses smaller than M_S. At $M_S = M_\chi = 400$ GeV a steep decrease of occurs as the new channel $\chi\chi \to SS$ opens up, afterwards the

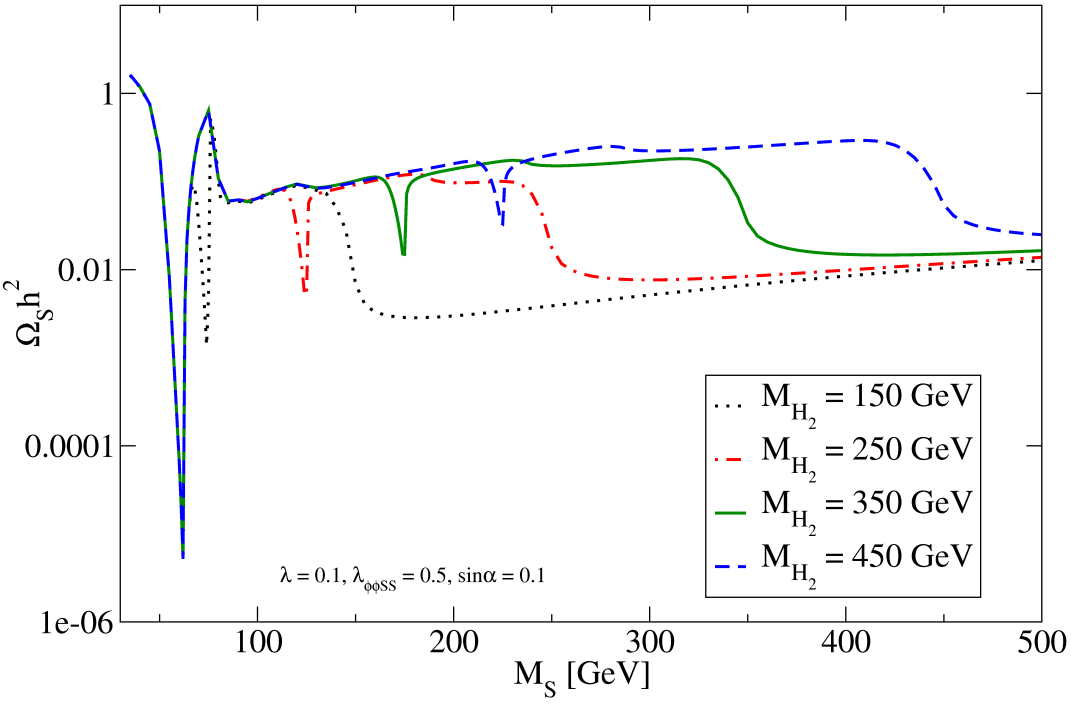

Figure 4.3.: The scalar relic density versus the scalar mass is shown for $M_\chi = 800$ GeV and various values of M_{H_2}: 150 GeV, 250 GeV, 350 GeV and 450 GeV. The other important parameters are $\lambda = 0.1, \lambda_{\phi\phi SS} = 0.5$ and $\sin\alpha = 0.1$.

line overlaps with the 60 GeV curve. Common to all three values of M_S is also the relic density suppression at the H_2 resonance. Choosing $M_S = 800$ GeV (black dashed line) leads to the same relic density as for 400 GeV up to M_χ reaching the value of 400 GeV. Until M_χ is larger than 600 GeV the relic density increases in this case. Then a soft decrease occurs due to the channel $\chi\chi \to H_2H_2$ becoming accessible. Once the dark matter mass reaches $M_S = 800$ GeV all three lines coincide, as conversion is allowed. This illustrates that conversion can decrease the relic density by more than two orders of magnitude.

The impact of conversion on the S relic density shows a slightly different behavior as presented in figure 4.5. The relic density of the scalar is shown as a function of M_S featuring different M_χ. Mostly, similar behavior to the fermion relic density is observed, the dip at the H_2 resonance and the decrease in relic density as new channels become accessible, but there is a difference between $M_\chi = 400$ GeV and 800 GeV for small values of M_S. This feature can be explained by residual conversions of the heavier fermion into the scalar. Figure 4.6 shows the evolution of fermion and scalar abundances for two different values of M_χ while M_S is equal to 200 GeV and all other parameters are the same as in figure 4.5. The equilibrium distributions are shown as dashed lines with

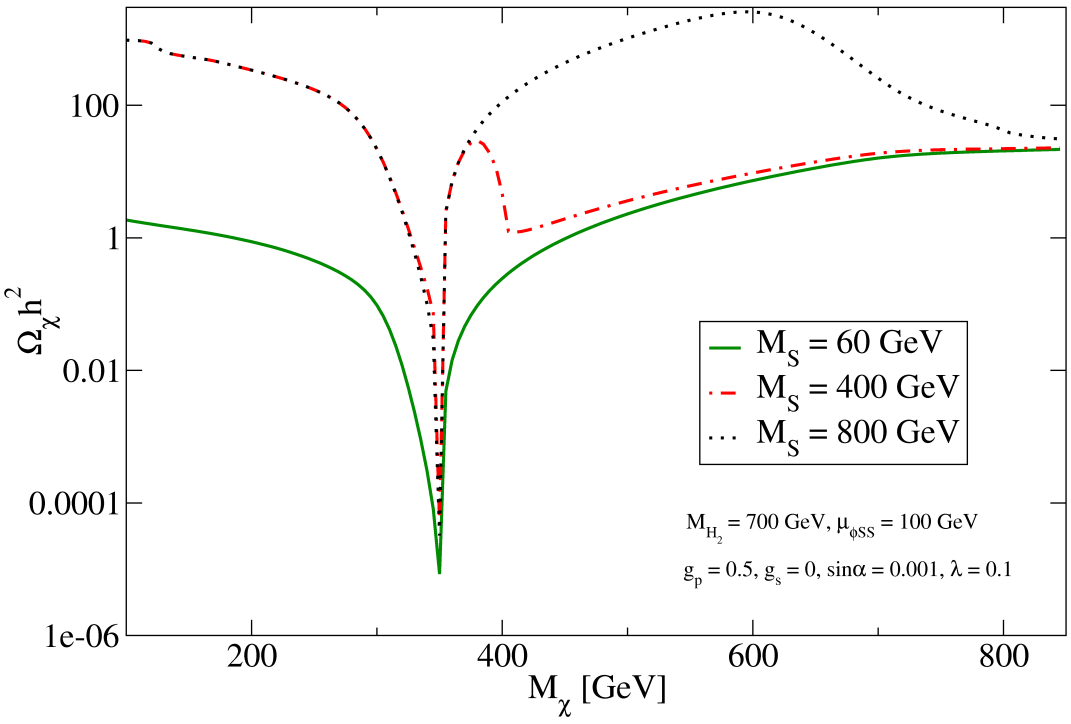

Figure 4.4.: The relic density of the fermion is plotted as a function of fermion mass for three values of M_S: 60 GeV, 400 GeV and 800 GeV. The other parameters are set to $M_{H_2} = 700$ GeV, $\mu_{\phi SS} = 100$ GeV, $g_p = 0.5$, $g_s = 0$, $\sin\alpha = 0.001$ and $\lambda = 0.1$.

colors corresponding to the abundances displayed as solid lines. First the abundances track the equilibrium values, which are suppressed by the Boltzmann factor, until the individual freeze-out temperature is reached. Then the abundances refrain to a constant value. As expected, for M_χ at 800 GeV the χ abundance (blue solid line) is larger than the abundance for 400 GeV (green solid line). Interestingly, the same is true for the abundance of the scalar, it is larger for $M_\chi = 800$ GeV (yellow solid line) than for 400 GeV (red solid line). In both cases M_χ is larger than M_S, hence conversion of χ into S is allowed. After the freeze-out the interaction rate of χ becomes small and only little residual conversion processes happen, as χ freezes out at higher temperatures than S. For $M_\chi = 400$ GeV, Y_χ is about one order of magnitude smaller than Y_S, thus residual conversion does not have a large impact on the S abundance. But for M_χ at 800 GeV the final abundance Y_χ is around one order of magnitude larger than Y_S, so there is an influence from residual annihilation. The large abundance of χ leads to a noticeable amount of conversion processes after freeze-out, enhancing the abundance of S. Hence conversion and the parameter controlling it, $\mu_{\phi SS}$, can have an impact on relic density in

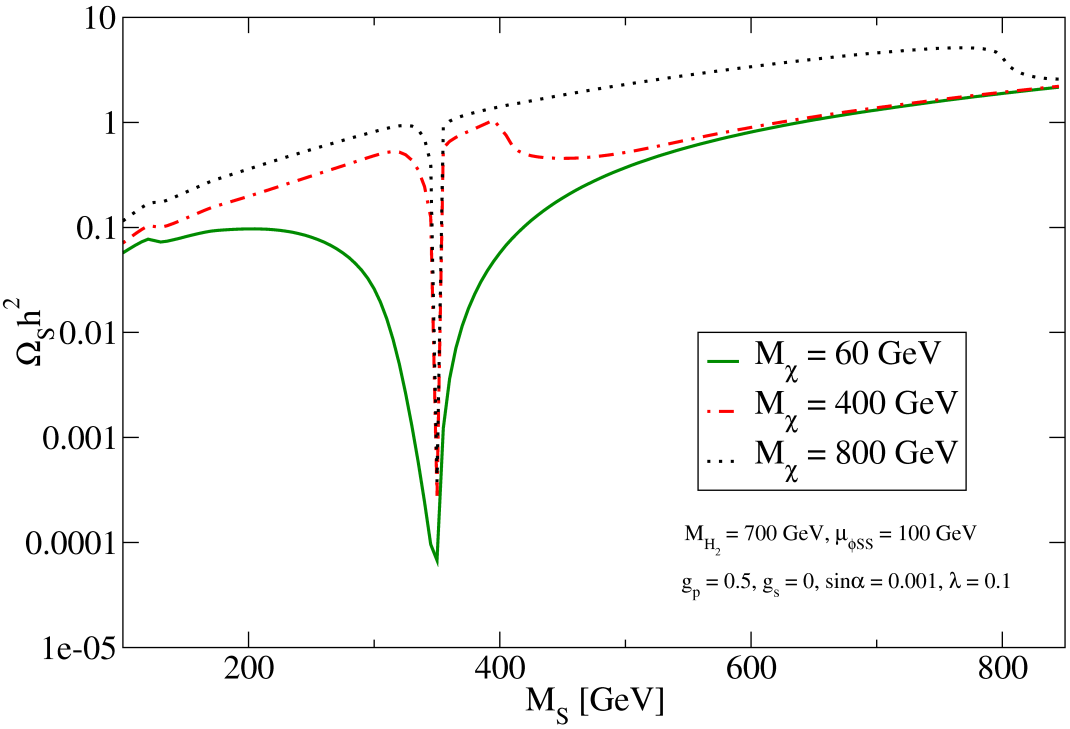

Figure 4.5.: The relic density of the scalar is plotted against its mass for three values of M_χ: 60 GeV, 400 GeV and 800 GeV. The other parameters are $M_{H_2} = 700$ GeV, $\mu_{\phi SS} = 100$ GeV, $g_p = 0.5$, $g_s = 0$, $\sin\alpha = 0.002$ and $\lambda = 0.1$.

a non-expected way. The relic density of the fermion is shown in figure 4.7 with respect to its mass M_χ for different values of $\mu_{\phi SS}$. The other important input parameters are fixed as stated in the figure, parameters that are not listed are set to zero. Overall, for larger $\mu_{\phi SS}$ the relic density becomes smaller, as a larger amount of χ annihilates to S for larger $\mu_{\phi SS}$ reducing the relic density. For masses larger than 700 GeV the influence of $\mu_{\phi SS}$ is less distinct and all four lines lie closer together. For $\mu_{\phi SS} = 100$ GeV (green solid line) the process $SS \to \chi\chi$ is dominant over the whole mass range, so no decrease in relic density is observed when the channel $\chi\chi \to H_2H_2$ opens at M_χ around M_{H_2}=700 GeV. For $\mu_{\phi SS}$ at 1 GeV (black dotted line) and 10 GeV (blue dashed line) conversion is less present and the threshold for H_2 production is important, clearly reducing the relic density once the new final state is available.

As we have seen, the behavior of the relic density in this model presents new features with respect to the singlet scalar and singlet fermion model: The interplay between S and the second Higgs boson H_2, the resonance at $2M_S = M_{H_2}$ as well as the new final states H_1H_2 and H_2H_2 for S annihilation, and dark matter conversion processes

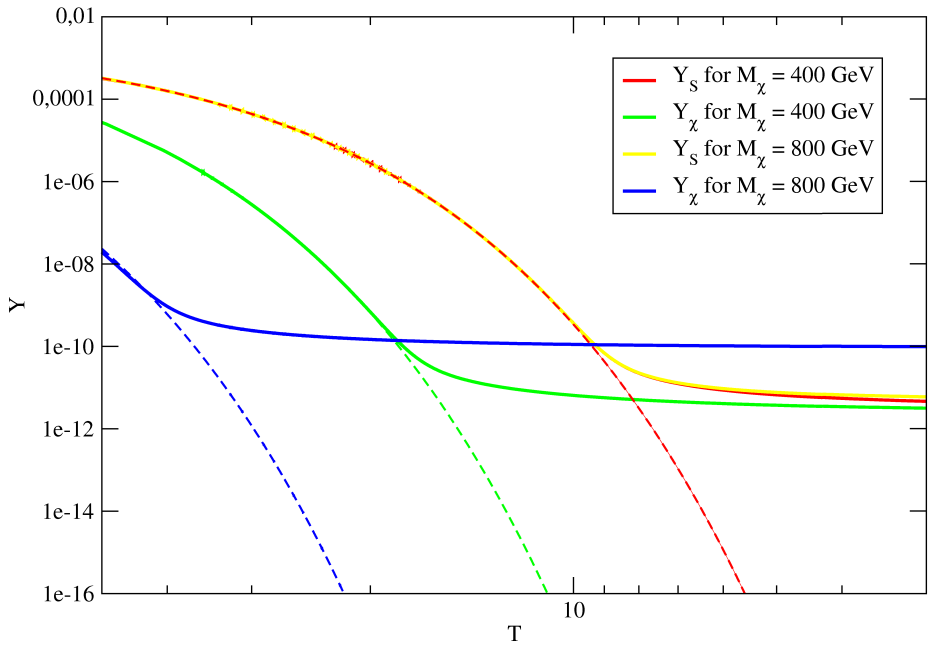

Figure 4.6.: The evolution of relic abundances for S and χ with temperature are shown for two different values of M_χ, 400 GeV and 800 GeV, while M_S is fixed at 200 GeV and the other important parameters are the same as in figure 4.5.

$SS \to \chi\chi$ which can decrease the relic density of the heavier component while increasing the one of the lighter particle. Hence the viable parameter regions in this model are not the same as in the singlet scalar and singlet fermionic models.

4.2. Direct Detection

Direct detection experiments impose strict bounds on dark matter models as stated in previous sections. In the singlet scalar and singlet fermion model large regions of the parameter space are already excluded.

In this two-component model both spin-independent direct detection cross sections are large and it is expected that most bounds change little with respect to the singlet models. As χ and S contribute only by a fraction ζ_χ and ζ_S to the relic density, direct detection experiments do not constrain the spin-independent direct detection

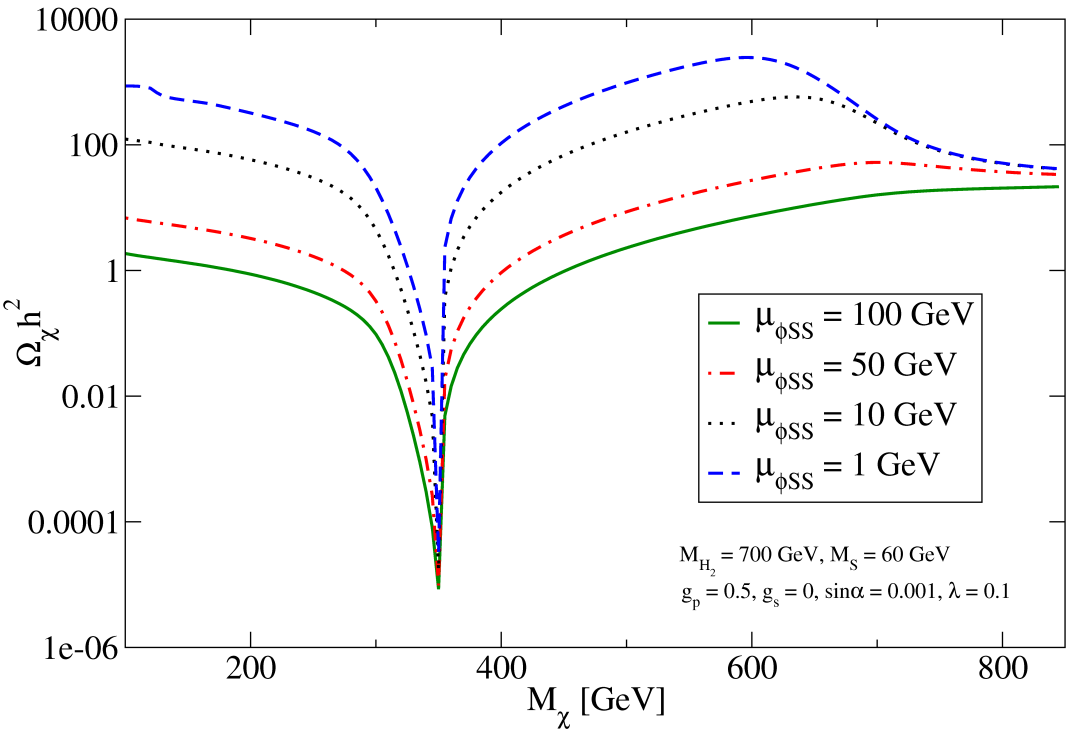

Figure 4.7.: The relic density of χ is plotted as a function of its mass for four different values of $\mu_{\phi SS}$: 1 GeV, 10 GeV, 50 GeV and 100 GeV. The other parameters are chosen as $M_{H_2} = 700$ GeV, $M_S = 60$ GV, $g_p = 0.5$, $g_s = 0$, $\sin\alpha = 0.001$ and $\lambda = 0.1$.

cross sections $\sigma_{\chi,\mathrm{SI}}$ and $\sigma_{S,\mathrm{SI}}$ but the quantities $\zeta_\chi\sigma_{\chi,\mathrm{SI}}$ and $\zeta_S\sigma_{S,\mathrm{SI}}$. Yet the direct detection rate has no strong dependence on ζ [75]. The ζ suppression is alleviated, as smaller values of ζ require larger couplings like λ or g_s to achieve the correct relic density. Larger couplings however result in larger direct detection cross sections, reversing the effect of small ζ, thus there is no suppression. For indirect detection ζ is important, as the detection rate σv has to be multiplied by ζ^2. This leaves a ζ suppression after taking into account the influence of larger couplings to achieve the right relic density. So in general direct detection is more feasible for multi-component dark matter models than indirect detection.

As the vertices for the fermion interacting with Standard Model particles are not altered with respect to the singlet fermionic model, the direct detection cross section stays the same as equation (3.7) and the important model parameters are still α, g_s, M_χ and M_{H_2}. Regarding the scalar, a new H_2 contribution appears. The interaction

between S and nucleons is mediated by t-channel exchange of the two scalars H_1 and H_2, as shown in figure 4.8.

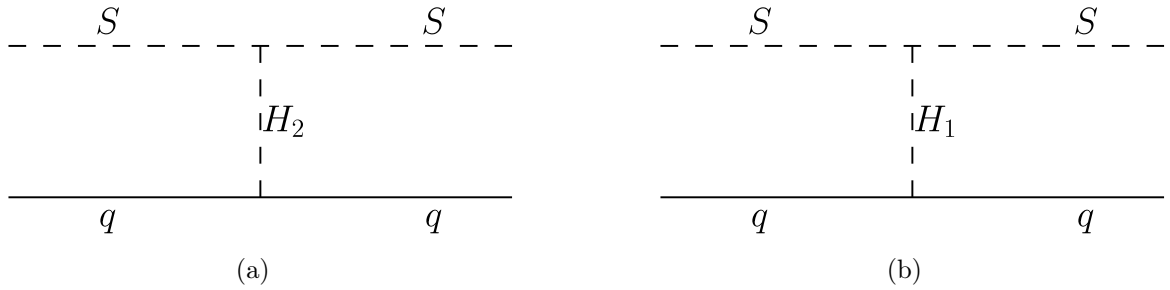

Figure 4.8.: Feynman diagrams for the direct detection of S.

The spin independent direct detection cross section is

$$\sigma_{S,\mathrm{SI}} = \frac{M_r^2}{8\pi M_{H_1}^4 M_{H_2}^4 M_S^2} \left(\frac{\lambda_{HSS} v}{2} \left(\cos^2\alpha M_{H_2}^2 + \sin^2\alpha M_{H_1}^2 \right) + \lambda \cos\alpha \sin\alpha \left(M_{H_1}^2 - M_{H_2}^2 \right) \right)^2 g_{Hp}^2 \tag{4.10}$$

where g_{Hp} is the same as given in equation (3.8).The derivation is summarized explicitly in section G.2 in the appendix. The cross section is determined by M_S, λ, $\sin\alpha$, M_{H_2} and $\mu_{\phi SS}$. Interestingly, the second term, which is proportional to the conversion parameter $\mu_{\phi SS}$, may cancel with the first term, suppressing the cross section. The cancellation happens for

$$\lambda_{canc} = \frac{\lambda_{HSS} v}{2} \left(\frac{\cos\alpha}{\sin\alpha} + \frac{M_{H_1}^2}{\left(M_{H_2}^2 - M_{H_1}^2 \right) \cos\alpha \sin\alpha} \right) \tag{4.11}$$

which is independent of the dark matter masses. This cancellation effect is illustrated in figure 4.9, which shows the direct detection cross section $\sigma_{S;\mathrm{SI}}$ as a function of M_{H_2} for different values of $\mu_{\phi SS}$. For a vanishing value of $\mu_{\phi SS}$ (solid red line), there is no cancellation. The cross section does not depend on M_{H_2}, therefore it is constant over the whole mass range. This line acts as a reference for the four non-zero values of $\mu_{\phi SS}$. Setting $\mu_{\phi SS}$ to 50 GeV (blue dash-dotted line) decreases the direct detection cross section over the entire shown mass range. It is nearly two orders of magnitude below the reference value. For $\mu_{\phi SS} = 100$ GeV (dotted black line) a large dip is visible around $M_{H_2} \approx 200$ GeV corresponding to a cancellation. This decrease of almost six orders of magnitude is the largest suppression achieved within this set of parameters. Allowing $\mu_{\phi SS}$ to take higher values, like 200 GeV (green dashed line) and 300 GeV

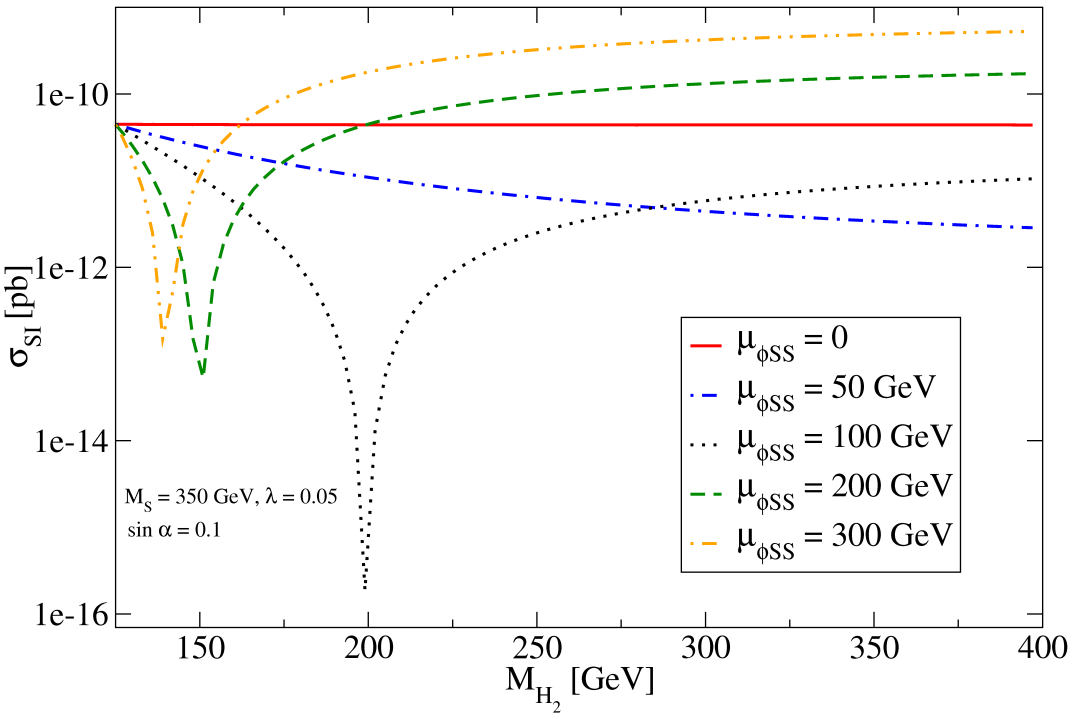

Figure 4.9.: The scalar spin-independent cross section as a function of M_{H_2} is shown for different values of $\mu_{\phi SS}$: 0 GeV, 50 GeV, 100 GeV, 200 GeV and 300 GeV. The other important parameters are $M_S = 350$ GeV, $\lambda = 0.05$ and $\sin\alpha = 0.1$.

(yellow dash-dotted line), moves the cancellation dips towards smaller M_{H_2} around 150 GeV. The decrease in the cross section is not as drastic as for $\mu_{\phi SS} = 100$ GeV and there is also an enhancement of the cross section at larger masses.

To illustrate this further, figure 4.10 displays the scalar direct detection cross section as a function of M_S for a fixed value of $\mu_{\phi SS} = 100$ GeV while various values of M_{H_2} are considered. According to equation (4.10), all lines decrease with increasing values of M_S. The dependence of σ_{SI} on M_{H_2} is clearly non-trivial as seen in equation (4.11). At $M_{H_2} = 200$ GeV (blue dash-dotted line) the suppression is largest, hence smallest values of $\sigma_{S,\mathrm{SI}}$ are achieved. They lie up to four order of magnitude lower than all other lines. Largest cross sections are obtained for M_{H_2} at 150 GeV (red solid line) and 500 GeV (orange dash-double dotted line). Both feature nearly the same cross section.

To summarize, while the behavior of the spin independent cross section for χ is the same as in the fermionic singlet model, the scalar one receives a new contribution medi-

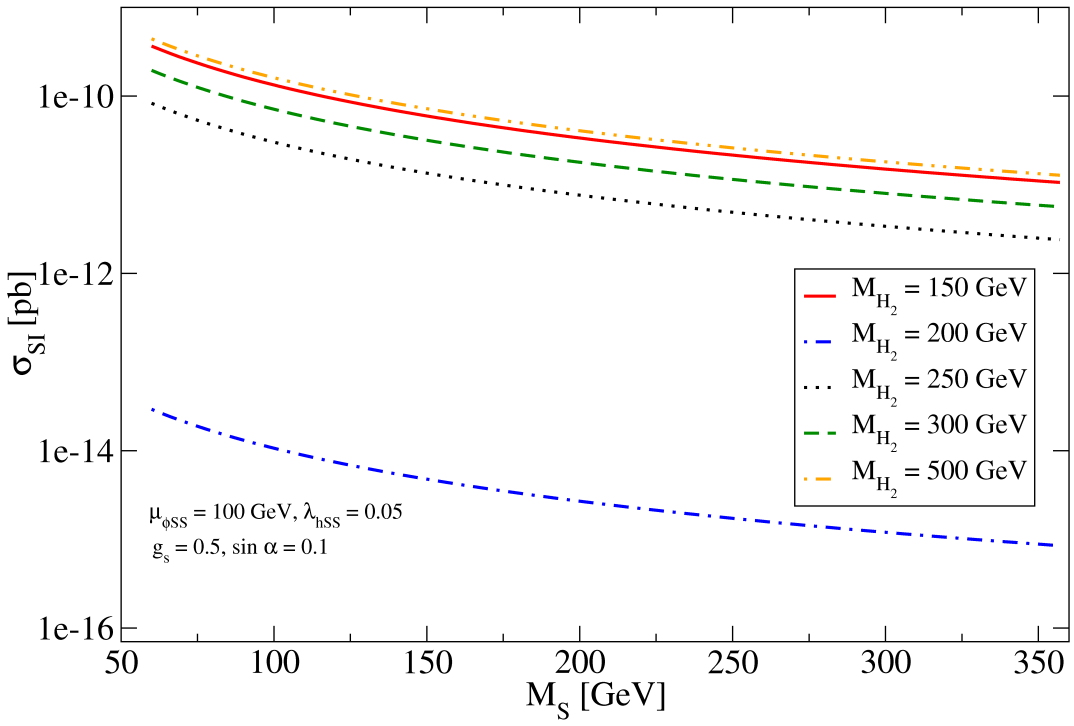

Figure 4.10.: For five different values of M_{H_2}, 150 GeV, 200 GeV, 250 GeV, 300 GeV and 500 GeV, the scalar direct detection cross section is plotted against the scalar mass M_S. And $\mu_{\phi SS}$ equals 100 GeV, λ is 0.5, g_s is 0.5 and $\sin\alpha$ equals 0.1.

ated by H_2. This new contribution may either lead to an enhancement or a suppression of the spin-independent direct detection cross section for S.

4.3. Detection Prospects

To illustrate the dark matter detection prospects in this model, five benchmark points compatible with all current bounds have been selected. For all points g_p and $\lambda_{\phi\phi SS}$ are set to zero. The other parameters are shown in table 4.1 along with the calculated relic density, the spin-independent direct detection cross section and the indirect detection rate σv. Figure 4.11 displays the direct detection cross sections of all five benchmark models with respect to the dark matter masses, an index S respectively χ denotes the quantities regarding the scalar or fermionic component. The current bound by LUX [26] (red solid line) and the expected sensitivity of XENON1T [25] (blue dash-dotted line) are also implemented.

Table 4.1.: The parameters of the five benchmark models along with the computed relic density, direct detection cross section and annihilation rates are shown.

Parameters / Model	I	II	III	IV	V
M_S [GeV]	52	200	300	120	220
M_χ [GeV]	70	180	400	165	280
M_{H_2} [GeV]	200	150	200	360	250
$\lambda_{\phi SS}$ [GeV]	400	0	0	0	0
g_s	0.45	0.58	0.9	0.65	0.6
sinα	0.1	0.1	0.07	0.08	0.05
λ	0.25	0.175	0.25	0.09	0.5
Ω_S/Ω_{DM} [%]	52	51	49	97	8
Ω_χ/Ω_{DM} [%]	48	49	51	3	92
$\sigma_{SI,S}$ [pb]	2.9×10^{-12}	1.7×10^{-9}	1.5×10^{-9}	1.2×10^{-9}	1.1×10^{-8}
$\sigma_{SI,\chi}$ [pb]	6.6×10^{-10}	1.8×10^{-10}	8.7×10^{-10}	1.2×10^{-9}	$3.0\times10-10$
$\langle\sigma v\rangle_S$ [10^{-26}cm^3/s]	7.2	4.7	4.5	2.2	30
$\langle\sigma v\rangle_\chi$ [10^{-26}cm^3/s]	1.6×10^{-8}	4.5×10^{-5}	4.2×10^{-5}	2.7	2.1×10^{-5}

Model I:

The two dark matter species are rather light with $M_S = 65$GeV and $M_\chi = 75$GeV and both give about 50 % of the relic density. Usually such low mass models are highly constrained by direct detection (cf. figure 2.11). Yet, this specific model is not within the sensitivity of current experiments due to the large value of $\mu_{\phi SS}$. It enhances conversion of χ to S and still allows small values for g_s while achieving the correct relic density. The cancellation effect mentioned before (cf. equation (4.11)) suppresses the cross section $\sigma_{S,\mathrm{SI}}$ of the scalar. Thus it is even below the expected XENO1T sensitivity, but the fermion is within the reach of future experiments.

Model II:

The dark matter masses are intermediate with $M_S = 200$GeV and $M_\chi = 180$GeV and the two components contribute the same amount to the relic density. The main annihilation channel determining the relic density of the fermion is $\chi\chi \to H_2H_2$ as $M_{H_2} = 150$GeV is below M_χ. Since M_{H_2} is also close to $M_{H_1} = 125$GeV, the fermionic

direct detection cross section is slightly suppressed according to equation (3.7). It is one order of magnitude below the scalar one, even though both species are detectable by future experiments.

Model III:

The two heavy dark matter species, with $M_S = 300\text{GeV}$ and $M_\chi = 400\text{GeV}$, convey 50 % of the total relic density each. The important annihilation channels are $\chi\chi \to H_2 H_2$ and $SS \to W^+W^-$, while μ_{phiSS} is zero and conversion does not occur. The cross sections obtained with this set of parameters are both within the reach of XENON1T, although $\sigma_{S,\text{SI}}$ is a bit larger than $\sigma_{\chi,\text{SI}}$.

Model IV:

The dark matter masses are intermediate with $M_S = 120\text{GeV}$ and $M_\chi = 165\text{GeV}$, but the scalar contributes around 97 % to the relic density and its direct detection cross section is close to the bound from LUX. The fermionic relic density is only about 3 % ,as $2M_\chi \approx M_{H_2}$ is close to the H_2 resonance and so annihilation on the early Universe is very efficient. Despite this, the fermion is detectable by future experiments. So, experiments can probe dark matter contributions of both species, even if one is subdominant at the percent level.

Model V:

The scalar in this model with intermediate masses, $M_S = 220\text{GeV}$ and $M_\chi = 280\text{GeV}$, provides only 8% of the total relic density, due to a large value of λ. Yet, both species are within the reach of XENON1T. This illustrates further the accessibility of subdominant dark matter species in direct detection experiments.

Regarding indirect detection the annihilation rates σv are rather small and there is an additional suppression by ζ. For the fermion $\sigma_\chi v_\chi$ is already very small in all five models without ζ_χ, as in the singlet fermionic model. The fermion annihilation cross section is velocity dependent, hence the annihilation rate $\sigma_\chi v_\chi$ is proportional to v_χ^2, which is small considering the dark mater velocities in the Galactic halo. For the scalar there is no high suppression of the annihilation rate, but the values fall below the thermal value of $3{\times}10^{-26}$ cm^3/s when taking the ζ_s suppression into account.

Overall indirect detection prospects for the fermion are rather unpromising for this multi component dark matter model, whereas the annihilation cross sections of the scalar can be close to the thermal value.

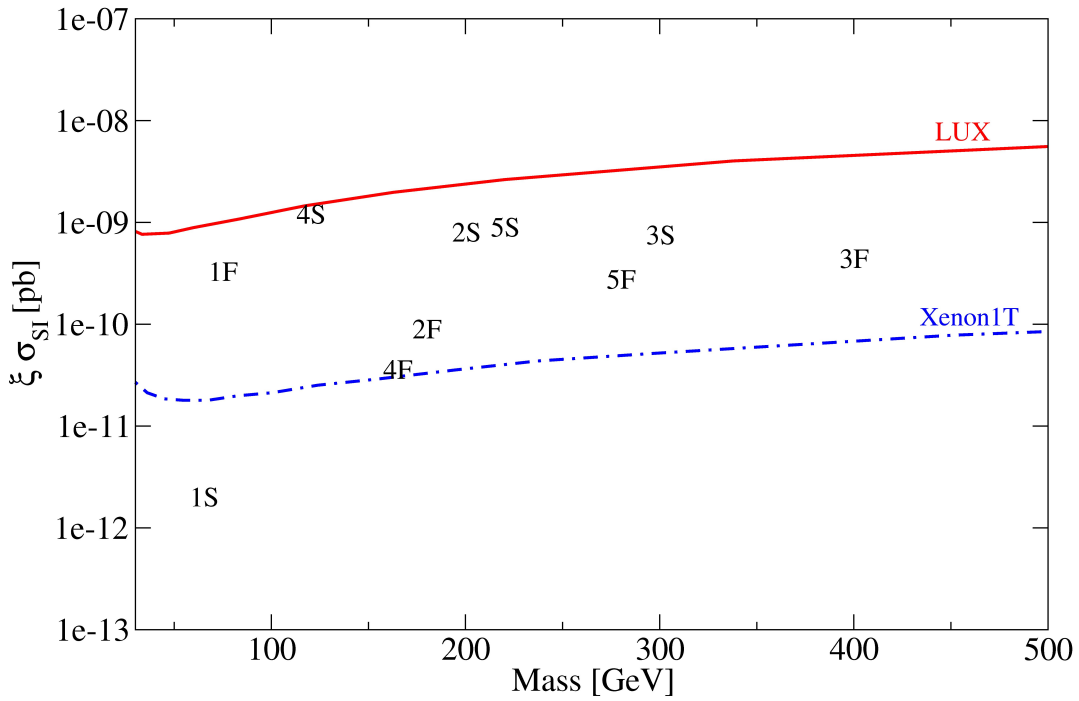

Figure 4.11.: The five benchmark models are shown in the plane (Mass,$\zeta\sigma_{\mathrm{SI}}$). The curves are current (LUX) and future (XENON1T) direct detection limits.

4.4. Summary

A new minimal two dark matter component model, which can be seen as a fusion of the singlet scalar and the singlet fermionic dark matter model, has been presented and analyzed. Three new fields, two scalars and one fermion, are added to the Standard Model, all singlets under the gauge group. The fermion as well as one of the scalars are odd under a newly introduced symmetry, thus the lightest odd particle is stable. Nicely, an accidental symmetry stabilizes the heavier particle also. Hence, two dark matter species are present and both contribute to the entire dark matter relic density. Even though this model can be seen as union of the singlet models, it has some new features on its own: The process of dark matter conversion can have a non-negligible effect on the relic density. It can either increase or lower the value with respect to the computation without conversion. Another novel feature concerns the dark matter scalar. Its direct detection cross section receives new contributions, which can either enhance or reduce the cross section.
Regarding direct detection, the scalar and fermionic component mostly feature direct detection cross sections within the reach of future one ton experiments as XENON1T. Interestingly, it is possible to detect both species, even if one provides only a few percent

of the entire relic density. As the annihilation rate for the fermion can be largely suppressed, indirect detection of it is rather unfeasible. In general this two-component model is better probable by direct detection than indirect detection.

5. Conclusion

Astrophysical and cosmological observations based on gravitational effects supply evidence for dark matter on all scales. To name a few: small temperature fluctuations in the CMB, the process of structure formation or the rotation curves of galaxies hint towards dark matter. According to recent measurements about 25% of the Universe's energy content is matter, but only 5% consists of known baryonic matter. The rest is dark matter. This new kind of matter is colorless, electrically neutral and stable compared to the lifetime of the Universe. It is hoped to detect and identify dark matter in many experiments, observing interactions between dark matter particles and the Standard Model ones. The nature of the interactions involving the hidden sector are described by many theories. Some are complex and yield a broad variety of different parameters while containing a natural dark matter candidate, like the LSP in SUSY, others are minimalistic and very plain. Such minimal models are rather simple by construction and allow for an easy confrontation with current experimental bounds.

In this thesis two minimal models for weakly interacting massive particles (WIMPs) were presented and analyzed in detail: The fermionic singlet dark matter model is revisited, revealing new aspects of its phenomenology, additionally a novel model for two-component dark matter was proposed. Both confirm that there is a rich phenomenology to these minimal models, which allows to make predictions regarding feasibility, direct and indirect detection.

The fermionic singlet dark matter model adds two new particles to the Standard Model, one Majorana fermion χ and a real scalar ϕ, both are singlets under the gauge group. In order to make χ stable dark matter an additional $\mathbb{Z}_2$ symmetry is imposed. Under this new symmetry all Standard Model particles and ϕ are even, while χ is odd. As ϕ is evenly charged under the new $\mathbb{Z}_2$, it mixes with the Higgs boson, giving rise to two mass eigenstates H_1 and H_2. The extended Higgs sector mediates all interactions of ϕ and the Standard Model, linking the visible sector to the dark sector. The allowed interactions, as they are renormalizable, are either parity conserving or parity violating denoted by the scalar coupling g_s and the pseudoscalar coupling g_p.

An extensive random scan of the entire parameter space in this framework was done for the parity conserving case with $g_p = 0$ and for the general case with $g_p \neq 0$. For each case 10^5 models were generated which fulfill current experimental and theoretical bound, except for direct and indirect detection. First the viable parameter regions were identified and characterized by projecting the models onto different planes, confirming that models compatible with the relic density constraint are present in a large region of

the parameter space. Special attention is paid to resonances and thresholds, as it was shown, that they can have a large impact on direct detection bounds. One way to evade direct detection while still obtaining the right relic density is the indirect Higgs portal, $\chi\chi \to H_1 H_2$, which has not been considered in previous works. It offers viable models at lower dark matter masses than the process $\chi\chi \to H_2 H_2$, which was mentioned before, and also the feasibility of resonant models is confirmed. In general, direct detection limits from XENON100 were found to exclude a large region of the parameter space in the parity conserving case, yet there are feasible models. Future experiments will be able to probe most of the region below the H_2 resonance, excluding even larger regions of the parameter space.

Similarly, the general case was investigated, the viable parameter regions are identified and confronted with current direct detection bounds. As new contribution to the annihilation rate originate from g_p, the relic density constraint is easier fulfilled while the direct detection cross sections can still be small. On account of this, the direct detection bounds become weaker, consequently no entire region in the plane (M_{H_2}, M_χ) is excluded. And due to the weaker constraints, indirect detection becomes more promising. Hence it is possible to achieve equilibrium for dark matter annihilation in the Sun, resulting in large neutrino and muon fluxes within the reach of current experiments. It is found, however, that all models with high fluxes were already excluded by direct detection bounds, so no new constraints were obtained.

The two-component dark matter model extends the framework of the fermionic singlet dark matter by another scalar field S, which is also odd under the $\mathbb{Z}_2$ symmetry. The lighter of the two odd particles is stabilized by the $\mathbb{Z}_2$ symmetry, while the heavier is stable by an accidental symmetry. Thus two dark matter candidates are present in this model, which requires the treatment of two coupled Boltzmann equations. A novel feature in the two-component model is the process of dark matter conversion $\chi\chi \to SS$, which can either increase or decrease the relic density of a species. Interestingly, residual annihilations of the heavier species after the freeze-out can raise the relic density of the lighter particle, which has not been expected.

The spin independent cross section of the fermion is the same as in the fermionic singlet model, while the scalar-nucleon interaction receives a new contribution due to H_2, which may suppress or increase the scalar cross section. In order to confront the two-component model with current direct detection limits, a set of five benchmark models was generated, which fulfill the usual phenomenological and cosmological bounds. Their relic densities were computed along with the spin-independent direct detection cross sections and the annihilation rates today. It was demonstrated that the benchmark models mostly lie within the reach of future 1-ton experiments and interestingly, in nearly all models it is possible to probe both dark matter contributions, even when one component may only convey a small percentage of the total relic density.

Indirect detection of the fermion, as in the fermionic singlet model, is not feasible.

Particularly, as there is a further suppression of the detection rate by the dark matter fraction. For the scalar, it is possible to reach annihilation rates around the thermal value even when taking the suppression by the dark matter fraction into account.

Both, the fermionic singlet and the two-component model, extend the Standard Model in a minimal way. Only few particles are added, yet there is a rich phenomenology, with manageable calculations which allow for an easy confrontation with current experimental limits. In both models it is possible to find regions in the parameter space which are consistent with the relic density bound and are not yet excluded by direct detection. Also there are parameter points which will be probed by future one-ton experiments, restricting the parameter space more. It is found that both models are better probable via direct detection than indirect observations.

A. Conventions, γ Matrices and Trace Theorems

All parts regarding Dirac algebra, γ-matrices, trace theorems and the general calculation of scattering amplitudes and cross sections and kinematics are based on [3]. This comprises only a short overview and few detailed derivations.

Units

Throughout the whole thesis natural units

$$\hbar = c = k_b = 1 \tag{A.1}$$

are used, unless it is stated differently. For example, masses in natural units are given in eV which is $\mathrm{eV/c^2}$ in real units.

Completeness Relation

The completeness relation for Dirac spinors u and v is

$$\begin{aligned} \sum_s u(p,s)\overline{u}(p,s) &= (\not{p} + M^2), \\ \sum_s v(p,s)\overline{v}(p,s) &= (\not{p} - M^2) \end{aligned} \tag{A.2}$$

for particles with four-momentum p, which obeys $p^2 = M$.

γ Matrices

The Dirac or γ matrices algebra is defined by the anticommutator relation

$$\{\gamma^\mu,\ \gamma^\nu\} = \gamma^\mu\gamma^\nu + \gamma^\nu\gamma^\mu = 2g^{\mu\nu}. \tag{A.3}$$

Throughout this work, the short notation $\not{p} = \gamma_\mu p^\mu$ is used, for four-vectors p.

γ^5 Identities

Based on the four γ-matrices, a fifth matrix is defined as

$$\gamma^5 := i\gamma^0\gamma^1\gamma^2\gamma^3 \tag{A.4}$$

which obeys

$$\gamma_5^2 = 1, \tag{A.5}$$
$$\{\gamma_5,\ \gamma^\nu\} = 0 \tag{A.6}$$
$$\mathrm{Tr}(\gamma^5) = 0, \tag{A.7}$$

where Tr() denotes the trace.

Hermitian Conjugates

Hermitian conjugates for γ matrices are as follows

$$\gamma^{0\dagger} = \gamma^0, \tag{A.8}$$
$$\gamma^{i\dagger} = -\gamma^i, \tag{A.9}$$
$$\gamma^{5\dagger} = \gamma^5 \tag{A.10}$$

with i running from one to three. For a spinor matrix element including any collection of γ-matrices Γ the Hermitian conjugate is given by

$$[\overline{u}(p',s')\Gamma u(p,s)]^\dagger = \overline{u}(p,s)\overline{\Gamma}u(p',s') \tag{A.11}$$

where

$$\overline{\Gamma} := \gamma^0\Gamma\dagger\gamma^0\ . \tag{A.12}$$

Especially for Dirac matrices:

$$\overline{\gamma^0} = \gamma^0, \tag{A.13}$$
$$\overline{\gamma^i} = \gamma^i, \tag{A.14}$$
$$\overline{\gamma^5} = -\gamma^5. \tag{A.15}$$

Trace Theorems

Using the Dirac algebra, the following trace theorems can be proven:

$$\begin{aligned} Tr(\not{a}\not{b}) &= 4ab, \\ Tr(\not{a}\not{b}\not{c}\not{d}) &= 4[(ab)(cd) + (ad)(bc) - (ac)(bd)], \\ Tr(\not{a}\gamma^5) &= 0, \\ Tr(\not{a}\not{b}\gamma^5) &= 0\ . \end{aligned} \tag{A.16}$$

B. Relativistic Kinematics and Cross Sections

Considering two body processes, it is comfortable to fix conventions for kinematics in the center of mass system.

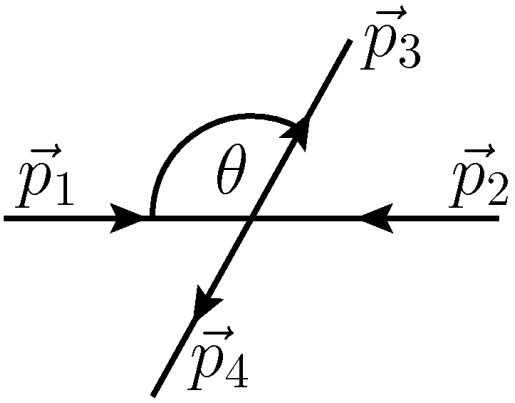

Figure B.1.: Kinematics

Figure B.1 shows a 2 to 2 body scattering process. If not stated differently, throughout this work, the two incoming particles have momenta $\vec{p}_1$ and $\vec{p}_2$ and energies E_1, E_2, the assigned 4-momenta are $p_{1,2} = (E_{1,2}, \vec{p}_{1,2})$. θ denotes the center of mass scattering angle as marked in the figure. The outgoing particles are associated with four-momenta p_3 and p_4 and energies E_3 and E_4. The relativistic energy-momentum relation is obtained by calculating the Lorentz invariant of four-momentum p,

$$p^2 = E^2 - \vec{p}^{\,2} \tag{B.1}$$

while making use of the mass-shell condition

$$p^2 = M^2. \tag{B.2}$$

The particles have masses M_i with $i \in [1, 2, 3, 4]$.

B.1. Mandelstam Variables

Once the conventions in kinematics are fixed, a set of variables can be defined as

$$\begin{aligned} s &= (p_1 + p_2)^2 = (p_3 + p_4)^2, \\ t &= (p_1 - p_3)^2 = (p_2 - p_4)^2, \\ u &= (p_1 - p_4)^2 = (p_2 - p_3)^2. \end{aligned} \tag{B.3}$$

These are called Mandelstam variables. s is the total center of mass energy squared and t is the negative of the transferred four-momentum squared. The advantage of these variables is their Lorentz invariance. As the energy momentum relation (B.1) and the mass-shell condition (B.2) hold,

$$s + t + u = M_1^2 + M_2^2 + M_3^2 + M_4^2 \tag{B.4}$$

is true. To examine this further, two particle scattering is considered in the center of mass frame. The frame is defined by

$$\vec{p}_1 + \vec{p}_2 = 0 = \vec{p}_3 + \vec{p}_4. \tag{B.5}$$

Corresponding variables within this frame are marked with a star, e.g. $p_i = p_i^*$. Through equation (B.5) the center of mass variables are

$$\begin{aligned} \vec{p}_1{}^* &= -\vec{p}_2{}^* =: \vec{p}, \\ \vec{p}_3{}^* &= -\vec{p}_4{}^* =: \vec{p}\,', \\ p_{1,2}^* &= (E_{1,2}^*,\ \pm\vec{p}), \\ p_{3,4}^* &= (E_{3,4}^*,\ \pm\vec{p}\,'). \end{aligned} \tag{B.6}$$

It is useful to express energy and momentum in Lorentz invariant quantities, using (B.1) and the Mandelstam variables. So

$$E_{1,3}^* = \frac{1}{\sqrt{s}} \left(s + M_{1,3}^2 - M_{2,4}^2 \right), \tag{B.7}$$

$$\vec{p}^{\,2} = \frac{1}{4s} \left(s^2 - 2s \left(M_1^2 + M_2^2 \right) + \left(M_1^2 - M_2^2 \right)^2 \right). \tag{B.8}$$

The scattering angle θ is obtained by inserting

$$\vec{p} \cdot \vec{p}\,' = |\vec{p}||\vec{p}\,'| \cos\theta \tag{B.9}$$

to

$$p_1^* p_3^* = E_1^* E_3^* - |\vec{p}_1{}^*||\vec{p}_3{}^*| \cos\theta \tag{B.10}$$

and using the definition of the Mandelstam variables. The outcome is

$$cos\theta = \left(s(t-u) + (M_1^2 - M_2^2)(M_3^2 - M_4^2)\right)\left(s^2 - 2s(M_1^2 + M_2^2(+(M_1^2 - M_2^2)\right)^{-1/2} \left(s^2 - 2s(M_3^2 + M_4^2) + (M_3^2 - M_4^2)^2\right)^{-1/2}. \tag{B.11}$$

This leaves two independent variables to describe a two body process:

$$s \text{ and } \theta \qquad \text{or} \qquad s \text{ and } t$$

B.2. Elastic Scattering Cross Sections and Direct Detection Cross Sections

Regarding elastic scattering, which is important in direct detection, the results from the previous section can be simplified. Elastic scattering implies

$$\begin{aligned} M_1 &= M_3, \\ M_2 &= M_4 \end{aligned} \tag{B.12}$$

as the initial and final state particles are the same. This constraint leads to

$$E_1^* = E_3^*, \tag{B.13}$$

$$E_2^* = E_4^*, \tag{B.14}$$

$$|\vec{p}|^2 = |\vec{p}\prime|^2 = \frac{1}{4s}\left(s - (M_1 + M_2)^2\right)\left(s - (M_1 - M_2)^2\right). \tag{B.15}$$

Thus the expression for the scattering angle θ simplifies to

$$\cos\theta = 1 + \frac{t}{2|\vec{p}|^2}. \tag{B.16}$$

For a lot of processes, the relative velocity v_{rel} between two interacting particles is important. It can be written as

$$\begin{aligned} v_{\text{rel}} = |\vec{v}_1 - \vec{v}_2| &= |\frac{\vec{p}_1}{E_1} - \frac{\vec{p}_2}{E_2} \\ &= |\frac{\vec{p}_1{}^*}{E_1^*} - \frac{\vec{p}_2{}^*}{E_2^*}| \\ &= \frac{|\vec{p}_1{}^*|}{E_1^* E_2^*}\sqrt{s}, \end{aligned} \tag{B.17}$$

where $E_1^* + E_2^* = \sqrt{s}$ is used.

So

$$\begin{aligned} v_{\text{rel}} E_1^* E_2^* =& |\vec{p}_1{}^*| \sqrt{s} \\ \overset{(B.1)}{=}& \sqrt{s} \sqrt{E_1^* - M_1^2} \\ \overset{(B.3),(B.2)}{=}& \sqrt{(p_1^* p_2^*)^2 - M_1^2 M_2^2}. \end{aligned} \tag{B.18}$$

is true. This factor is independent of the frame. In case of annihilation, where the incoming particles are identical,

$$E_1^* = E_2^* \qquad \text{and} \qquad E_1^{*2} = \frac{1}{4} s \tag{B.19}$$

holds. Thus

$$v_{\text{rel}} E_1^* E_2^* = |\vec{p}^*| \sqrt{s} = \frac{1}{2} \sqrt{s(s - 4M_1^2)}. \tag{B.20}$$

For $2 \to 2$ processes with identical final state particles, the cross section is given by

$$\begin{aligned} \mathrm{d}\sigma =& \frac{1}{E_1 E_2} \frac{1}{|v_{rel}|} \frac{\mathrm{d}\Omega}{8\pi} |\overline{F}|^2 \frac{2|\vec{p}_{\text{fin}}|}{\sqrt{s}} \frac{1}{4\pi} \\ \overset{(B.20)}{=}& \frac{1}{s} \frac{\mathrm{d}\Omega}{8\pi} |\overline{F}|^2 \frac{1}{4\pi} \left(1 - \frac{4M_{\text{fin}}^2}{s}\right)^{1/2} . \end{aligned} \tag{B.21}$$

where $\vec{p}_{\text{fin}}$ is the momentum of one final state particle with mass M_{fin} and energy E_{fin} in the center of mass frame and $|\overline{F}|^2$ is the spin averaged squared matrix element describing the process. If the scattering amplitude $|\overline{F}|^2$ depends on t, the integration has to be done explicitly, but it can be simplified by using equation (B.16). Otherwise, the integration over the solid angle yields a factor of 4π.

Direct detection can be treated as elastic dark matter-quark scattering at zero momentum transfer, hence s goes to zero. The general cross section in this case is given by

$$\mathrm{d}\sigma |v_{\text{rel}}| = \frac{1}{s} \frac{\mathrm{d}\Omega}{8\pi} |\overline{F}|^2 \frac{1}{4\pi} \left(1 - \frac{4M_{\text{fin}}^2}{s}\right)^{1/2} \tag{B.22}$$

where $|\overline{F}|^2$ is the scattering amplitude for dark matter off quarks. To obtain the spin independent direct detection cross section, the form factors $f_{p,n}$ account for the distribution of quarks in the nucleons. In the case of a t-independent scattering amplitude,

the cross section is

$$\sigma_{n,p}^{\mathrm{SI}} = \frac{|\overline{M}|^2}{32\pi} \frac{f_{n,p}^2}{(M_S + M_{n,p})^2}. \tag{B.23}$$

C. Feynman Rules

C.1. Singlet Fermionic Dark Matter - Feynman Rules

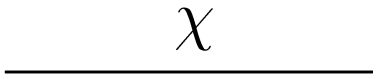

External fermions: u incoming, $\overline{u}$ outgoing
External antifermions: v incoming, $\overline{v}$ outgoing

External gauge boson: ϵ_μ^α

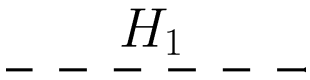

H_1 propagator: $\frac{i}{s-M_{H_1}^2}$

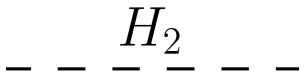

H_2 propagator: $\frac{i}{s-M_{H_2}^2}$

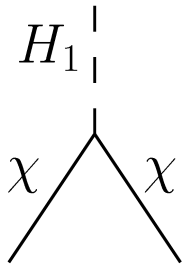

$i \cdot \sin\alpha \, (g_s + i g_p \gamma_5)$

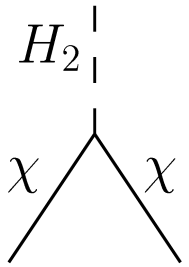

$i \cdot \cos\alpha \, (g_s + i g_p \gamma_5)$

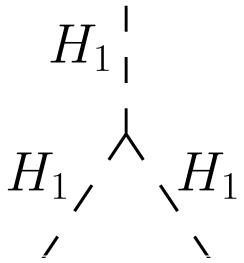

$-i \cdot (6\cos^3\alpha\lambda_H v - 3\cos^2\alpha\sin\alpha\mu$
$+3\cos\alpha\sin^3\alpha\lambda_4 v - 2\sin^3\alpha\mu_3)$

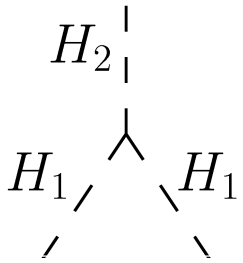

$-i\cdot(\cos^3\alpha\mu + 2\cos^2\alpha\sin\alpha(3\lambda_H - \lambda_4)v$
$+2\cos\alpha\sin^2\alpha\,(\mu_3 - \mu) + \sin^3\alpha\lambda_4 v)$

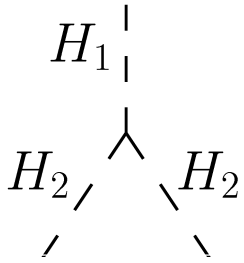

$-i\cdot(\cos^3\alpha\lambda_4 v + 2\cos^2\alpha\sin\alpha\,(-\mu_3 + \mu)$
$+2\cos\alpha\sin^2\alpha\,(3\lambda_H - lv)\,v - \sin^3\alpha\mu)$

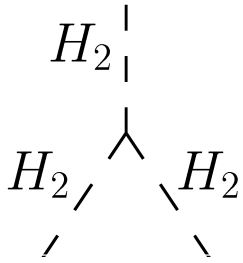

$-i\cdot\big(\cos^3\alpha\mu_3 + 3\cos^2\alpha\sin\alpha\lambda_4 v + 3\cos\alpha\sin^2\alpha\mu$
$+8\sin^3\alpha\lambda_H v)$

C.2. Two-Component Dark Matter - Feynman Rules

In the two-component dark matter model, all Feynman rules from the previous section apply. Additionally new vertices appear, which are listed here.

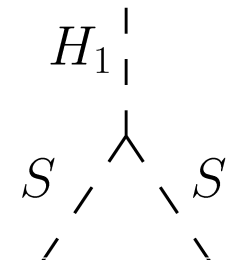

$-i \cdot \left(\frac{1}{2}\cos\alpha\lambda_{HSS} v - \sin\alpha\lambda\right)$

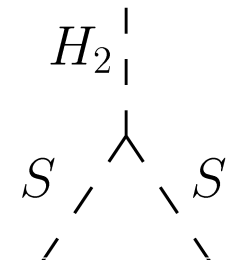

$-i \cdot \left(\frac{1}{2}\sin\alpha\lambda_{HSS} v + \cos\alpha\lambda\right)$

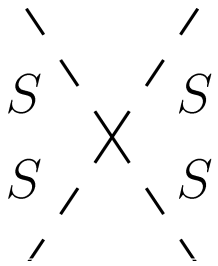

$-i \cdot 6\lambda_S$

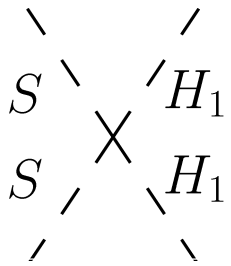

$-\frac{i}{2} \cdot \left(\cos^2\alpha\lambda_{HSS} + 4\sin^2\alpha\lambda_{\phi\phi SS}\right)$

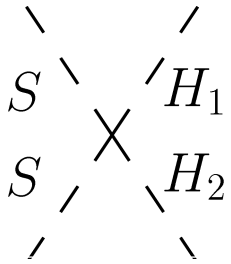

$-\frac{i}{2}\cos\alpha\sin\alpha \cdot (\lambda_{HSS} - 4\lambda_{\phi\phi SS})$

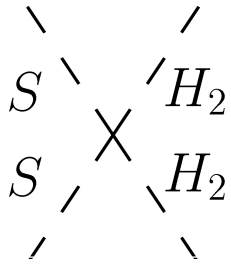

$-\frac{i}{2} \cdot \left(\lambda_{HSS}\sin^2\alpha + 4\cos^2\alpha\lambda_{\phi\phi SS}\right)$

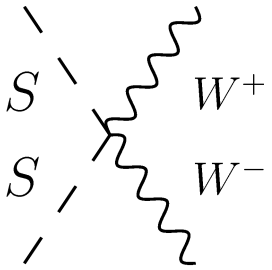

$-\frac{1}{2}i\lambda_{HSS}$

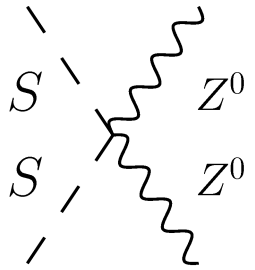

$-\frac{1}{2}i\lambda_{HSS}$

D. Thermal Average

This section shows a short sketch on thermally averaged cross sections times velocity. It is based on the work by Gelmini and Gondolo [40]. Consider a particle species with equilibrium density distribution $f(E)$ for energy E. At a given temperature T the distribution f(E) follows a Maxwell-Boltzmann distribution, it is proportional to $\exp^{-E/T}$. Thus the thermally averaged cross section times velocity is

$$\langle \sigma v \rangle = \frac{\int \sigma v \; e^{-E_1/T} \; e^{-E_2/T} \; d^3p_1 \; d^3p_2}{\int e^{-E_1/T} \; e^{-E_2/T} \; d^3p_1 \; d^3p_2}. \tag{D.1}$$

v is the velocity between two incoming particles, $\vec{p}_{1,2}$ are the three-momenta and $E_{1,2}$ the corresponding particle energies.
The relativistic energy-momentum relation (B.1) allows to transform the volume element in momentum space,

$$\mathrm{d}^3p_1\mathrm{d}^3p_2 = 4\pi p_1 \mathrm{d}E_1 \; 4\pi p_2 \mathrm{d}E_2 \; \frac{1}{2}\mathrm{d}\cos\theta. \tag{D.2}$$

θ is the angle between $\vec{p}_1$ and $\vec{p}_2$, and $\mathrm{p}_{1,2} = |\vec{p}_{1,2}|$. Introducing the new variables

$$\begin{aligned} E_+ &= E_1 + E_2, \\ E_- &= E_1 - E_2, \\ s &= 2m^2 + 2E_1E_2 - 2p_1p_2\cos\theta \end{aligned} \tag{D.3}$$

transforms the volume element to

$$d^3p_1 d^3p_2 = 2\pi^2 E_1 E_2 \mathrm{d}E_+ \mathrm{d}E_- ds. \tag{D.4}$$

The previous limits $E_{1,2} > m$ and $|\cos\theta| \leq 1$ translate to

$$E_+ \geq \sqrt{s} =: E_{+,\min}, \tag{D.5}$$

$$s \geq 4m^2, \tag{D.6}$$

$$|E_-| \leq \sqrt{1 - \frac{4m^2}{s}}\sqrt{E_+^2 - s} =: E_{-,\max}. \tag{D.7}$$

These transformation of integration variables is applied to the the numerator of (D.1):

$$\begin{aligned}\int \sigma v e^{-E_1/T} e^{-E_2/T} \mathrm{d}^3p_1 \mathrm{d}^3p_2 =& 2\pi^2 \int_{4m^2}^{\infty} \int_{E_{+,\min}}^{\infty} \int_{-E_{-,\max}}^{+E_{-,\max}} \sigma v E_1 E_2 e^{-E+/T} \mathrm{d}E_- \mathrm{d}E_+ \mathrm{d}s \\ =& 4\pi^2 \int_{4m^2}^{\infty} \int_{E_{+,\min}}^{\infty} \sigma v E_1 E_2 \sqrt{1-\frac{4m^2}{s}} \sqrt{E_+^2 - s} e^{-E_+/T} \mathrm{d}E_+ \mathrm{d}s \\ \overset{(B.20)}{=}& 2\pi^2 T \int_{4m^2}^{\infty} \sigma (s-4m^2) \sqrt{s} K_1(\frac{\sqrt{s}}{T}) ds, \end{aligned} \tag{D.8}$$

in the last step, the properties of s were used and the integration over E_+ is carried out as σ depends on s only. K_1 is the second kind of modified Bessel function of order one. The denominator is treated similarly:

$$\begin{aligned}\int e^{-E_1/T} e^{-E_2/T} =& 2\pi^2 \int_{4m^2}^{\infty} \int_{E_{+,\min}}^{\infty} \int_{-E_{-,\max}}^{+E_{-,\max}} E_1 E_2 e^{-E+/T} \mathrm{d}E_- \mathrm{d}E_+ \mathrm{d}s \\ =& 4\pi^2 \int_{4m^2}^{\infty} \int_{E_{+,\min}}^{\infty} E_1 E_2 \sqrt{1-\frac{4m^2}{s}} \sqrt{E_+^2 - s} e^{-E_+/T} \mathrm{d}E_+ \mathrm{d}s \\ =& 2\pi^2 \int_{4m^2}^{\infty} \sqrt{1-\frac{4m^2}{s}} \sqrt{s} E_1 E_2 K_1(\frac{\sqrt{s}}{T}) \mathrm{d}s \\ =& \left(4\pi m^2 T K_2(\frac{m}{T})\right)^2 \end{aligned} \tag{D.9}$$

with the modified Bessel function K_2 of second kind of the order 2. Combining equation (D.8) and (D.9) the thermally averaged cross section times velocity is

$$\langle \sigma v \rangle = \frac{1}{8m^4 T K_2^2(\frac{m}{T})} \int_{4m^2}^{\infty} \sigma (s-4m^2) \sqrt{s} K_1(\frac{s}{T}) \mathrm{d}s. \tag{D.10}$$

The next part is based on [51]. It is important for the handling of the two Boltzmann equations in H, as the thermally averaged cross section for the process $AB \to CD$ can be linked to the process $CD \to AB$. The cross section can be written as

$$\begin{aligned}\sigma_v^{ABCD} =& \frac{T}{64\pi^2 s^2 Y_{A,\mathrm{eq}}(T) Y_{B,\mathrm{eq}}(T)} \int \frac{\mathrm{d}s}{\sqrt{s}} K_1\left(\frac{\sqrt{s}}{T}\right) p_{\mathrm{in}} p_{\mathrm{out}} \\ & \sum_{\substack{a\in A \; b\in B \\ c\in C \; d\in D}} \int_{-1}^{1} |\mathcal{M}_{ab\to cd}(\sqrt{s}, \cos\theta)|^2 \mathrm{d}\cos\theta, \end{aligned} \tag{D.11}$$

where $\mathcal{M}_{ab\to cd}$ is the 2 to 2 matrix element. The equilibrium value is given by

$$Y_{A,\mathrm{eq}} = \frac{T}{2\pi^2 s} \sum_{a\in A} g_a M_a^2 K_2 \left(\frac{M_a}{T}\right). \tag{D.12}$$

In this equation g_a is the coupling, M_a the mass of particle a which is of type A. As the process $AB \to CD$ is described by the same matrix element as $CD \to AB$, the relation

$$Y_{A,\mathrm{eq}} Y_{B,\mathrm{eq}} \sigma_v^{ABCD} = Y_{C,\mathrm{eq}} Y_{D,\mathrm{eq}} \sigma_v^{CDAB} \tag{D.13}$$

is true. It is used in equations (4.5) and (4.6) to simplify the expressions.

E. Scalar potential in the fermionic singlet model

The scalar potential in the fermionic singlet model in section 3 is

$$\begin{aligned} -V(\phi, H) = &- \mu_H^2 H^\dagger H + \lambda_H (H^\dagger H)^2 + \mu \phi H^\dagger H + \frac{\lambda_4}{2} \phi^2 H^\dagger H \\ &+ \mu_1^3 \phi - \frac{\mu_\phi^2}{2} \phi^2 + \frac{\mu_3}{3} \phi^3 + \frac{\lambda_\phi}{4} \phi^4. \end{aligned} \tag{E.1}$$

It includes the Standard Model Higgs doublet H and the scalar mediator ϕ.

Actuating the minimum of this potential yields the vacuum expectation values $\langle H \rangle = 246$ GeV and $\langle \phi \rangle$. Without loss of generality, it is possible to find a basis in which ϕ has a vanishing vacuum expectation value.
The minimum is determined by

$$\frac{\partial V}{\partial x_i}|_{x_i = \langle x_i \rangle} = 0; \tag{E.2}$$

where x_i stands for the arguments of V and their conjugates. Taking all derivatives leads to the expressions

$$\frac{\partial V}{\partial \phi} = -\mu_\phi^2 \phi + \lambda_\phi \phi^3 + \lambda_\phi \phi H^\dagger H + \mu_1^3 + \mu_3 \phi^2 + \mu H^\dagger H, \tag{E.3}$$

$$\frac{\partial V}{\partial H^\dagger} = -\mu_H^2 H + 2\lambda_H H \left(H^\dagger H\right) + \frac{\lambda_\phi}{2} \phi^2 H + \mu \ \phi H, \tag{E.4}$$

$$\frac{\partial V}{\partial H} = -\mu_H^2 H^\dagger + 2\lambda_H H^\dagger \left(H^\dagger H\right) + \frac{\lambda_\phi}{2} \phi^2 H^\dagger + \mu \ \phi H^\dagger. \tag{E.5}$$

At the minimum, the expressions

$$\mu_1^3 + \frac{1}{2} \mu v^2 = 0, \tag{E.6}$$

$$-\mu_H^2 + \lambda_H v^2 = 0 \tag{E.7}$$

are obtained. An expansion around the vacuum expectation values for H in unitary

gauge is

$$H = \frac{1}{\sqrt{2}} \begin{pmatrix} 0 \\ h + v \end{pmatrix}. \tag{E.8}$$

It expands the potential to

$$\begin{aligned} V(\phi, h) =& (-\mu_H^2 v + \lambda_H v^3)h + (-\frac{\mu_H^2}{2} + \frac{3\lambda_H v^2}{2})h^2 + \lambda_H v h^3 + \frac{\lambda_H}{4}h^4 \\ &+ (\mu_1^3 + \frac{\mu v^2}{2})\phi + (-\frac{\mu_\varphi^2}{2} + \frac{\lambda_4 v^2}{4})\phi^2 + \frac{\mu_3}{3}\phi^3 + \frac{\lambda_\varphi}{4}\phi^4 \\ &+ \mu v \phi h + \frac{\lambda_4 v}{2}\phi^2 h + \frac{\mu}{2}\,\phi h^2 + \frac{lv}{4}\phi^2 h^2. \end{aligned} \tag{E.9}$$

The mass terms are identified by

$$M_{x_i}^2 = \frac{\partial V}{\partial x_i^2} \tag{E.10}$$

which yields

$$M_h^2 = -\mu_H^2 + 3\lambda_H v^2, \tag{E.11}$$

$$M_\phi^2 = -\mu_\varphi^2 + \frac{\lambda_4 v^2}{2} \tag{E.12}$$

With respect to equations (E.6) to (E.12), further information about parameters of this model is gained:

$$\mu_1^3 = \frac{-\mu v^2}{2}, \tag{E.13}$$

$$\mu_H^2 = \frac{M_h^2}{2}, \tag{E.14}$$

$$\lambda_H = \frac{M_h^2}{2v^2}, \tag{E.15}$$

$$\mu_\varphi^2 = \frac{\lambda_4 v^2}{2} - M_\phi^2. \tag{E.16}$$

The terms involving the two interaction eigenstates ϕ and h are

$$\begin{pmatrix} \varphi & h \end{pmatrix} \mathbb{A} \begin{pmatrix} \phi \\ h \end{pmatrix} \tag{E.17}$$

where

$$\mathbb{A} = \begin{pmatrix} \frac{1}{2}M_\phi^2 & \frac{1}{2}\mu v \\ \frac{1}{2}\mu v & \frac{1}{2}M_h^2 \end{pmatrix}. \tag{E.18}$$

A transformation to diagonalize $\mathbb{A}$ is performed:

$$\mathbb{D} = \mathbb{U}^{-1}\mathbb{A}\mathbb{U} \tag{E.19}$$

with

$$\mathbb{U} = \begin{pmatrix} \cos\alpha & -\sin\alpha \\ \sin\alpha & \cos\alpha \end{pmatrix}. \tag{E.20}$$

This corresponds to a basis transformation from interaction eigenstate basis (ϕ, h) to mass eigenstate basis (H_1, H_2).

$$\begin{pmatrix} H_2 \\ H_1 \end{pmatrix} = \mathbb{U}^{-1} \begin{pmatrix} \varphi \\ h \end{pmatrix} \tag{E.21}$$

which is equal to

$$\phi = -\sin\alpha H_1 + \cos\alpha H_2, \tag{E.22}$$
$$h = \cos\alpha H_1 + \sin\alpha H_2. \tag{E.23}$$

The back transformation gives the result from equation (3.3) from section 3.

In consequence, the relations between the masses for the different states are

$$M_h^2 = M_{H_1}^2 \cos^2\alpha + M_{H_2}^2 \sin^2\alpha, \tag{E.24}$$
$$M_\phi^2 = M_{H_1}^2 \sin^2\alpha + M_{H_2}^2 \cos^2\alpha. \tag{E.25}$$

This provides also an expression for μ

$$\mu v = (M_{H_2}^2 - M_{H_1}^2)\sin\alpha\cos\alpha. \tag{E.26}$$

Hence the free parameters of the model which are chosen for its analysis can be linked to the parameters in the potential.

F. Direct Detection Cross Section for the Fermion

The direct detection of the fermion χ takes places via t-channel exchange of the two scalars H_1 and H_2 as it is shown in figure F.1. The derivation of the corresponding cross section is shown in short steps in the following.

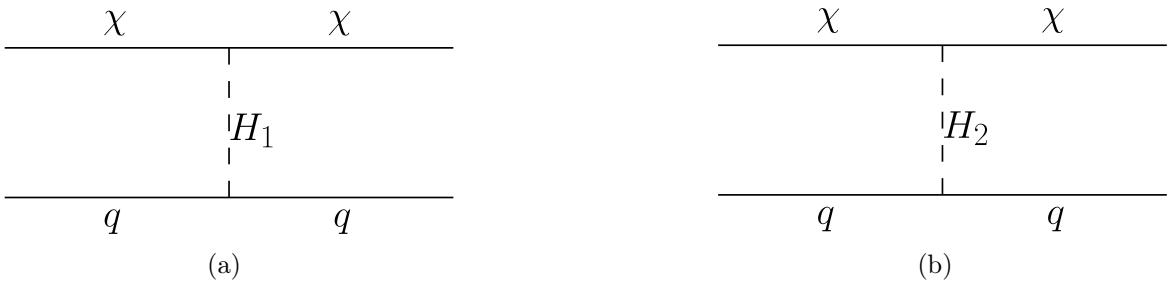

Figure F.1.: Feynman diagrams providing spin-independent elastic scattering of dark matter particles off nuclei.

The scattering amplitude for the fermion-quark interaction is

$$F = i \sin\alpha \cos\alpha \left(\frac{1}{M_{H_1}^2} - \frac{1}{M_{H_2}^2} \right) \overline{u}(p_3, s_3) \left(g_s + i g_p \gamma_5 \right) u(p_1, s_1) \overline{u}(p_4, s_4) u(p_2, s_2) \quad \text{(F.1)}$$

where the fermion is assigned with momentum $p_1 = p_3$ and spin $s_1 = s_3$, the quark momentum is equal to $p_2 = p_4$ and the quark spin is $s_2 = s_4$ and the quark mass is M_q.

The average and sum over spins in the squared amplitude reads as follows:

$$\begin{aligned}
|\overline{F}|^2 =& K \left(\sum_{s_3} \overline{u}(p_3, s_3)(g_s + i g_p \gamma_5) \left(\sum_{s_1} u(p_1, s_1)\overline{u}(p_1, s_1) \right) (g_s + i g_p \gamma_5) u(p_3, s_3) \right) \\
& \left(\sum_{s_2, s_4} \overline{u}(p_4, s_4) u(p_2, s_2) \overline{u}(p_2, s_2) u(p_4, s_4) \right) \\
\overset{*}{=}& K Tr\left((\not{p}_1 + M_\chi)(g_s + i g_p \gamma_5)(\not{p}_1 + M_\chi) \right) Tr\left((\not{p}_2 + M_q)(\not{p}_2 + M_q) \right) \\
\overset{**}{=}& \frac{16}{v^2} M_\chi^2 M_q^2 g_s^2 \sin^2 2\alpha g_s^2 \left(\frac{1}{M_{H_1}^2} - \frac{1}{M_{H_2}^2} \right)^2
\end{aligned} \tag{F.2}$$

* denotes that the completeness relation (A.2), $p_1 = p_3$ and $p_2 = p_4$ are used. The abbreviation K is introduced as

$$K := \sin^2 \alpha \cos^2 \alpha \frac{M_q^2}{v^2} \left(\frac{1}{M_{H_1}^2} - \frac{1}{M_{H_2}^2} \right)^2. \tag{F.3}$$

Plugging the amplitude into the general direct detection cross section B.22 yields

$$\sigma_{\mathrm{SI}} = \frac{g_s^2 \sin^2 2\alpha}{4\pi} M_r^2 \left(\frac{1}{M_{H_1}^2} - \frac{1}{M_{H_2}^2} \right)^2 g_{\mathrm{HP}}^2, \tag{F.4}$$

where M_r is the reduced mass of the dark matter proton system and

$$g_{\mathrm{HP}} = \frac{M_p}{v} \left[\sum_{q=u,d,s} f_q^p + \frac{2}{9} \left(1 - \sum_{q=u,d,s} f_q^p \right) \right] \approx 10^{-3}, \tag{F.5}$$

where M_p is the proton mass.

G. Calculations for the Scalar S in the Two-Component Dark Matter Model

G.1. Annihilation Cross Sections

Process : $SS \to \mathbf{f}\overline{f}$

:

The two diagrams shown in figure G.1 contribute to the scalar S annihilating to fermions of the mass M_f.

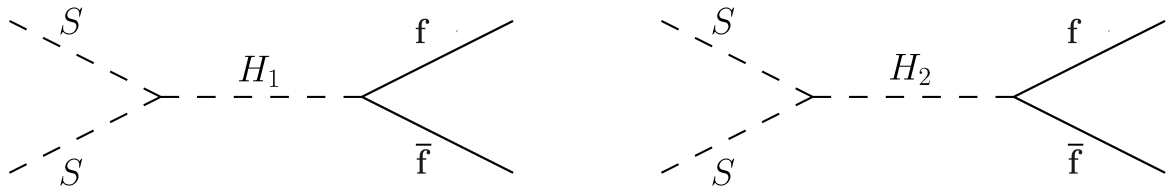

Figure G.1.: Feynman diagram for $SS \to f\overline{f}$.

The scattering amplitude is given by the matrix element

$$\begin{aligned} F = &- i \left(\frac{M_f}{v} \cos\alpha (\frac{1}{2} \cos\alpha \lambda_{HSS} v - \sin\alpha \lambda) \frac{1}{s - M_{H_1}^2} \right. \\ &\left. + \frac{M_f}{v} \sin\alpha (\frac{1}{2} \sin\alpha \lambda_{HSS} v + \cos\alpha \lambda) \frac{1}{s - M_{H_2}^2} \right) \bar{u}(p_3) v(p_4) \end{aligned} \tag{G.1}$$

according to the Feynman rules in the two-component dark matter model. The squared

matrix element is

$$|F|^2 = \frac{M_f^2}{v^2}\left(\frac{a}{s-M_{H_1}^2}+\frac{b}{s-M_{H_2}^2}\right)^2 \bar{u}(p_3)v(p_4)\bar{v}(p_4)u(p_3) \tag{G.2}$$

with

$$a := \cos\alpha(\frac{1}{2}\cos\alpha\lambda_{HSS}v - \sin\alpha\lambda), \tag{G.3}$$

$$b := \sin\alpha(\frac{1}{2}\sin\alpha\lambda_{HSS}v + \cos\alpha\lambda). \tag{G.4}$$

Carrying out the average over initial spins and the sum over final spins leads to

$$|\overline{F}|^2 = KN_C Tr((\not{p}_3 + M_f)(\not{p}_4 - M_f)) \tag{G.5}$$

$$= KN_C 2s\left(1-\frac{4M_f^2}{s}\right) \tag{G.6}$$

with the abbreviation

$$K := \frac{M_f^2}{v^2}\left(\frac{a}{s-M_{H_1}^2}+\frac{b}{s-M_{H_2}^2}\right)^2. \tag{G.7}$$

and the symmetry factor N_C taking into account the color of the final state, N_C is 1 for leptons and 3 for quarks. The second line is obtained when applying the completeness relation (A.2) and the last line results when trace theorems (A.16) are applied. The differential cross section, according to (B.21, is

$$\mathrm{d}\sigma_{SS\to f\bar{f}}|v_{rel}| = \frac{\mathrm{d}\Omega}{16\pi^2}N_C K\left(1-\frac{4M_f^2}{s}\right)^{3/2}, \tag{G.8}$$

where the integration can be taken out:

$$\sigma_{SS\to f\bar{f}}|v_{rel}| = \frac{1}{4\pi}N_C K\left(1-\frac{4M_f^2}{s}\right)^{3/2}. \tag{G.9}$$

Process: $SS \to V\bar{V}$

Vector boson production from S annihilation takes place in a similar way as fermion production. It is either mediated by H_1 and H_2 or takes place directly, as shown in figure G.2.

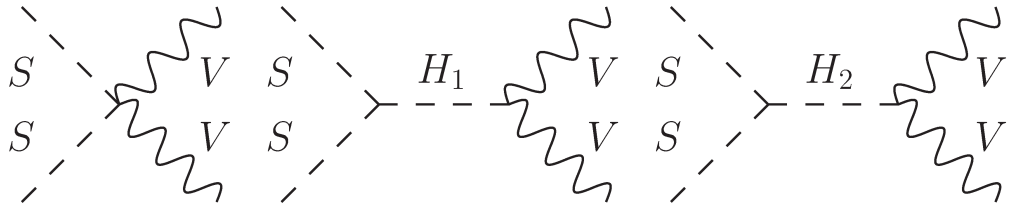

Figure G.2.: Feynman diagrams for $SS \to V\overline{V}$.

The corresponding amplitude is

$$F = -i\epsilon_\mu^\alpha \epsilon_\nu^\beta \left(\frac{2M_V^2}{v} \left(\frac{a}{s - M_{H_1}^2} + \frac{b}{s - M_{H_2}^2} \right) + \frac{\lambda_{HSS}}{2} \right) \tag{G.10}$$

where M_V is the vector boson mass, ϵ is a polarization vector and a as well as b are the same as before. These two factors originate from the coupling of the scalar to the two Higgs bosons. Averaging over initial spins and summing over final spins in the squared amplitude leads to

$$|\overline{F}|^2 = N_V \sum_{spins} \left(\epsilon_\mu^\alpha \epsilon_\nu^\beta g^{\mu\nu} \right)^2 \left(\frac{2M_V^2}{v} \left(\frac{a}{s - M_{H_1}^2} + \frac{b}{s - M_{H_2}^2} \right) + \frac{\lambda_{HSS}}{2} \right)^2 \tag{G.11}$$

$$\overset{(G.14)(G.16)}{=} C \left(2 + \frac{(p_3 p_4)^2}{M_V^4} \right) \tag{G.12}$$

$$= C \frac{s}{4M_V^4} \left(1 - \frac{4M_V^2}{s} + \frac{8M_V^4}{s^2}) \right) \tag{G.13}$$

where N_V is the symmetry factor, which is 1 for W bosons and 1/2 for Z bosons, as they are their own antiparticle, and the abbreviation

$$C := N_V \left(\frac{2M_V^2}{v} \left(\frac{a}{s - M_{H_1}^2} + \frac{b}{s - M_{H_2}^2} \right) + \frac{\lambda_{HSS}}{2} \right)^2 \tag{G.14}$$

and the identity

$$\sum_{spins} (\epsilon_\mu^\alpha \epsilon_\nu^\beta g^{\mu\nu})^2 = (g^{\mu\nu)} + \frac{p_3^\mu p_3^\nu}{M_V^2})(g_{\mu\nu]} + \frac{p_{4\nu} p_{4\mu}}{M_V^2}) \tag{G.15}$$

$$= 2 + \frac{(p_3 p_4)^2}{M_V^4} \tag{G.16}$$

are used in the steps according to the labels above the equal signs. The last line in (G.13) is obtained while using the equations for the Mandelstam variables in the center

of mass frame. Accordingly the cross section is

$$\sigma v_{rel} = \frac{C}{32\pi M_V^4}\left(1-\frac{4{M_V}^2}{s}\right)^{1/2}\left(1-\frac{4M_V^2}{s}+\frac{8M_V^4}{s^2})\right) \tag{G.17}$$

as the integration over the solid angle just gives 4π.

Process: $SS \to HH$

The annihilation $SS \to H_{1,2}H_{1,2}$ is mediated by the five diagrams shown in figure G.3.

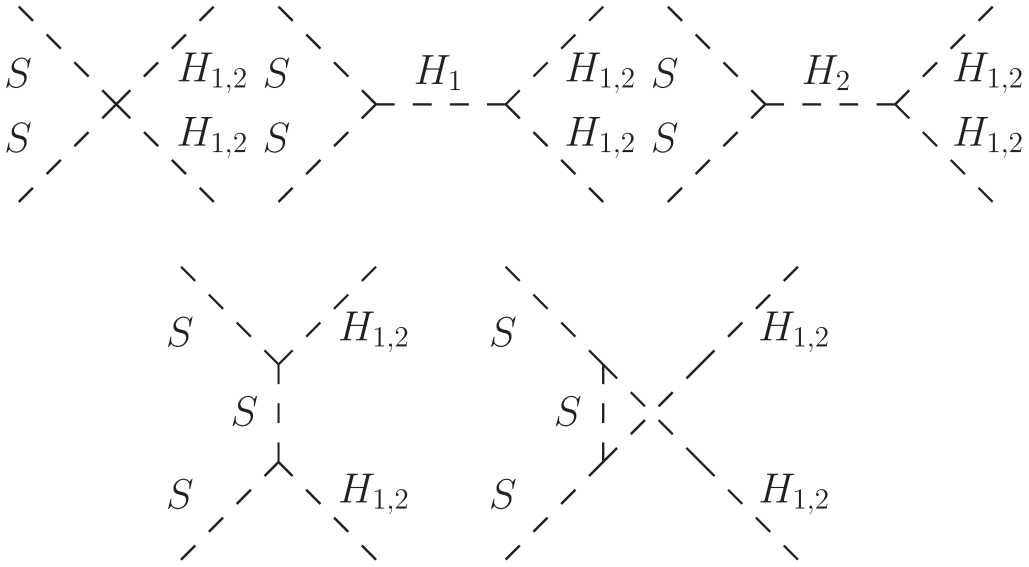

Figure G.3.: Feynman diagrams for the process $SS \to H_{1,2}H_{1,2}$.

The corresponding amplitude for either $SS \to H_1H_1$ and $SS \to H_2H_2$ is given by

$$F = \frac{-i}{2}\left(a-\frac{b}{s-M_{H_{1,2}^2}}-\frac{c}{s-M_{H_{1,2}}^2}+d\left(\frac{1}{t-M_S^2}-\frac{1}{u-M_S^2}\right)\right) \tag{G.18}$$

where the coefficients for the process $SS \to H_1H_1$ are

$$\begin{aligned}
a =& \cos^2\alpha\lambda_{HSS} + 4\sin^2\alpha\lambda_{\phi\phi SS},\\
b =& (\cos\alpha\lambda_{HSS}v - 2\sin\alpha\lambda)\\
&\left(6\cos^3\alpha\lambda_H v - 3\cos^2\alpha\sin\alpha\mu + 3\cos\alpha\sin^3\alpha\lambda_4 v - 2\sin^3\alpha\mu_3\right),\\
c =& (\sin\alpha\lambda_{HSS}v + 2\cos\alpha\lambda_{\phi SS})\\
&\left(\cos^3\alpha\mu + 2\cos^2\alpha\sin\alpha(3\lambda_H - \lambda_4)v + 2\cos\alpha\sin^2\alpha\,(\mu_3 - \mu) + \sin^3\alpha\lambda_4 v\right),\\
d =& (\cos\alpha\lambda_{HSS}v - 2\sin\alpha\lambda)^2,
\end{aligned}$$

and or $SS \to H_2H_2$ the coefficients are

$$\begin{aligned}
a_2 =& \cos\alpha\sin\alpha\cdot(\lambda_{HSS} - 4\lambda_{\phi\phi SS}),\\
b_2 =& (\cos\alpha\lambda_{HSS}v - 2\sin\alpha\lambda)\\
&\left(\cos^3\alpha\lambda_4 v + 2\cos^2\alpha\sin\alpha\,(-\mu_3 + \mu) + 2\cos\alpha\sin^2\alpha\,(3\lambda_H - lv)\,v - \sin^3\alpha\mu\right),\\
c_2 =& (\sin\alpha\lambda_{HSS}v + 2\cos\alpha\lambda_{\phi SS})\\
&\left(\cos^3\alpha\mu_3 + 3\cos^2\alpha\sin\alpha\lambda_4 v + 3\cos\alpha\sin^2\alpha\mu + 8\sin^3\alpha\lambda_H v\right),\\
d_2 =& (\sin\alpha\lambda_{HSS}v + 2\cos\alpha\lambda_{\phi SS})^2.
\end{aligned}$$

As there are no spins involved, the averaged squared amplitude is directly introduced to the cross section formula (B.21):

$$\begin{aligned}
\mathrm{d}\sigma v_{rel} =& \frac{1}{s}\frac{1}{32\pi}\left(1 - \frac{4M_{H_{1,2}}^2}{s}\right)^{1/2}\frac{1}{4}\cdot\\
&\left(a - \frac{b}{s - M_{H_{1,2}^2}} - \frac{c}{s - M_{H_{1,2}}^2} + d\left(\frac{1}{t - M_S^2} - \frac{1}{u - M_S^2}\right)\right)^2 \mathrm{d}\Omega
\end{aligned} \tag{G.19}$$

In order to integrate the differential cross section, first all parts independent of t and u are treated, then the integration over the t and u dependent parts is done, which has a vanishing result.

$$\begin{aligned}
\sigma v_{rel} =& \frac{1}{64\pi s}\left(1 - \frac{4M_{H_{1,2}}^2}{s}\right)^2\left(a - \frac{b}{s - M_{H_{1,2}^2}} - \frac{c}{s - M_{H_{1,2}}^2}\right)^2 +\\
&\frac{1}{64\pi s^{\frac{3}{2}}}\left(1 - \frac{4M_{H_{1,2}}^2}{s}\right)^{\frac{3}{2}}\left(\int\left(d^2 f^2(t) + \left(\frac{2db}{s - M_{H_1}^2} + \frac{2cd}{s - M_{H_2}^2}\right)f(t)\right)dt\right)\\
=& \frac{1}{64\pi s}\left(1 - \frac{4M_{H_{1,2}}^2}{s}\right)^2\left(a - \frac{b}{s - M_{H_{1,2}^2}} - \frac{c}{s - M_{H_{1,2}}^2}\right)^2
\end{aligned} \tag{G.20}$$

With the abbreviation

$$f(t) := \left(\frac{1}{t - M_S^2} - \frac{1}{u - M_S^2} \right). \tag{G.21}$$

G.2. Direct Detection Cross Section

The direct detection cross section is obtained when calculating the elastic scattering of dark matter particles off quarks at zero momentum transfer. In the two-component model the scattering of the scalar S off nucleons takes place via a t-channel exchange of Higgs bosons H_1 and H_2. The corresponding diagrams are shown in figure G.4.

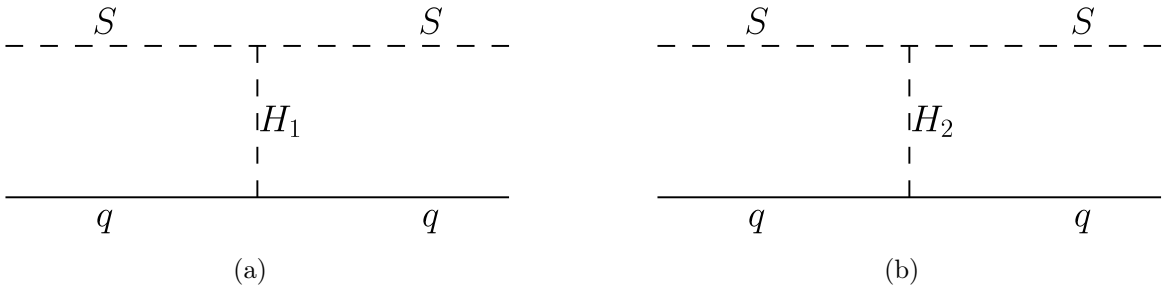

Figure G.4.: Feynman diagrams providing spin-independent elastic scattering of dark matter particles S off quarks.

Thus it is sufficient to take the spin averaged squared amplitude for the process $SS \to f\bar{f}$ (G.22) with $s = 0$, which then is

$$|\overline{F}|^2 = K_0 2s \left(1 - \frac{4M_f^2}{s} \right) \tag{G.22}$$

with the abbreviation

$$K_0 := \frac{M_f^2}{v^2} \left(\frac{a}{M_{H_1}^2} + \frac{b}{M_{H_2}^2} \right)^2. \tag{G.23}$$

Since this is independent of Mandelstam variable t, equation (B.23) can be applied and the resulting spin-independent cross section is

$$\begin{aligned} \sigma_{S,\mathrm{SI}} = \frac{M_r^2}{4\pi M_{H_1}^4 M_{H_2}^4 M_s^2} \Big(& \frac{v}{2} \lambda_{HSS} \left(\cos^2\alpha M_{H_2}^2 + \sin^2\alpha M_{H_1}^2 \right) \\ & + \lambda \cos\alpha \sin\alpha \left(M_{H_1}^2 - M_{H_2}^2 \right) \Big)^2 g_{HP}^2. \end{aligned} \tag{G.24}$$

where g_{HP} is the same as for the fermion.

H. Trapezoidal-Euler routine

In order to solve two coupled Boltzmann equations, an implicit Euler and trapezoidal routine with an adaptive step width is used. It is adapted from the DarkSUSY code [73] as described in the manual [74]. This section is loosely based on this description.
First a trapezoidal method is used, then the Euler discretization. The stepwidth is adapted according to the difference between the two discretization values. One starts with a set of two coupled Boltzmann equations, similar to (4.5) and (4.6):

$$\frac{\mathrm{d}Y_1}{\mathrm{d}x} = -a\left(b\left(Y_1^2 - Y_{1,\mathrm{eq}}^2\right) + c\left(Y_1^2 - Y_{1,\mathrm{eq}}^2\frac{Y_2^2}{Y_{2,\mathrm{eq}}^2}\right)\right), \tag{H.1}$$

$$\frac{\mathrm{d}Y_2}{\mathrm{d}x} = -a\left(d\left(Y_2^2 - Y_{2,\mathrm{eq}}^2\right) + e\left(Y_2^2 - Y_{2,\mathrm{eq}}^2\frac{Y_1^2}{Y_{1,\mathrm{eq}}^2}\right)\right). \tag{H.2}$$

The variables a, b, c, d and e contain all annihilation cross sections and prefactors which can depend on x. A simplified from is

$$\frac{\mathrm{d}Y_1}{\mathrm{d}x} = f_1(x), \tag{H.3}$$

$$\frac{\mathrm{d}Y_2}{\mathrm{d}x} = f_2(x) \tag{H.4}$$

with $\mathrm{f}_{1,2}$ presenting the right hand side of the coupled equations (H.1) and (H.2). In order to discretize the equation, one starts at a point x_i and goes to $x_{i+1} := x_i + h$ with the stepwidth h. For simplicity the notation $f_{i,1,2}$ is adapted for $f_{1,2}(x_i)$, analogous $a(x_i) =: a_i$ and so on.
To find $Y_{i+1,1,2}$ and describe the evolution of Y in x, first a trapezoidal method is used:

$$Y_{i+1,1} - Y_{i,1} = h\frac{f_{i+1,1} + f_{i,1}}{2}, \tag{H.5}$$

$$Y_{i+1,2} - Y_{i,2} = h\frac{f_{i+1,2} + f_{i,2}}{2}. \tag{H.6}$$

Inserting the corresponding expressions for $f_{i+1,1,2}$ and $f_{i,1,2}$ from (H.1) and (H.2) leads to two coupled quadratic expressions for $Y_{i+1,1}$ and $Y_{i+1,2}$. When the quadratic equations are solved, a result for $Y_{i+1,1,2}$ is obtained. It only depends on quantities from the step

i and the equilibrium values for x_{i+1}. So

$$\begin{aligned} Y_{i+1,1} &= F_1(x_i, Y_{i+1,1,\mathrm{eq}}, Y_{i+1,2,\mathrm{eq}}) \\ Y_{i+1,2} &= F_2(x_i, Y_{i+1,1,\mathrm{eq}}, Y_{i+1,2,\mathrm{eq}}) \end{aligned} \tag{H.7}$$

is obtained. If $F_{1,2}$ is not defined, or negative for a certain x_{i+1} the step width h is reduced to $\frac{h}{2}$ and the step is repeated.
In order to have a handle on the step width, equation (H.1) and (H.2) are also discretized according to an Euler method;

$$Y_{i+1,1} - Y_{i,1} = h f_{i+1,1}, \tag{H.8}$$

$$Y_{i+1,2} - Y_{i,2} = h f_{i+1,2}. \tag{H.9}$$

The expressions for $f_{1,2}$ are inserted, which leads to another set of quadratic equations. Their solution is

$$\begin{aligned} Y'_{i+1,1} &= G_1(x_i, Y_{i+1,1,\mathrm{eq}}, Y_{i+1,2,\mathrm{eq}}) \\ Y'_{i+1,2} &= G_2(x_i, Y_{i+1,1,\mathrm{eq}}, Y_{i+1,2,\mathrm{eq}}) \end{aligned} \tag{H.10}$$

If $G_{1,2}$ is not defined or if it is negative, the step is repeated with half of the stepwidth h. The two discretization results are used to evaluate, whether a step is valid or not. The difference d is defined as

$$d := \min\left(\left| \frac{Y_{i+1,1} - Y'_{i+1,1}}{Y_{i+1,1}} \right|, \left| \frac{Y_{i+1,2} - Y'_{i+1,2}}{Y_{i+1,2}} \right| \right). \tag{H.11}$$

If d is smaller than the precision $\epsilon = 0.01$ the step size is reduced to $\frac{hs}{d/\epsilon}$ with the safety factor $s = 0.9$ and the step is repeated. If d is larger than or equal to the precision, the step is accepted, $Y_{i+1,1,2}$ is taken as the next value for the abundance. The stepwidth is increased to $\frac{hs}{d/\epsilon}$ in this case. If the stepwidth falls below a given limit like $1/10$ of the initial step width, the recursion is aborted. The same is true if a maximum number of steps is reached.

List of Figures

List of Tables

Bibliography

[1] S. Esch. M. Klasen. and C.E. Yaguna : Detection prospects of singlet fermionic dark matter. *Phys.Rev.* **D88** p.075017 (2013) doi : 1308.0951.

[2] S. Esch. C. Yaguna. M. Klasen : A minimal model for two-component dark matter. `http ://arxiv.org/abs/1406.0617`.

[3] Aitchison, I. ; Hey, A.J. : Gauge Theories in Particle Physics. *Institute of Physics Publishing* (1996)

[4] Bertone, G., editor : Particle Dark Matter - Observations, Models and Searches. *Cambridge University Press* (2010)

[5] Clowe, D. et al: A direct empirical proof of the existence of dark matter. *The Astr.J.* **648** : p.L109–L113 (2006)

[6] Djouadi, A. et al: Implications of lhc searches for higgs-portal dark matter. *Physics Letters* **B 709** p.65–69 (2012)

[7] Fixsen, D.J. : The temperature of the cosmic microwave background. *The Astrophysical Journal* **707** p.916–920 (2009)

[8] Hinshaw, G. et al: Nine-year microwave anisotropy probe (WMAP) observations : Cosmological parameter results. *arxiv* 1212.5226 (2012)

[9] Jungmann, G. et al: Supersymmetric dark matter. *Physics Report* **267** p195–373 (1996)

[10] Lopez-Honorez, L. et al: Higgs portal, fermionic dark matter, and a standard model like higgs at 125 gev. *Physics Letters* **B 716** p.179–185 (2012)

[11] NASA ; Fruchter,A and the ERO team (STScI): *STScI-2000-07* (2000)

[12] NASA. and WMAP Team : Nine year microwave sky (2012)

[13] NASA, U.Arizona, and D.Clowe et al.

[14] D. O'Connell et al: Minimal extension of the standard model scalar sector. *Physical Review* **D75** p.037701 (2007)

[15] V.C. RUBIN AND W.K. FORD JR. : Rotation of the andromeda nebula from a spetcroscopic survey of emission regions. *The Astrophysical Journal* **159** p.379–403 (1970)

[16] T.S. VAN ALBADAet al: Distribution of dark matter in the spiral galaxy ngc3198. *The Astrophysical Journal* **295** p.305–313 (1985)

[17] F. ZWICKY : Die Rotverschiebung von extragalaktischen Nebeln. *Helvetica Physica Acta* **VI** p.110–127 (1933)

[18] Y. GYUN KIMet al: Singlet fermionic dark matter. *JHEP* **0805** p.100 (2008) doi : 0803.2932.

[19] S. BAEKet al: Search for the Higgs portal to a singlet fermionic dark matter at the LHC. *JHEP* **1202** p.047 (2012) doi : 1112.1847.

[20] L. LOPEZ-HONOREZ et al: Higgs portal, fermionic dark matter, and a Standard Model like Higgs at 125 GeV. *Phys.Lett.* **B716** p.179–185 (2012) doi : 1203.2064.

[21] S. BAEK et al: Vacuum structure and stability of a singlet fermion dark matter model with a singlet scalar messenger. *JHEP* **1211** p.116 (2012) doi : 1209.4163.

[22] M. FAIRBAIRN R. HOGAN : Singlet Fermionic Dark Matter and the Electroweak Phase Transition. *arXiv* (2013) doi : 1305.3452.

[23] P.A. ADE et al: Planck 2013 results. XVI. Cosmological parameters. *arXiv* (2013) doi : 1303.5076.

[24] E. APRILE et al: Dark Matter Results from 225 Live Days of XENON100 Data. *Phys.Rev.Lett.* **109** : (2012) doi : 1207.5988.

[25] E. APRILE et al: The XENON1T Dark Matter Search Experiment. *arXiv* (2012) arXiv : 1206.6288.

[26] D.S. AKERIB et al: First results from the LUX dark matter experiment at the Sanford Underground Research Facility. *Phys.Rev.Lett.* **112** : (2014) doi : 1310.8214.

[27] F. HALZEN, D. HOOPER : The Indirect Search for Dark Matter with IceCube. *New J.Phys.* **11** : (2009) doi : 0910.4513.

[28] T. DEYOUNG : Particle Physics in Ice with IceCube DeepCore. *Nucl.Instrum.Meth.* **A692** p.180–183 (2012) doi : 1112.1053.

[29] R. ABBASI et al: The Design and Performance of IceCube DeepCore. *Astropart.Phys.* **35** p.615–624 (2012) doi : 1109.6096.

[30] Planck Scientific Collaboration : NASA Webpage : PLANCK reveals an almost perfect Unvierse. http ://www.nasa.gov/mission_pages/planck/multimedia/index.html#.VBCOKfi2mb4.

[31] R.K. Sachs and A.M. Wolfe : Perturbations of a Cosmological Model and Angular Variations of the Microwave Background. *Astrophys.J.* **147** p.73 (1976) doi : 10.1086/148982.

[32] P.J.E. Peebles and J.T. Yu : Primeval Adiabatic Perturbation in an Expanding Universe. *Astrophys.J.* **162** p.815 (1970) doi : 10.1086/150713.

[33] G. Hinshaw. et al: Seven-Year Wilkinson Microwave Anisotropy Probe (WMAP) Observations : Power Spectra and WMAP-Derived Parameters . *Astrophys.J.Suppl.* **192** p.16 (2011) doi : 10.1088/0067-0049/192/2/16.

[34] J.A. Peacock : A Measurement of the Cosmological Mass Density from Clustering in the 2dF Galaxy Redshift Survey. *Nature* **410** p.169–173 (2001) doi : 10.1038/35065528.

[35] V. Springel. et al: Simulations of the formation, evolution and clustering of galaxies and quasars. *Nature* **435** p.629–636 (2005) doi : 10.1038/nature03597.

[36] G. Lemson, Virgo consortium : Millennium Simulation. http ://www.mpa-garching.mpg.de/millennium/.

[37] S. Dimopoulos. et al: Supersymmetry and the Scale of Unification. *Phys.Rev.* **D24** p.1681–1683 (1981) doi : 10.1103/PhysRevD.24.1681.

[38] F. Boudjema. et al: One-loop corrections to gaugino (co-)annihilation into quarks in the MSSM . *Phys.Rev.* **D89** : (2014) doi : 10.1103/PhysRevD.89.114012.

[39] B. Herrmann. et al: One-loop corrections, uncertainties and approximations in neutralino annihilations : Examples. *Phys.Rev.* **d84** : (2011) doi : 10.1103/PhysRevD.84.116001.

[40] P. Gondolo. G. Gelmini. : Cosmic abundances of stable particles : improved analysis. *Nucl.Phys.* **B360** p.145–179 (1997) doi : 10.1016/0550-3213(91)90438-4.

[41] O. Klein : Quantentheorie und fünfdimensionale Relativitätstheorie. *Zeit.F.Phys.* **A37** p.895–906 (1926) doi : 10.1007/BF01397481.

[42] T. Kaluza : Zum Unitätsproblem in der Physik. https ://archive.org/details/sitzungsberichte1921preussi.

[43] T. Appelquist. et al: Kaluza–Klein Theory in Perspective (Frontiers in Physics). *Addison Wesley* (1987) ISBN :0-201-09829-6.

[44] J. Overduin, P. Wesson : Kaluza–Klein Gravity. *Phys.Rept.* **238** p.303–380 (1997) doi : 10.1016/S0370-1573(96)00046-4.

[45] H. Cheng. et al: Kaluza–Klein Dark Matter. *Phys.Rev.Lett* **89** : (2002) doi : 10.1103/PhysRevLett.89.211301.

[46] M. Cirelli. et al: Minimal Dark Matter. *Nucl.Phys* **B753** p 178–194 (2006) doi : 10.1016/j.nuclphysb.2006.07.012.

[47] K. Enquist. et al: Standard Model with a real singlet scalar and inflation. *JCAP* **2014** p.35 (2014) doi : 10.1088/1475-7516/2014/08/035.

[48] W. Guo. Y. Wu : The real singlet scalar dark matter model. *JHEP* **1010** p.83 (2010) doi : 10.1007/JHEP10(2010)083.

[49] S. Bhattacharya. et al.; Two-Component Dark Matter. *JHEP* **1310** p.158–180 (2013) doi : 10.1007/JHEP10(2013)158.

[50] M. Medvedev : Cosmological Simulations of Multi-Component Cold Dark Matter. *JHEP* **113** : (2014) doi : 10.1103/PhysRevLett.113.071303.

[51] G. Belanger, et al: Impact of semi-annihilations on dark matter phenomenology - an example of Z_N symmetric scalar dark matter. *Phys.Rev.Lett.* **1204** p.010 (2012) doi : 1202.2962.

[52] R. Bernabei. et al: Investigating the DAMA annual modulation data in the framework of inelastic dark matter. *EPJ.* **C23** p.61–64 (2002) doi : 10.1007/s100520100854.

[53] C. Aalseth. et al: CoGeNT : A Search for Low-Mass Dark Matter using p-type Point Contact Germanium Detectors. *Phys.Rev.* **D88** : (2013) doi : 10.1103/PhysRevD.88.012002.

[54] G. Angloher. et al: Results from 730 kg days of the CRESST-II Dark Matter search. *EPJ.* **C72** : (2012) doi : 10.1140/epjc/s10052-012-1971-8.

[55] R. Agnese. et al. CDMSlite : A Search for Low-Mass WIMPs using Voltage-Assisted Calorimetric Ionization Detection in the SuperCDMS Experiment. *Phys.Rev.Lett.* **112** : (2014) doi : 10.1103/PhysRevLett.112.041302.

[56] S. Archambault and the PICASSO Collaboration : Constraints on Low-Mass WIMP Interactions on 19F from PICASSO. *Phys.Lett.* **B711** p.153–161 (2012) doi : 10.1016/j.physletb.2012.03.078.

[57] M. Ackermann et al: Constraints on the Galactic Halo Dark Matter from Fermi-LAT Diffuse Measurements. *Astrophys.J.* **761** p.91 (2012) doi : 1205.6474.

[58] O. Adriani et al: Details for Measurement of the isotopic composition of hydrogen and helium nuclei in cosmic rays with the PAMELA experiment. *Astrophys.J.* **770** : (2013) doi : 10.1088/0004-637X/770/1/2.

[59] G. Aad et al: Search for Dark Matter in Events with a Hadronically Decaying W or Z Boson and Missing Transverse Momentum in pp Collisions at $s\sqrt{}$=8 TeV with the ATLAS Detector. *Phys. Rev. Lett.* **12** : (2014) doi : 10.1103/PhysRevLett.112.041802.

[60] A. Askew et al: Searching for Dark Matter at Hadron Colliders. *IKAZ.* **A29** : (2014) doi : 10.1142/S0217751X14300415.

[61] M. Ackermann et al. Constraining Dark Matter Models from a Combined Analysis of Milky Way Satellites with the Fermi Large Area Telescope. *Phys.Rev.Lett.* **107** : (2011) doi : 1108.3546.

[62] P. Salati, et al: Indirect Dark Matter Detection with Cosmic Antimatter. *arXiv* (2010) doi : 1003.4124.

[63] F. Halzen and D. Hooper : The Indirect Search for Dark Matter with IceCube. *New J.Phys.* **11** : (2009) doi : 0910.4513.

[64] M. Danninger : Thesis : A search for dark matter annihilations in the Sun with IceCube and related studies. `http ://icecube.wisc.edu/ mda65/talks/thesis.pdf`.

[65] M.G. Aartsen et al: Search for dark matter annihilations in the Sun with the 79-string IceCube detector. *Phys.Rev.Lett.* **110** p.131302 (2013) doi : 1212.4097.

[66] J. McDonald : Gauge singlet scalars as cold dark matter. *Phys.Rev.* **D50** p.3637–3649 (1994) doi : hep-ph/0702143.

[67] C.P. Burgess, et al: The Minimal model of nonbaryonic dark matter : A Singlet scalar. *Nucl.Phys.* **B619** p.709–728 (2001) doi : hep-ph/0011335.

[68] C.E. Yaguna : Gamma rays from the annihilation of singlet scalar dark matter. *JCAP* **0903** p.003 (2009) doi : 0810.4267.

[69] A. Goudelis. Y. Mambrini. and C.E. Yaguna : Antimatter signals of singlet scalar dark matter. *JCAP* **0912** p.008 (2009) doi : 0909.2799.

[70] Y. Mambrini : Higgs searches and singlet scalar dark matter : Combined constraints from XENON 100 and the LHC. *Phys.Rev.* **D84** p.115017 (2011) doi : 1108.0671.

[71] A. Semenov : LanHEP - a package for automatic generation of Feynman rules from the Lagrangian. Updated version 3.1. *arXiv* (2010) arXiv : 1005.1909.

[72] G. Belanger, et al: micrOMEGAs 3 : A program for calculating dark matter observables. *Comput.Phys.Commun.* **185** p.960–985 (2014) doi : 1305.0237.

[73] P. Gondolo, J. Edsjo, P. Ullio, L. Bergstrom, Mia Schelke, et al: DarkSUSY : Computing supersymmetric dark matter properties numerically. *JCAP* **0407** p.008 (2004) doi : astro-ph/0406204.

[74] P. Gondolo : 1 DarkSUSY darksusy-5.1 (rev 806) Manual and long description of routines. `http ://www.fysik.su.se/ edsjo/darksusy/docs/Manual.pdf`.

[75] G. Duda, et al: Detection of a subdominant density component of cold dark matter. *Phys.Lett.B* **529** p.187–192 (2002) doi : hep-ph/0102200.

[76] J. Silk : Cosmic Black-Body Radiation and Galaxy Formation. *Astrophys.J.* **151** p.459 (1968) doi : 10.1086/149449.

[77] CMS Collaboration : Search for Supersymmetry in pp Collisions at 7 TeV in Events with Jets and Missing Transverse Energy. *Phys.Lett.B* **698** p.196–218 (2011) doi : 0.1016/j.physletb.2011.03.021.

[78] ATLAS Collaboration : Search for supersymmetry using final states with one lepton, jets, and missing transverse momentum with the ATLAS detector in $\sqrt{s} =$ 7 TeV pp. *Phys.Rev.Lett.* **106** : (2011) doi : 10.1103/PhysRevLett.106.131802.

[79] H.P. Nilles : Dynamically broken supergravity and the hierarchy problem. *Phys.Lett.* **B115** p.198 (1982) doi : 10.1016/0370-1573(84)90008-5.

[80] P. Higgs : Broken symmetries and the masses of gauge bosons. *Phys.Rev.Lett.* **13** p.508 (1964) doi : 10.1103/PhysRevLett.13.508.

[81] Max-Planck-Institut für Kernphysik : Webpage : Dark Matter. `http ://www.mpi-hd.mpg.de/lin/research_DM.en.html`.

[82] T. Saab : An Introduction to Dark Matter Direct Detection Searches & Techniques. *arXiv* (2012) arXiv :1203.2566.

[83] V. Barger et al: LHC Phenomenology of an Extended Standard Model with a Real Scalar Singlet. *Phys.Rev.* **D77** : (2008) doi : 0706.4311.

[84] G. Aad et al: Observation of a new particle in the search for the Standard Model Higgs boson with the ATLAS detector at the LHC. *Phys.Lett.* **B716** p.1–29 (2012) doi : 1207.7214.

[85] S. Chatrchyan et al: Observation of a new boson at a mass of 125 GeV with the CMS experiment at the LHC. *Phys.Lett.* **B716** p.30–61 (2012) doi : 1207.7235.

[86] J.R. Espinosa, et al: Fingerprinting Higgs Suspects at the LHC. *JHEP* **1205** p.097 (2012) doi : 1202.3697.

[87] CMS Collaboration : Combination of standard model Higgs boson searches and measurements of the properties of the new boson with a mass near 125 GeV. (2013) CMS-PAS-HIG-13-005.

[88] ATLAS Collaboration : Combined coupling measurements of the Higgs-like boson with the ATLAS detector using up to 25 fb^{-1} of proton-proton collision data. (2013) ATLAS-CONF-2013-034 ATLAS-COM-CONF-2013-035.

[89] J. Ellis and T. You : Updated Global Analysis of Higgs Couplings. *JHEP* **1306** p.103 (2013) doi : 1303.3879.

[90] C. Cheung. et al: Prospects and Blind Spots for Neutralino Dark Matter. *JHEP* **1305** : (2013) doi : 10.1007/JHEP05(2013)100.

[91] D.C. Mallings. et al: After LUX : The LZ Program. *arXiv* : (2011) arXiv :1110.0103 .

[92] M. Aguilar. et al: First Result from the Alpha Magnetic Spectrometer (AMS) Experiment. *Phys.Rev.Lett.* **110** : (2013) doi : 10.1103/PhysRevLett.110.141102.

[93] E. Corbelli. S. Selucci : The extended rotation curve and the dark matter halo of M33. *Mon.Not.Roy.Ast.Soc.* **311** p.441–447 (2000) doi : 10.1046/j.1365-8711.2000.03075.x.

[94] K. Begeman. et al: Extended rotation curves of spiral galaxies : dark haloes and modified dynamics. *Mon.Not.Roy.Ast.Soc.* **249** p.523 (1991) ISSN 0035-8711.

Declaration of originality

I hereby declare that this thesis, *Fermionic singlet and two-component dark matter*, represents my original work and that I have used no other sources except as noted by citations and listed in the references. All data, tables, figures and text citations which have been reproduced from any other source have been explicitly acknowledged a such[1].

Münster, 30.10. 2014
Place, date

Sonja Esch

[1] This declaration of originality follows nearly the exact wording of the University of Bern declaration of originality, found at http://www.gcb.unibe.ch/unibe/graduateschools/gcb/content/e3529/e3695/e3652/Declaration_of_Originality_e